Enhanced Thermal Transport in Soft Composites

Through Magnetic Alignment and Contact Engineering

by

Matthew Ralphs

A Dissertation Presented in Partial Fulfillment
of the Requirements for the Degree
Doctor of Philosophy

Approved February 2019 by the
Graduate Supervisory Committee:

Konrad Rykaczewski, Co-Chair
Robert Wang, Co-Chair
Patrick Phelan
Liping Wang
Shankar Devasenathipathy

ARIZONA STATE UNIVERSITY
May 2019

ABSTRACT

Soft polymer composites with improved thermal conductivity are needed for the thermal management of electronics. Interfacial thermal boundary resistance, however, prevents the efficient use of many high thermal conductivity fill materials. Magnetic alignment of ferrous fill material enforces percolation of the high thermal conductivity fill, thereby shifting the governing boundary resistance to the particle-particle interfaces and increasing the directional thermal conductivity of the polymer composite. Magnetic alignment maximizes the thermal conductivity while minimizing composite stiffening at a fill fraction of half the maximum packing factor. The directional thermal conductivity of the composite is improved by more than 2-fold. Particle-particle contact engineering is then introduced to decrease the particle-particle boundary resistance and further improve the thermal conductivity of the composite.

The interface between rigid fill particles is a point contact with very little interfacial area connecting them. Silver and gallium-based liquid metal (LM) coatings provide soft interfaces that, under pressure, increase the interfacial area between particles and decrease the particle-particle boundary resistance. These engineered contacts are investigated both in and out of the polymer matrix and with and without magnetic alignment of the fill. Magnetically aligned in the polymer matrix, 350nm-thick silver coatings on nickel particles produce a 1.8-fold increase in composite thermal conductivity over the aligned bare-nickel composites. The LM coatings provide similar enhancements, but require higher volumes of LM to do so. This is due to the rapid formation of gallium oxide, which introduces additional thermal boundaries and decreases the benefit of the LM coatings.

The oxide shell of LM droplets (LMDs) can be ruptured using pressure. The pressure needed to rupture LMDs matches closely to thin-walled pressure vessel

theory. Furthermore, the addition of tungsten particles stabilizes the mixture for use at higher pressures. Finally, thiols and hydrochloric acid weaken the oxide shell and boost the thermal performance of the beds of LMDs by 50% at pressures much lower than 1 megapascal (MPa) to make them more suitable for use in TIMs.

DEDICATION

This dissertation is dedicated to my wonderful wife, Amanda, who has supported me whole heartedly in this endeavor since day one.

ACKNOWLEDGMENTS

A big thanks to my faculty advisers, Dr. Konrad Rykaczewski and Dr. Robert Wang, for shepherding me through my PhD and lining me up for future success.

TABLE OF CONTENTS

Page

LIST OF TABLES viii

LIST OF FIGURES ix

NOMENCLATURE x

CHAPTER

1 INTRODUCTION 1

Introduction 1

Thermal Interface Materials Overview 1

Interfacial Thermal Boundary Resistance 8

Hypothesis 10

Summary and Outline 10

2 BACKGROUND, THEORY, AND MEASUREMENT 12

Introduction 12

Contact Resistance and Effective Thermal Conductivity 12

TIM Thickness to Match Component Roughness 14

Liquid Metal in a Polymer Matrix 16

Polydimethylsiloxane as a Matrix 17

Theoretical Models for Composite Thermal Conductivtiy 18

Liquid Metal Oxide Manipulation 21

Stepped Bar Appartus and ASTM D5470 Standard Basics 22

3 MAGNETIC ALIGNMENT IN PARTICLE-LADEN POLYMER COMPOSITES 26

Introduction 26

Magnetic Alignment to Enforce Percolation 26

Previous Work 27

Methods 28

CHAPTER Page

Results and Discussion 28

Conclusions 29

4 PARTICLE-PARTICLE CONTACT ENGINEERING 31

Introduction 31

Low Metal-Metal Thermal Boundary Resistance 31

Silver-Silver Interfaces 33

Liquid Metals in TIMs 34

Methods 35

Results and Discussion 35

Conclusions 36

5 THERMAL RAMIFICATIONS OF LM OXIDE RUPTURE 38

Introduction 38

Popping LMDs 38

Methods 41

Results and Discussion 47

Conclusions 51

6 CONCLUSIONS AND FUTURE WORK 53

REFERENCES 56

APPENDIX

A HEAT SINK SURFACE PROFILES 67

B APPROVALS TO USE PREVIOUSLY PUBLISHED WORKS 72

C BUCKLING OF MAGNETICALLY-FORMED FILLER FIBER COLUMNS UNDER COMPRESSION INCREASES THERMAL RESISTANCE OF SOFT POLYMER COMPOSITES 74

APPENDIX Page

D IN SITU ALLOYING OF THERMALLY CONDUCTIVE POLYMER COMPOSITES BY COMBINING LIQUID AND SOLID METAL MICRO-ADDITIVES 82

E THERMAL CONDUCTIVITY ENHANCEMENTS OF SOFT POLYMER COMPOSITES THROUGH MAGNETICALLY-INDUCED PERCOLATION AND PARTICLE-PARTICLE CONTACT ENGINEERING 94

BIOGRAPHICAL SKETCH 102

LIST OF TABLES

Table Page

2.1 Heat Sink Details and Roughness Values 15

2.2 Table of Most Applicable Models for Particle Laden Composites 20

LIST OF FIGURES

Figure Page

1.1 Illustration Demonstrating the Concept of Contact Resistance and TIMs ... 3

1.2 LM Thermal Grease Pump-out ... 5

1.3 Thermal Resistance Measurements for Commercial TIMs ... 6

1.4 Total Package Resistance as a Function of k_{TIM} ... 7

1.5 Illustration of R_c and R_b ... 8

1.6 Theoretical Effect of Boundary Resistance on Particle-Laden Composites ... 9

2.1 Illustration and Theoretical Effect of Contact Resistance ... 13

2.2 Thermal Resistance Mearurements Demonstrating Benefits of Soft TIMs ... 14

2.3 ASTM D5470 and SBA Measurement Principles ... 25

4.1 Schematic of Large, Poly-dispersed LM-Cu Filler Increases k ... 32

4.2 k vs Size of Poly-dispersed LM-Cu Filler ... 33

5.1 Pressure vs LMD Diameter for Various Oxide Tensile Strengths ... 39

5.2 Illustration Detailing Sedimentation Process for LMD Size Distributions ... 42

5.3 Some Typical LMD Size Distributions After the Sedimentation Process ... 42

5.4 Illustration and Details of the Dropcast Process for Measuring LMDs ... 43

5.5 Typical Thermal Data From LMD Compression Measurements ... 44

5.6 Compressed and Uncompressed Beds of LMDs ... 45

5.7 Illustration Detailing Process for Thiol and HCl Treated LMDs ... 47

5.8 Thermal Results for Five LMD Size Distributions With Pressure Data ... 48

5.9 Thermal Resistance vs Normalized Thickness of LMDs ... 49

5.10 Thermal Results for LMDs With Addition of Tungsten Particles ... 50

5.11 Thermal Conductivity vs Pressure Measurements for Thiolated LMDs ... 51

NOMENCLATURE

Symbol	Definition
TIM	Thermal interface material
R_c	Thermal contact resistance
R_b	Interfacial thermal boundary resistance
R_{th}	Measured thermal resistance, includes R_c
k	Thermal conductivity
k_c	Composite thermal conductivity
k_{eff}	Effective thermal conductivity, includes R_c
k_{TIM}	Thermal conductivity of a TIM
ϕ	Filler volume fraction
ϕ_{max}	Maximum packing factor or filler volume fraction
LM	Liquid Metal (gallium-based, unless stated otherwise)
LMD	Liquid Metal Droplet
P	Pressure
t	sample thickness
t_0	initial or uncompressed sample thickness
t_c	compressed sample thickness

CHAPTER 1

INTRODUCTION

1.1 Introduction

This chapter will, first, present a short overview of the two main concepts that are critical in understanding the scope of this work, namely, the application and the underlying physics. The main target application for this work is thermal interface materials and the thermal management of electronics. The underlying physics on which this work is predicated is that of the existence of an interfacial thermal boundary resistance at all microscopic interfaces in a composite material. The second half of this chapter will introduce the main hypothesis of this work and a summary of the organization for the rest of the document.

1.2 Thermal Interface Materials Overview

Thermal management of electronics is essential as the semiconductor industry tries to advance as fast as Moore's Law predicts, doubling transistor density every two years.[1] The increase in packing density of transistors on a single microelectronic chip was facilitated by ever decreasing the size of metal-oxide-semiconductor field-effect transistors (MOSFET).[2] Decreases in transistor size and increases in speed, or frequency, have been at the forefront of semiconductor technology research. However, transistor speed has stalled over the last few years due to the physical limitations on heat dissipation.[3] "[…] It has become practically impossible to keep on conjunctly increasing both [transistor count and frequency] due to physical limitations on power dissipation; one of the two features (i.e. either number of transistors or frequency) had to level off in order to make the ICs

[integrated circuits] capable to operate under practical thermal conditions. Frequency was selected as the sacrificial victim and it has stalled in the few GHz since the middle of the previous decade."[3] Integrated circuits (ICs) now have features down to 14 nanometers,[2–4] paving the way for extremely high packing densities and leaving very little surface area available to dissipate accumulated heat. Thus, it is critical to efficiently remove heat from the IC through the use of thermal interface materials.

Thermal interface materials (TIMs) help dissipate heat away from ICs by minimizing the thermal contact resistance between electronic packaging components. Thermal contact resistances are caused by air gaps between the two geometrically imperfect surfaces, as illustrated by Figure 1.1a. A TIM eliminates air gaps between components by replacing those gaps with a higher thermal conductivity material. In traditional electronics packaging, TIMs are used on either side of an integrated heat spreader (IHS), as shown in Figure 1.1b. The main job of the IHS is to spread out the heat generated by the CPU so it doesn't create hot spots.[5] Reducing the thermal resistance between components enables more heat to be removed from the CPU.

TIMs are typically greases or gels that can conform and fill the imperfections on the interfacing surfaces. Polymer composite TIMs have been at the forefront of advanced TIM research over the past decade,[6–8] ever since the 2005 ITRS highlighted the need for TIMs with improved adhesion, higher elastic modulus, and increased thermal conductivity.[9] High k fill particles are added to the polymer matrix to boost its thermal conductivitiy. The thermal conductivity of most polymers is low (0.1-0.6 $Wm^{-1}K^{-1}$).[10] Silicon based soft polymers have a thermal conductivity of about 0.2-0.3 $Wm^{-1}K^{-1}$,[11] which is 10 times higher than air, but 50 times lower than stainless steel, 1000 times lower than copper and aluminum, and 10,000 times lower

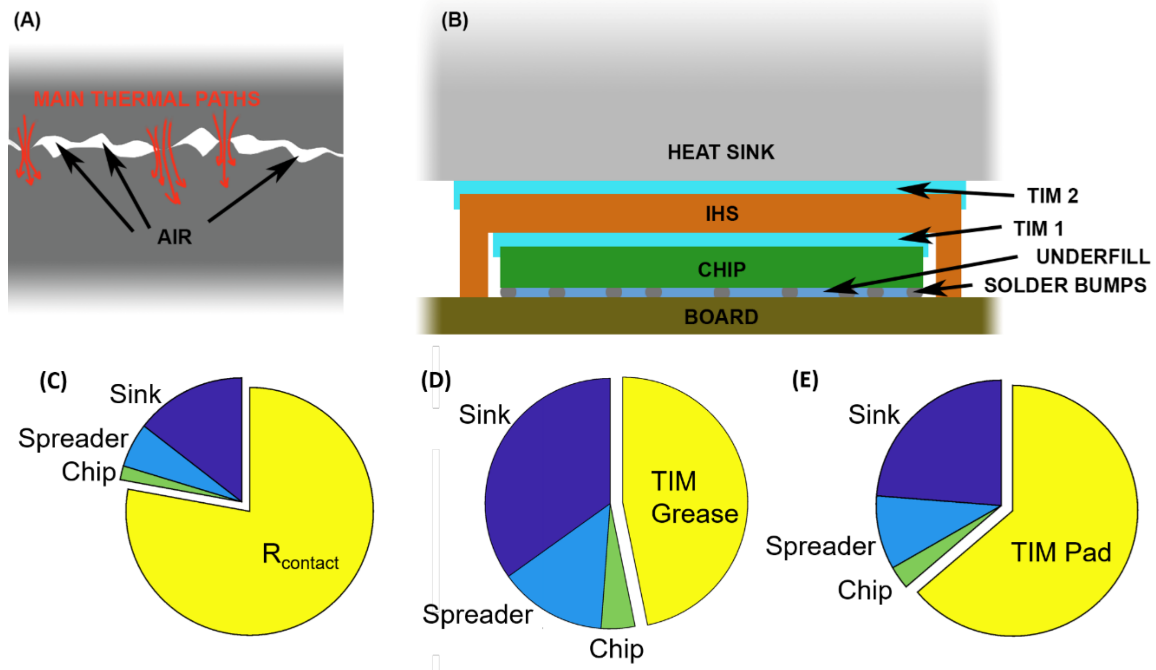

Figure 1.1: (A) illustration demonstrating how air gaps prevent good thermal conduction across mechanical interfaces; (B) a diagram illustrating where thermal interface materials might be used in integrated circuits (IHS = integrated heat spreader); and diagrams detailing the amount of thermal resistance contributed by individual components using values suggested by Bogatin[12] when no TIMs are used (C), a standard commercial TIM grease is used (D), and when a standard commercial TIM pad is used (E).

than diamond. However, the low elastic modulus of polymers make them ideal for use as TIMs because they can easily conform to the micro-roughness of the mating interfaces to eliminate air pockets but will not be squished out under thermal cycling.

Figure 1.1c – 1.1e provide diagrams detailing thermal resistances of individual components as compared to $R_{contact}$ (no TIMs), a generic commercial TIM grease with k = 2 $Wm^{-1}K^{-1}$ and BLT = 50µm, and a generic commercial TIM pad with k = 10 $Wm^{-1}K^{-1}$ and BLT = 500µm, respectively. These diagrams assume component thermal resistances of: heat sink = 0.4 K/W, chip = 0.05 K/W, and integrated heat spreader = 0.16 K/W.[12]

In 2003, Gwinn and Webb listed the characteristics of an ideal TIM and stated that the "ideal TIM has not yet been discovered."[13] The characteristics they listed are:

1. High thermal conductivity, *k*
2. Easily deformed by small contact pressure to contact all uneven areas of both mating surfaces, including surface pores, eliminating the thermal contact resistance
3. Will not leak out of the interface
4. Non-toxic
5. Minimal thickness
6. Will maintain performance indefinitely
7. Manufacturing friendly (easy to apply and remove)

Most of the leading commercial TIMs can be categorized as either a thermal grease or a thermal pad. Both are packed with high *k* fill material to boost the overall *k* of the composite. Thermal greases generally have very little matrix material around the high *k* fill. Greases also typically use non-crosslinked polymers or gels as the matrix, providing good mechanical compliance and a flexible application thickness, but making them susceptible to leakage (often referred to as "pump-out"). Furthermore, while some commercial thermal greases profess to have a high intrinsic thermal conductivity, their effective thermal conductivity (see Section 2.2 for more details) in application is generally much lower.[14,15]

Pump-out is caused by thermally induced cycling stresses at IC component interfaces that press the thermal grease out of the interface when the IC gets hot from normal operation. When the IC cools down, the grease does not return to its original position. Instead, it keeps moving further out of its intended interface until it has been completely pumped-out of the interface. This is one cause for the short

life of modern electronics. Degraded TIM performance leads to degraded IC performance and shortened life.

The main thermal stresses that cause pump-out stem from a mismatch in coefficients of thermal expansion between IC components (i.e. the silicon chip and a copper or aluminum heat spreader). This mismatch causes disproportional distortions at the interface, which compress and pump the thermal grease out from between the components. Figure 1.2 shows that, with very little pressure, a commercial liquid metal thermal grease is easily dislogded from its intended interface.

Thermal pads, in general, have an interconnected and cross-linked matrix thus there is no pump-out. But to have an interconnected matrix means a limit to how much filler can be added as well as to how thin the TIM can be – both of which increase the minimum thermal resistance of the TIM. Figure 1.3 shows the thermal performance of several leading commercial TIMs, both greases and pads, along with a polished Cu-Cu interface for reference. The figure presents the thermal resistance (R_{th}) of the TIMs between two polished copper bars, indicative of normal TIM performance in a standard application. Figure 1.3b presents R_{th} against the bond line thickness (BLT), which is the thickness of the TIM in the interface under normal operating conditions.[16] All the TIMs presented in this figure proved effective at

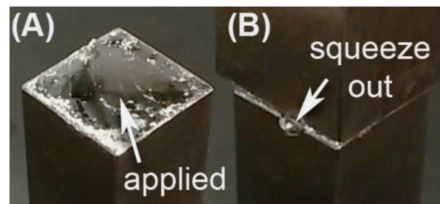

Figure 1.2: LM thermal grease (Thermal Grizzly Conductonaut) (A) as applied and (B) with a 50g component (5.4 kPa) placed on top of the interface and the subsequent loss of the thermal grease in the interface.

decreasing the thermal resistance at the Cu-Cu interface, but it is obvious that greases generally have superior initial thermal performance over pads, mainly because they can be applied in very thin layers and have excellent mechanical compliance. However, because of the issues with greases explained earlier, a pad has the potential to fulfill the majority of the desired characteristics in an ideal TIM and perform better in the long run, if only the effective thermal conductivity can be increased.

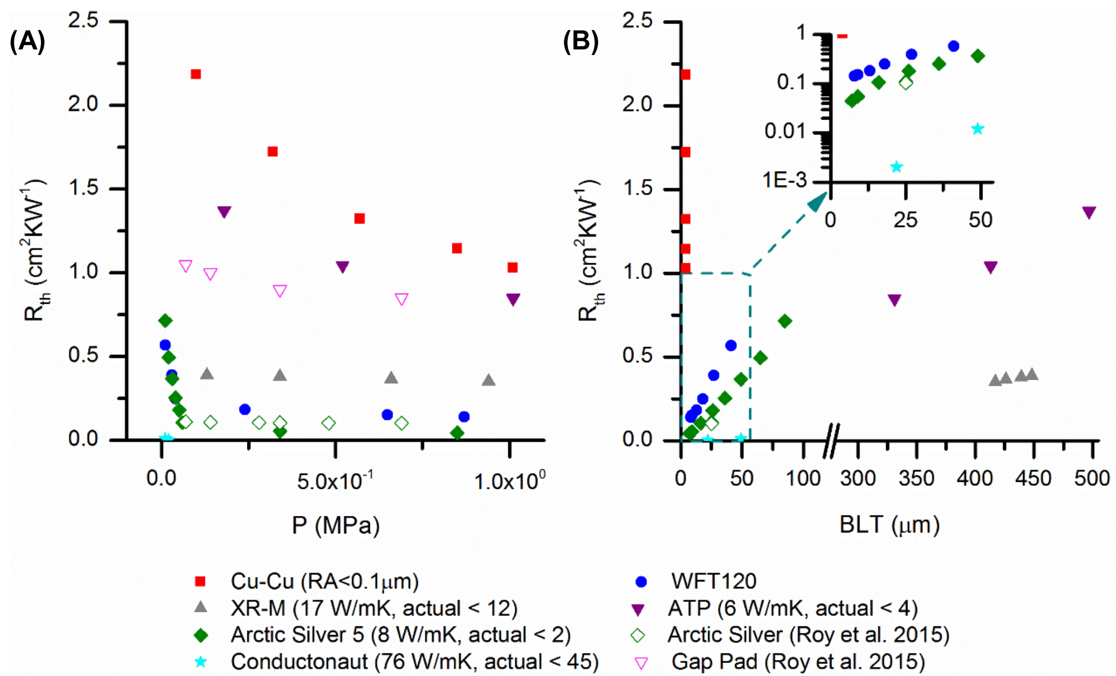

Figure 1.3: (A) Plot of thermal resistance, R_{th}, vs pressure, P, and (B) R_{th} vs bond line thickness (BLT) for commercial TIMs, both measured and literature values. The Cu-Cu interface is included for reference and is a mirror finish with BLT 3-4 μm. Literature values are from Roy et al. 2015.[15] Inset in (B) is showing log scale on the y axis and is a magnification from the lower left corner of (B), same units. WFT120 is WakeField Type 120 thermal compound, XR-M is Fujipoly Ultra Extreme XR-m thermal pad, ATP is Arctic Thermal Pad, and Conductonaut is Thermal Grizzly Conductonaut Thermal Grease Paste. Estimated 68% uncertainty for BLT is 10μm, for pressure is 0.05 MPa, and for R_{th} is 4%.

There are, however, diminishing returns on the total package resistance from increasing the effective thermal conductivity of the TIM, $k_{TIM,eff}$. Figure 1.4 details the effect on total package thermal resistance from increasing the effective thermal conductivity of the TIMs, using the following values for component resistances: heat sink = 0.4 K/W, chip = 0.05 K/W, integrated heat spreader = 0.16 K/W, and various resistances for different TIM BLTs.[12] This assumes the schematic shown in Figure 1.1b and uses a basic thermal resistance network to estimate total package resistance. It assumes that the heat goes from chip to ambient through the heat sink. As shown in the figure, increasing $k_{TIM,eff}$ is important with thicker BLTs, but for thinner BLTs the total package resistance is less dependent on $k_{TIM,eff}$, especially when $k_{TIM,eff}$ is above 5 or 10 W/mK. Thus, increasing $k_{TIM,eff}$ for pads from 10 W/mK to 20 W/mK can still provide thermal benefits on the order of a 30-40% decrease in package resistance.

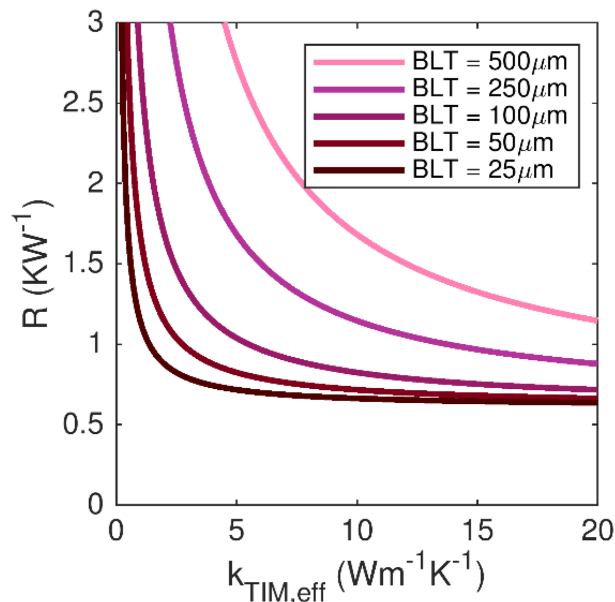

Figure 1.4. Plot of total package resistance (from chip to ambient through the heat sink) with various BLT over a range of effective TIM thermal conductivities.

1.3 Interfacial Thermal Boundary Resistance

Many filler materials have been investigated as additives for polymer composite TIMs, but the cheapest and easiest solution to enhance the thermal conductivity has been to simply add high thermal conductivity metal or ceramic particles into the polymer matrix. Basic effective medium theory predicts that the larger the thermal conductivity of the metal filler, the greater the increase in the thermal conductivity of the composite. Interfacial thermal boundary resistance, R_b, however, between the particles themselves and between the particles and surrounding polymer matrix, plays a critical role in limiting thermal performance in the composite.[17]

Where contact resistance, R_c, is the thermal resistance at macroscopic interfaces between components (i.e. between the TIM and IHS or heat sink), boundary resistance, R_b, is the thermal resistance at microscopic interfaces within the composite, as illustrated in Figure 1.5. Boundary resistances are present at all interfaces where material properties change within the composite. The change in properties at these interfaces produce phonon scattering events leading to thermal resistance. Boundary resistances are present between particles and the matrix, between particles themselves, and even between particles and any particle coatings.

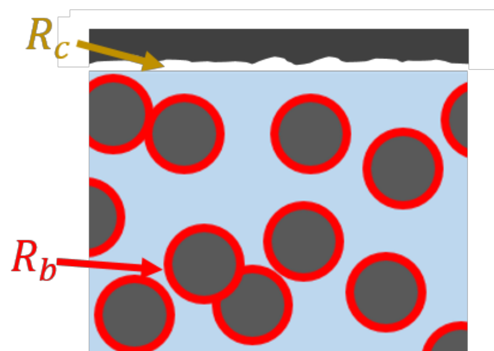

Figure 1.5: Illustration showing the difference between contact resistance (R_c) and interfacial thermal boundary resistance (R_b).

Figure 1.6 presents data on the thermal conductivity of a composite, k_c, using the Tavangar model[18] (see Section 2.6 for details) for various ratios of particle thermal conductivity, k_p, to matrix thermal conductivity, k_m, with various values for R_b. The figure shows that using particles with a thermal conductivity more than 100x that of the matrix produces diminishing returns. In particular, assuming a boundary resistance (R_b) on the order of 10^{-6} m^2KW^{-1} and 10μm diameter particles, 95% of the maximum k_c is reached with k_p/k_m of 100. So with a polymer matrix with k_m = 0.25 $Wm^{-1}K^{-1}$, a particle fill material with k_p = 25 $Wm^{-1}K^{-1}$ is enough to reach 95% of the maximum k_c. Particles with higher k produce diminishing returns. Thus, it is only worthwhile to use k_p/k_m of more than 100x if R_b can be reduced enough to take advantage of the high k_p. Specifically, using k_p = 400 $Wm^{-1}K^{-1}$ for copper, if R_b is decreased from 2×10^{-6} m^2KW^{-1} to 1×10^{-7} m^2KW^{-1} then k_c can be increased by more than 100%.

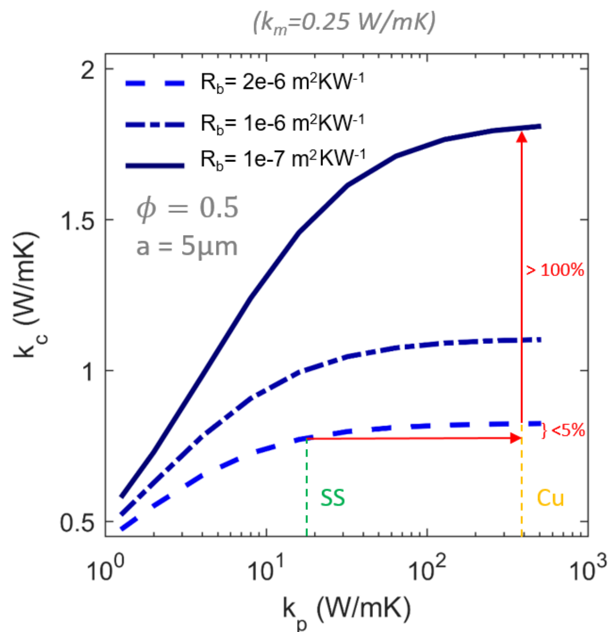

Figure 1.6: Results using the Tavangar model (details of the model can be found in section 2.6) showing the relation between the k_p, k_c, and R_b when k_m = 0.25 Wm-1K-1, φ = 0.5, and the radius of the particle fill, *a*, is 5μm.

1.4 Hypothesis

The interfacial boundary resistance in a particle-laden soft polymer composite can be reduced by increasing the interfacial area between particles and by enforcing particle percolation through the composite. This work will target both of these approaches in the synergistic use of magnetic alignment of fill particles and particle-particle contact engineering. Magnetic alignment of the fill particles enforces percolation across the composite and ensuring good particle-particle contact. The dissipating heat, essentially, thermally short circuits through the connected high k particle network and bypasses the lower k polymer matrix. The resistance at the particle-particle interfaces are then decreased through particle-particle contact engineering using liquid metal- and silver-coated fill particles. These coatings decrease the resistance at the particle-particle interfaces by deforming under minimal pressure and increasing the interfacial area between particles. The combination of these two approaches may enhance the thermal conductivity of the composite.

1.5 Summary and Outline

Chapter 1 demonstrated the need for high k polymer composites in the thermal management of ICs. Boundary resistance, however, prevents the effective use of high k particle fill. This work will target and decrease boundary resistance through a synergistic coupling of magnetic alignment and particle-particle contact engineering.

Chapter 2 presents supplemental background information related to TIMs and introduces several theoretical approaches for modeling the thermal conductivity of particle-laden polymer composites. This chapter also provides details for the thermal

measurement techniques that are common throughout this work and the ASTM standard on which the technique is based. The sections in this chapter are meant as supplemental information for the subsequent chapters.

Chapter 3 will demonstrate the merits of magnetic alignment in enhancing the directional thermal conductivity of polymer composites. Specifically, the theory, fabrication, and performance of magnetically aligned nickel fibers in a silicone-based polymer will be discussed in-depth. Furthermore, we will investigate the performance of such aligned fiber composites under various amounts of compressive strain, highlighting some of the pitfalls in using these aligned composites in applications where they operate under severe strain.

Chapter 4 presents two methods of particle-particle contact engineering that lower the resistance between particles: soft silver coatings and liquid metal (gallium) coatings. These coatings are evaluated on nickel particles with and without magnetic alignment to highlight the drastic enhancement these coatings can make when particle-particle contact is increased through magnetic alignment. Both coatings provide enhanced thermal performance, but the oxide skin on the liquid metal coatings is highlighted as an area for improvement.

Chapter 5 evaluates further the thermal impact of the gallium oxide skin. Gallium droplets are fabricated into liquid metal droplet beds and compressed while measuring the thermal and electrical resistance. Various sizes of droplets are investigated to determine what is required to rupture the oxide and the thermal ramifications of doing so. Solid metal particles are added to the liquid metal droplets as well as some exploratory chemical modifications to further affect the oxide rupture and thermal properties of the beds.

Chapter 6 provides overall conclusions and the direction of future work.

CHAPTER 2

BACKGROUND, THEORY, AND MEASUREMENT

2.1 Introduction

This chapter presents topics that may be useful to better understand the subsequent chapters, including: background topics related to TIMs, theoretical models that can and are used to support the conclusions derived from experiments, and details on the methods of measurement used in this work. The sections in this chapter are not meant to be a cohesive work, but instead should be used as a supplement and reference, as needed.

2.2 Contact Resistance and Effective Thermal Conductivity

It's not enough for a TIM to have a high intrinsic thermal conductivity, it must also have a high effective thermal conductivity – which accounts for contact resistance, R_c. The intrinsic thermal conductivity of the TIM (k or k_{TIM}) relates to the thermal conductivity of the bulk TIM material. The effective thermal conductivity (k_{eff}) relates to the measured thermal conductivity when used between two mating surfaces – indicative of TIM applications. The k_{TIM} only relies on the resistance of the TIM material (R_{TIM}) and the thickness of the pad (t). The k_{eff}, on the other hand, includes R_{TIM} and the contact resistance between the pad and mating surfaces (R_c). The difference between k and k_{eff} is illustrated in Figure 2.1. If R_c stays constant as R_{TIM} is reduced, then R_c plays a larger role in the value of k_{eff}. Figure 2.1a shows R_{TIM} reducing due to the thickness decreasing, but this effect could also come from an increase in k_{TIM}, as shown in Figure 2.1b. At a thickness typical in common thermal

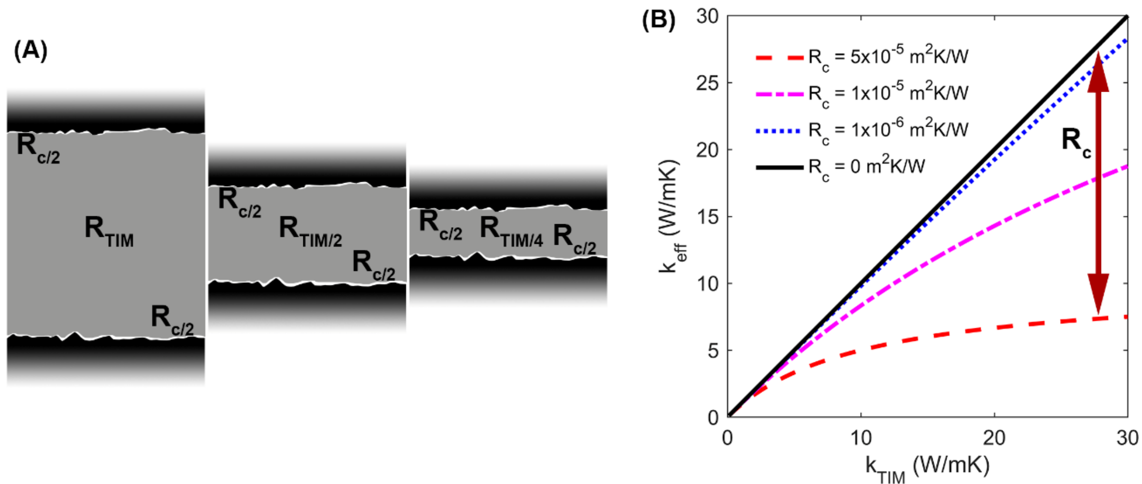

Figure 2.1: (A) An illustration showing how Rc stays the same as RTIM decreases, effecting keff more as RTIM gets smaller and (B) a plot showing the effect Rc has on keff as ktim and Rc increase (kmatrix is 0.25 Wm-1K-1).

grease applications, R_c can account for more than 80% of R_{th}, lowering k_{eff} to less than 15% of the manufacturers stated k_{TIM}.[14]

The elastic modulus (E) of the TIM affects the magnitude of R_c. Two Kapton films, with k_{TIM} = 0.12[19] and 0.37[20] $Wm^{-1}K^{-1}$ and thickness, t = 25 and 50μm, measure a k_{eff} = 0.7 and 0.17 $Wm^{-1}K^{-1}$, respectively. The difference between k_{eff} and k_{TIM} is more than 200%, indicating that R_c makes up half of R_{th} when E is large and t is small. The modulus must be low enough to allow for the material to press into and fill the grooves and irregularities on the mating surfaces and displace the air. Figure 2.2 shows the thermal resistance R_{th} of the two previously mentioned Kapton films along with the polished Cu-Cu interface and EcoFlex 00-20. EcoFlex is a soft, silicone polymer with k_{TIM} around 0.25 $Wm^{-1}K^{-1}$, 100x the thermal conductivity of air, but much lower than most commercial TIMs. Yet, at low pressures and 5x the BLT of the Cu-Cu interface, the Ecoflex provides a 2x decrease in thermal resistance over the

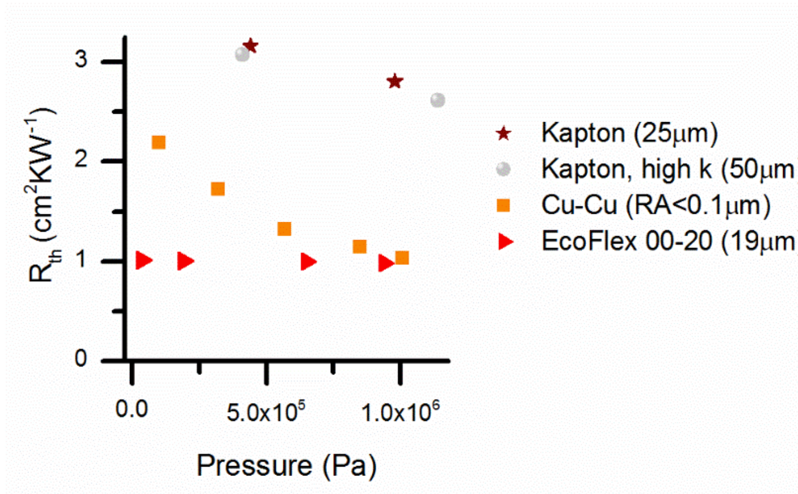

Figure 2.2: A plot of R_{th} vs P for a few common materials, showing that soft materials can lower R_c significantly, thus lowering R_{th}. (RA stands for roughness average)

empty interface. This demonstrates the importance of using a material that is soft enough to fill the air gaps in the interface, which drastically reduces R_c.

2.3 TIM Thickness to Match Component Roughness

There are two things to consider when determining the thickness of a TIM: (1) surface roughness of the mating surfaces and (2) the coefficient of thermal expansion mismatch between IC components. To provide pertinent real data, the roughness of three commercial heat sinks was measured using optical profilometry in order to determine the size of the air gaps a TIM needs to fill. One heat sink was forged copper with a mirror finish, one was aluminum with a machined finish, and one was aluminum with a machined finish with copper heat pipes imbedded on the surface. The details on the heat sinks and the roughness of each is presented in Table 2.1. Further details on the heat sinks and their surface roughness profiles can be found in Appendix A.

Table 2.1: Heat sink details and roughness values from optical profilometry.

Make/Model	Max Peak Height (μm)	Average Surface Roughness (μm)
Cooler Master Hyper 212 EVO	36	3.2
Cryorig H7	12	2.5
Enzotech CNB-SI Forged copper 1100	0.5	0.06

Based on the measured heat sink roughness values, the maximum gap that a TIM would need to fill is somewhere around 60μm. This assumes that the tallest peak aligns perfectly with a similarly tall peak on the mating surface. While it is rare that the two mating components would both have such rough mating surfaces and that the tallest peaks would be aligned, this gives an absolute maximum value for the gap between components based on surface roughness. This maximum thickness is also large enough to account for warpage of planar surfaces.

Between polished surfaces, thermal grease will have a BLT of 15-50μm, but the lower value is impractical for a thermal pad unless it is cast in place. More realistic targets for a pad that provides good support for thermal stresses is 50-100μm, which is thick enough to be handled during application, and is still thin enough to minimize thermal resistance. That being said, the thicknesses of the materials measured in this work are generally between 1 and 1.5 mm in order to help minimize the effects of contact resistance on the measured thermal conductivities.

2.4 Liquid Metal in a Polymer Matrix

Some of the best performing commercial TIMs consist of thin metal foils with moderately low melting temperatures (T_{melt}) such as indium (T_{melt}=157°C, k≈80 Wm^{-1}K^{-1}) or alloys such as SnBi (T_{melt}=138°C, k≈20 Wm^{-1}K^{-1}).[21,22] However, these relatively low melting temperature materials have low mechanical compliance, leading to thermal fatigue in the IC due to the large mismatch in coefficients of thermal expansion between the IC components.[23,24] Gallium-based LMs are liquid near room temperature, which helps to alleviate the problems with thermal stresses.

Some studies have investigated increasing the wettability and thermal performance of the liquid metals with additives, chemical modification, and creating various alloys to improve its properties for use as a wet TIM.[15,25–28] Others have looked at making thermal pastes and circuits out of LM nano-dropets which can be ruptured and sintered into electrically conducting circuits.[29–31]

One major concern with gallium based LMs being used in TIMs for ICs is the rapid gallium induced degradation of many metals used in IC packaging.[32–34] This concern is particularly severe with aluminum (one of the most common heat sink materials), which becomes extremely brittle when exposed to gallium.[33] To prevent corrosion, the mating materials can be modified through surface treatments (e.g. anodizing or introducing a tungsten barrier layer[35]), but alternatively, gallium can be encapsulated and immobilized in a polymer matrix.

The use of liquid metals (LM) in soft polymer composites has recently been explored with focus on its electrical properties to be used as stretchable and wearable electronics[31,36–41] with some attention to the thermal benefits of LM-polymer composites.[36,42] Electrical properties are somewhat tunable and may rely on the size of the liquid metal inclusions. Composites are reported to be electrically conducting with LM inclusion diameters between 4-20μm[43] and electrically insulating

with diameters between 50nm-3μm.[36] While the size of LM inclusions is also expected to affect the elastic modulus of the composite, the thermal conductivity is affected very little – ranging from 1.4 $Wm^{-1}K^{-1}$ at sub 3μm diameter inclusions[36] to 1.5 $Wm^{-1}K^{-1}$ at 4-20μm inclusions.[42] The primary contributors that affect the thermal conductivity of the composites are the aspect ratio and volume fraction of the inclusions.[42] Using LM as filler in a polydimethylsiloxane (PDMS) matrix, Bartlett et al.[42] demonstrated that a high directional thermal conductivity of up to 10 $Wm^{-1}K^{-1}$ can be achieved by strain-induced spherical-to-cylindrical deformation of the microscale LM inclusions. Unfortunately, surface leakage of LM is a problem when composites with large LM inclusions[42,44,45] are cut or compressed (as with typical TIM applications). These types of mechanical forces drive the LM out of the polymer matrix and hence Ga-induced corrosion of adjacent materials is still a concern.

Very little research has been done using LM as a means to decrease the thermal resistance between solid metal fill. This works aims to fill that gap.

2.5 Polydimethylsiloxane as a Matrix

Polydimethylsiloxane (PDMS) is a common elastic polymer used in a variety of applications, from medical equipment to thermal interface materials. It is a cross-linked, silicone-based polymer and is commercially available from a number of manufacturers. Several models are available from each manufacturer so the properties can vary greatly, but this makes it easier to acquire a matrix material with the right characteristics. Furthermore, a lot of work has been done to evaluate the effects on modifying the mixing process in the fabrication of PDMS.

Sylgard 184, a PDMS from Dow Corning, has been reported to have the following physical properties: shear modulus between 100 kPa and 2 MPa, low glass transition temperature (-130°C),[46] and low change in shear elastic modulus versus

temperature (1.1 kPa/°C).[47] Liu et al. report a decrease in Young's modulus with increase in curing temperature and an increase in curing time, from 900 kPa at 100°C for 0.5 hours down to 400 kPa at 300°C for 3 hours.[48] Schnieder et al. and Dow Corning put the elastic modulus of Sylgard 184 at 1.8 MPa.[49,50] Sylgard 184 is reported to have a thermal conductivity of 0.27 by the manufacturer.[51] Most PDMS has a Mullins effect, which results in a change or relaxation of the modulus between the first and second loadings.[45,52]

Jeong et al. developed a simple process that tunes the properties of PDMS to make it more soft, stretchable, and sticky, making it ideal for epidermal electronics.[53] Wang et al. investigated the crosslinking effect of PDMS on the elastic modulus, from 5:1 all the way down to 33:1 cross linker ratio.[54]

The majority of the composites in this thesis use Smooth-on's EcoFlex 00-20, which is much more elastic and soft than Sylgard 184 and has k = 0.3±0.02 $Wm^{-1}K^{-1}$.

2.6 Theoretical Models for Composite Thermal Conductivity

Effective medium approximations (EMAs) for particulate laden composites can be generally categorized under:

1. Maxwell based model
2. Self-consistent (SC) model
3. Differential effective medium (DEM) model

Maxwell[55] based models lump dilute particulate ($\phi < 0.25$) into a single particle inside of a matrix of infinite extent. Therefore, the particles have no interaction between themselves. Rayleigh[56] based models take the particles or inclusions to be periodic, but still assume dilute concentrations. Some Rayleigh-based models take into account effects from particles in near contact. Hasselmann and Johnson[57] built

thermal boundary resistance into the Maxwell model and Nan et al.[58] adapted it for non-spherical particles. But all these still assume dilute concentrations ($\phi < 0.4$).

SC models appear to start with Bruggeman[59] and are expanded upon by Landauer.[60] They are "based on the approximation that the medium outside a particular type of inclusion can be considered homogeneous, the effective conductivity of which needs to be determined. SC approximations do not account for spatial distribution of the inclusions and are of questionable validity when applied to systems that do not possess phase-inversion symmetry."[61]

DEM models also appear to start with Bruggeman and are an asymmetric approximation scheme. They assume that the particles are added progressively to the matrix whose effective conductivity is known at any given stage. The Bruggeman asymmetric model (BAM) takes into account thermal boundary resistances and, "among classical EMT's, the Bruggeman scheme is considered the most accurate for high filler volume fractions."[17]

Tavangar[18] came up with a similar expression to the BAM, but went on to define the effective phase contrast, γ, as:

$$\gamma = \frac{k_c}{\left(1 + \frac{k_p R_b}{a}\right) k_m}$$

where a is the particle radius, k_p is the particle thermal conductivity, R_b is the interface resistance between particle and matrix, k_c is the thermal conductivity of the composite, and k_m is the thermal conductivity of the matrix. His equation is valid for the full range of γ (2 to 8), whereas the Hasselmann-Johnson model fails above 4 (as do most of the Maxwell based models).[17]

The Nielson model[62] is an empirical model popular in literature even though it doesn't include ITR. It was formulated for moderate filler fractions ($\phi < 0.4$) and becomes unstable at higher fill fractions.[63]

Bartlett et al.[42] use a modified Bruggeman equation to model LM inclusions that starts with a SC EMT that takes into account the shape of the ellipsoidal particles, L, where L is 1/3 for spherical particles:

$$\frac{k_c - k_m}{Lk_c + (1-L)k_m} = \phi \, \frac{k_p - k_m}{Lk_m}$$

This is good for dilute concentrations but to account for particle-particle interactions they turn it into a DEM. This model matches polymer composites with LM inclusions at $\phi = 0.5$. Table 2.2 details the equations of the most applicable models to estimate k_c for mostly spherical metal particles in a PDMS composite.

Table 2.2: Table of most applicable models for related composites.

Model	**Equation**	**Valid ϕ**
Bruggeman modified	$\left(\frac{k_p - k_c}{k_p - k_m}\right)\left(\frac{k_m}{k_c}\right)^L = 1 - \phi$	All
Tavangar	$1 - \phi = \frac{(k_m)^{\frac{1}{3}}\left(k_p k_c R_b + ak_c - ak_p\right)}{(k_c)^{\frac{1}{3}}\left(k_p k_m R_b + ak_m - ak_p\right)}$	All
Maxwell-Garnett with R_b (Hasselmann-Johnson similar)	$\frac{k_c}{k_m} = \frac{\left[k_p(1+2\alpha) + 2k_m\right] + 2\phi\left[k_p(1-\alpha) - k_m\right]}{\left[k_p(1+2\alpha) + 2k_m\right] - \phi\left[k_p(1-\alpha) - k_m\right]}$ $\alpha = \frac{2R_b k_m}{d}$	<0.4
Bruggeman Asymmetric	$(1-\phi)^3 = \left(\frac{k_c}{k_M}\right)^{\frac{1+2\alpha}{1-\alpha}}\left(\frac{k_c - k_p(1-\alpha)}{k_M - k_p(1-\alpha)}\right)^{\frac{3}{1-\alpha}}$	All

One variable that is hard to estimate in these models is R_b. R_b due solely to phonon acoustic mismatch is estimated on the order of 10^{-8} m^2KW^{-1} at room temperature,[16,64] providing a lower bound for this value. The contact resistance between Cu and Si at 300 K is around 4×10^{-4},[64] providing a loose upper bound. Prasher puts R_b between a polymer matrix and metal fillers of 10μm in diameter at

$5x10^{-6}$ m^2KW^{-1}.[16] Rai and Moore claim a chemically clean interface between PDMS and copper nanowires to have a boundary resistance of $3x10^{-7}$ m^2KW^{-1}.[65]

2.7 Liquid Metal Oxide Manipulation

The thickness of the oxide layer on LM in ambient conditions is typically 1-3 nm thick.[31,66,67] The oxide layer is strong enough to support free standing LM structures and is often referred to as a skin.[68] The oxide skin is amphoteric and can be thinned or removed in solutions with pH > 10 or pH < 3.[68]

The oxide skin helps to stabilize LM inclusions in a PDMS matrix and it facilitates the fabrication of such composites made by simple mixing with a mortar and pestle. A minimum of 1.7 MPa is required to rupture a composite structure of GaInSn droplets (2-30 μm diameters) in a PDMS matrix at ϕ=0.5 and induce electrical conductivity.[44]

LM droplets can be formed outside of a polymer matrix by sonicating bulk LM in various solutions,[31,40,69] shearing the LM into droplets,[30,70] or by forming droplets through microfluidic channels.[71,72] Forming LM droplets through microfluidic channels produces large, but stable, droplets with diameters on the order of 50-100 μm.[72] Sonication of bulk LM can produce much smaller droplets (< 30 μm). Increased sonication duration decreases LM droplet size from 13 μm with 2 minutes of sonication down to 1 μm with 60 minutes of sonication. The longer duration also increases the thickness of the oxide skin along with flaking nanoplatelets of LM oxide with average length and width of 200 and 50 nm, respectively. LM oxide nanoplatelets start to emerge after 5 minutes sonication in DIW.[69] The size of the LM droplets can be reduced down to an average diameter of 110 nm by using thiol ligands in an ethanol solution with a probe sonicator. Ren et al. report that the thiols create a 3 nm organic layer around the oxide skin, further stabilizing the LM

droplets.[31] Furthermore, Tevis et al. claim that shearing LM into droplets in acetic acid forms an organic layer on top of the oxide shell.[70]

Yamaguchi et al. show reversible size control of nanoscale LM droplets under ultrasonication (hone-type) with the use of thiols, acids, and temperature.[40] Thiols and acids are used together in order to controllably grow the LM droplets. Hydrochloric acid is effective for removing the LM oxide.[73,74]

The LM oxide is electrically insulating and the LM droplets must be merged together to create electrical circuits. A force of 50 nN is required to break through the oxide skin of a ligand stabilized LM droplet of 100 nm in diameter with an AFM tip (~80 kPa).[31] The size of the droplets affects the force required to rupture them.[37]

The formation of oxide is also detrimental to the thermal properties of LM. Li et al. show more than a 100% increase in thermal resistance in oxidized LM, as compared to bulk LM. They overcome this by adding 10wt% copper particles to the oxidized LM and bring the thermal resistance back down to near bulk LM.[27] Tang et al. show that adding 20vol% copper particles to a LM amalgam can more than double the thermal conductivity over that of the bulk LM and they provide a decent analysis on the subsequent alloying of Cu and Ga.[75]

2.8 Stepped Bar Apparatus and ASTM D5470 standard basics

I oversaw the design, fabrication, and calibration of a stepped-bar apparatus (SBA),[76,77] which is based on the ASTM D5470 standard[78] for measuring the thermal resistance of thin materials. This SBA was used in this research as the primary source of thermal characterization. Our custom SBA includes a linear encoder and a load cell that measure sample thickness and pressure during the thermal resistance measurements. Measuring thermal conductivity fundamentally requires applying a known heat flux to a sample of known geometry and then measuring the

temperature drop across the sample. In this method, a steady state temperature gradient across the sample is created using a heat source and a heat sink. The sample is placed between two metallic reference bars of known cross-sectional area and thermal conductivity. To minimize errors from misalignment, the top bar has a larger cross-section than the bottom bar.[76] The temperature distribution in the reference bars (measured via thermocouples in precision-machined holes along the reference bar lengths) is then used to measure the heat flux, q, in the bars. Because the system is well insulated, the measured heat flow through the bars is equal to the measured heat flow through the sample. Extrapolating the temperature distributions of the reference bars to the bar-sample interfaces allows the temperature drop across the sample (ΔT) to be determined. The measured thermal resistance (R_{th}) across the sample is then found with

$$R_{th} = \frac{\Delta T}{q}$$

This thermal resistance represents the summation of the sample's intrinsic thermal resistance (R_s) as well as the thermal contact resistance (R_c) between the sample and the reference bars (note that R_c is the sum of two contact resistances, the contact resistance between the top reference bar and the top of the sample and the contact resistance between the bottom reference bar and the bottom of the sample). The samples are under pressure during thermal resistance measurements to minimize R_c, which will bring k_{eff} closer to the true k of the composite. Various loads are used to gauge sample properties, but the target pressure for the results of this study are 5-150 psi, the pressure range applicable to electronic cooling.[6]

With R_{th} and t_c known, the effective thermal conductivity can be calculated by:

$$k_{eff} = \frac{t_c}{R_{th}} = \frac{t_c}{R_c + R_s}$$

This effective thermal conductivity includes the combined effects of the intrinsic sample resistance and the sample contact resistance. Consequently, the effective thermal conductivity is smaller than the intrinsic sample thermal conductivity.

The sample temperature drop is determined by extrapolating the linear temperature distribution from the bottom bar to the bottom of the sample and a 2nd order curve fit from the end of the top bar to the top of the sample, as outlined by Thompson.[79] This method of using a 2nd order fit for the end of the top bar was used primarily to be consistent with the method laid out by Thompson, but the difference in using a 2nd order fit vs a 1st order fit is generally small (< 2%) for our samples. The heat flux through the reference bars is determined from the slope of its temperature distribution (i.e., Fourier's Law), as described by a linear fit through the measured temperatures in the bars. Only the upper portion of the top bar is used in the fit to calculate the heat flux in order to avoid any effects from the interface with the sample – though no effects have been specifically identified. Figure 2.3a demonstrates these principles as it applies to the stepped bar apparatus. Figure 2.3b presents measured values for small LM inclusions in PDMS at various values of ϕ, following the procedure as outlined by Jeong et al.[36] along with their reported results. The slight difference in values can be traced back to the k of the polymer matrix. They measure k_{PDMS} = 0.17 $Wm^{-1}K^{-1}$ and I measure k_{PDMS} = 0.27 $Wm^{-1}K^{-1}$, which difference follows through the rest of the values in the data. The difference in measured values of the PDMS could be due to difference in polymer or measurement technique. They used Elastosil RT 601 and I used Sylgard 184. They used xenon flash to measure thermal diffusivity and converted that to a thermal conductivity whereas I measured thermal resistance and sample thickness with a SBA to get thermal conductivity.

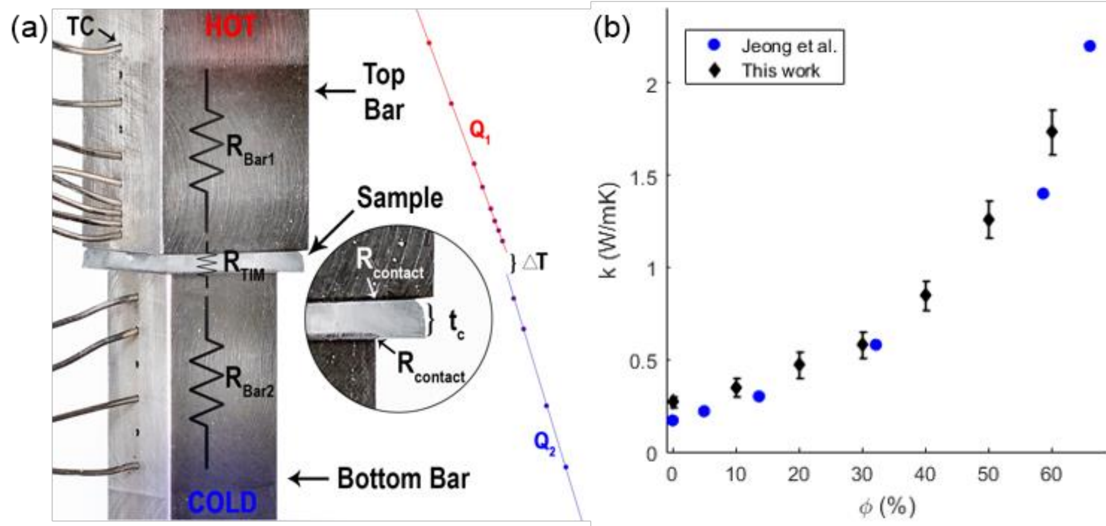

Figure 2.3: (a) Measurement principles of the ASTM D5470 standard. (b) Our results with well dispersed LM inclusions validated against Jeong et al.[36]

I estimate that the overall measurement uncertainty in k_{eff} from our SBA ranges from 4 to 6% (relative, 68% confidence).[77] Additional uncertainty arises as the thermal conductivities of the sample and reference bars become more similar, and this corresponds to the higher end of the previously mentioned uncertainty range. I validated our thermal conductivity measurements against literature results on PDMS-liquid metal composites[36,42] with good agreement. The measured Sylgard 184 thermal conductivity of 0.27 ± 0.01 $Wm^{-1}K^{-1}$ also matches well with the thermal conductivity stated by the manufacturer (Sylgard 184), 0.27 $Wm^{-1}K^{-1}$.[51]

CHAPTER 3

MAGNETIC ALIGNMENT IN PARTICLE-LADEN SOFT POLYMER COMPOSITES

3.1 Introduction

This chapter focuses on the benefits and pitfalls of using magnetic alignment to enhance the directional thermal conductivity of particle-laden polymer composites. The published work in Appendix C, titled "Buckling of Magnetically-Formed Filler Fiber Columns under Compression Increases Thermal Resistance of Soft Polymer Composites",[80] provides most of the novel research contributed in this chapter. As the first author on this paper, I was the main contributor in both research and writing. Some of the material in this chapter also came from the accepted manuscript in Appendix E, titled "Thermal Conductivity Enhancement of Soft Polymer Composites through Magnetically-Induced Percolation and Particle-Particle Contact Engineering".[81] Additional background and a more detailed literature survey are included in this chapter to provide a more complete work on the topic.

3.2 Magnetic Alignment to Enforce Percolation

The thermal conductivity of particle-laden polymer composites increases almost linearly with increasing particle fill volume fraction, ϕ, until the percolation threshold (ϕ_p), is surpassed. Above ϕ_p, much greater returns are achieved by increasing ϕ. The percolation threshold is the point where a single network of connected particles spans the entire length of the composite. It is most easily observed by measuring the electrical resistance or conductivity of a composite. The composite will go from electrically insulating below the percolation threshold to electrically conducting above it.[82,83] This threshold can be as low as ϕ = 0.01 for

specialized high aspect ratio fill such as nanowires,[84,85] but it is typically around ϕ= 0.3 for more cost-effective spheroidal particles.[86–88] Unfortunately, major increases in the composites thermal conductivity are usually achieved well above the percolation threshold ($\phi \geq 0.5$), which can degrade the mechanical properties of the composite as well as increase R_c at its interfaces.[16,89] Operating above the percolation threshold creates more direct contact between multiple filler particles within the matrix and shifts the governing thermal boundary resistances from the matrix-particle interfaces (R_{mp}) to particle-particle interfaces (R_{pp}).[82] One way this shift to R_{pp} limited boundary resistances can be achieved at lower ϕ is by aligning the fill material in the matrix. While many methods can be used to align the fill,[90–97] I focus on using an external magnetic field to align particles and enforce percolation through the matrix.

3.3 Previous Work

Imposing a magnetic field on an uncured polymer is a simple and cost-effective method of directing the spatial arrangement of magnetic particles within the matrix, leading to highly anisotropic electrical and thermal conductivities in the composite. This process has been utilized since the 1980's when Jin et al. showed that magnetic alignment of electrically conductive particles in a non-conducting matrix can be used to make an anisotropic composite that conducts electricity only along the aligned particle columns.[98,99] There have been many demonstrations of altering electrical properties of composites using magnetic alignment since then,[100–102] but it was not until more recently that the thermal ramifications of this procedure have been studied. Specifically, Martin and Gulley[103] and Su et al.[104] show that the magnetic alignment of 2 - 7 diameter nickel particles doubles the thermal conductivity a polymer composite. Furthermore, several authors, including Solis and Martin,[105] Yuan et al.,[106] Martin and Snezhko,[107] and others[108–110] have shown that aligning higher aspect ratio particles

can produce even higher enhancements in directional thermal conductivity. Martin and Snezhko[107] concluded that applying a magnetic field leads to the formation of an optimal composite structure for thermal transport by minimizing the magnetostatic energy and maximizing the permeability and, thus, the thermal conductivity.

However, most TIMs operate under various amounts of load and compression. The effects of compression on magnetically aligned, particle-laden soft composites had not previously been investigated. In this chapter, I use an applied magnetic field to align nickel fibers with an aspect ratio of 7 in a soft polymer composite and evaluate the effects of compression on the aligned polymer composites.

3.4 Methods

Details on composite fabrication, materials, and methods used in this work can be found in the published and accepted manuscripts (Appendix C and Appendix E) and further information is supplied in the supporting information of each respective manuscript.

3.5 Results and Discussion

Using large nickel fibers (50 μm wide × 20 μm thick × 250 μm long) results in a maximum packing factor (ϕ_{max}), of 0.35.[111] As ϕ approaches ϕ_{max} there is less space between fibers for them to reorient and align with the applied magnetic field. The maximum composite thermal conductivity for the aligned composite was at ϕ = 0.15 and reached k = 2.1 $Wm^{-1}K^{-1}$. This is also where the greatest increase due to magnetic alignment was observed (compared to the unaligned composite). Using spherical nickel particles (21 μm average diameter) in the soft polymer matrix reaches a theoretical ϕ_{max} closer to 0.6. Experimentally, the highest k for these

composites was observed at ϕ = 0.5 (the highest ϕ that was fabricated and measured) and reached k = 2.9 $Wm^{-1}K^{-1}$ for the aligned composites. Magnetic alignment increased the composite thermal conductivity by 0.6-0.8 $Wm^{-1}K^{-1}$ for ϕ = 0.2 – 0.4 and 0.4 for ϕ = 0.1 and 0.5. Thus, the largest increase in k due to magnetic alignment happens near $\phi_max/2$, where there is sufficient space for the particles to rearrange and at high enough ϕ to create continuous percolating networks through the thickness of the composite. Furthermore, high aspect ratio fill do not have their highest k at the highest ϕ - like spheroidal fill particles - but rather max out near $\phi_{max}/2$. This is due to the decreased number of high resistance particle-matrix interfaces when high aspect ratio fill are aligned, end-to-end through the composite.

When both aligned nickel particle composites and aligned nickel fiber composites are compressed at low ϕ, the thermal resistance, R_{th}, of the composites actually increases as compressive strain, ϵ, increases. For both aligned systems, there is a threshold, ϕ_t, near $\phi_{max}/2$ below which R_{th} increases with increased ϵ and above which R_{th} decreases with increased ϵ. Below ϕ_t the aligned particle columns bend out of plane with the heat gradient, which transitions the mode of heat transfer from parallel along the aligned particle columns through the polymer matrix at ϵ = 0 to more of a series representation at higher ϵ. Above ϕ_t there is not enough space between aligned particle columns for them to bend out of plane without contacting and connecting with adjacent columns.

3.6 Conclusions

Magnetic alignment of high k fill in a soft polymer composite can dramatically increase the composites thermal conductivity, often by 2-, 3-, or 4-fold over the

unaligned composite when higher aspect ratio fill are used. Additionally, aligning high aspect ratio fill can enable higher thermal conductivities at lower ϕ – preserving many of the desirable mechanical properties of the soft polymer matrix that are lost when nearing the maximum packing limits of the fill material (lower young's modulus, lower contact resistance, etc.). However, aligning the fill at low ϕ can have negative thermal side effects when using the composites under high strain. Thus, an optimum balance of thermal and mechanical performance is achieved in these aligned composites near $\phi_{max}/2$.

CHAPTER 4

PARTICLE-PARTICLE CONTACT ENGINEERING

4.1 Introduction

Chapter 3 discussed how magnetic alignment can enforce percolation and increase particle-particle contact in the polymer composite. This chapter revisits magnetic alignment, but takes it one step further to use contact engineering to decrease the resistance between the aligned particles. In this chapter, I show that metal-metal interfaces have low boundary resistance and then use silver- and liquid metal-coatings on nickel particles to decrease the thermal boundary resistance at the particle-particle interfaces.

The majority of the work on this topic has been accepted for publication to Advanced Materials Interfaces with the title "Thermal Conductivity Enhancement of Soft Polymer Composites through Magnetically-Induced Percolation and Particle-Particle Contact Engineering."[81] The accepted manuscript is in Appendix E. Further work on this topic is included in Appendix D and is titled, "In Situ Alloying of Thermally Conductive Polymer Composites by Combining Liquid and Solid Metal Microadditives".[112] Additional background and a more detailed literature survey are provided in this chapter along with a summary of the results and conclusions.

4.2 Low Metal-Metal Thermal Boundary Resistance

In Chapter 3, magnetic alignment was used to connect particles together and enhance the thermal performance of the polymer composite. In this section, copper particles are used with LM in a polymer composite to demonstrate how metal-metal interfaces have lower R_b than metal-polymer interfaces. Copper was chosen for this

study because LM will readily wet and stick to copper. In fact, copper and gallium rapidly alloy and form $CuGa_2$ (see Appendix D for details).

The Cu and LM are mixed together prior to adding it into the polymer matrix to form various sized LM-Cu fill. When the copper and LM mixture is well dispersed, k_c is similar to a copper-polymer composite with no LM. But when large Cu-LM clusters are allowed to persist within the polymer matrix, as illustrated in Figure 4.1, k_c then can exceed that of copper alone.

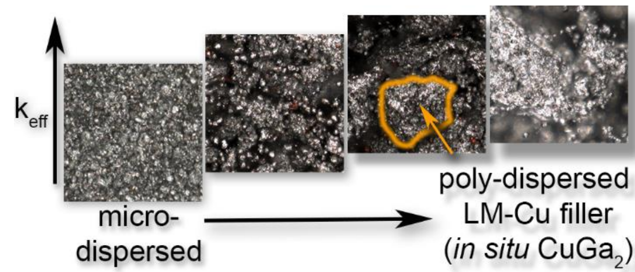

Figure 4.1: Schematic showing how large, poly-dispersed, LM-Cu fill increases k_{eff}.

Figure 4.2 presents the thermal performance of the LM-Cu-polymer composite as the size of the poly-dispersed LM-Cu filler increases ($PAD_{50\%}$ is a measure of how large the clusters are. See full article in Appendix D for details) at ϕ = 0.5 ($\phi_{LM} = \phi_{Cu}$ = 0.25). As the figure details, the larger the clusters of connected LM-Cu fill, the higher the effective thermal conductivity of the composite. Extracting the R_c from these measurements provides estimates for the bulk composite thermal conductivity of nearly 20 $Wm^{-1}K^{-1}$. This highlights the fact that metal-metal interfaces have much lower interfacial boundary resistance than metal-polymer, oxide-polymer, and oxide-oxide interfaces. This fact provides the basis for the assumption that soft and liquid metal coatings to connect particles can boost can dramatically decrease R_b overall.

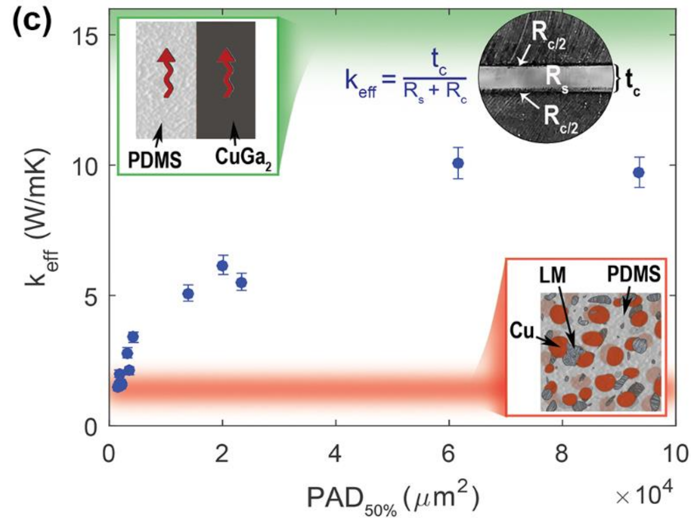

Figure 4.2: Effective thermal conductivity of LM-Cu-polymer composites plotted against the size of poly-dispersed LM-Cu filler at $\phi_{LM} = \phi_{Cu} = 0.25$.

These LM-Cu-polymer composites may be useful for certain applications, but because of the rapid alloying of the Cu and Ga, they stiffen more than a Cu-only polymer composite. Additionally, because of their unique processing, it is difficult to repeatably produce high k composites. Thus, magnetic alignment is now used to provide a more repeatable process and metal particle coatings are used to lower R_b.

4.3 Silver-Silver Interfaces

Because of its high thermal conductivity and non-oxidizing surface,[113,114] silver is a unique and attractive fill material for polymer composites. Even dispersed silver nanowires alone provide impressive thermal conductivity enhancement at very low ϕ[115] that can be improved on by thermal (at 150°C)[116,117] or microwave[118,119] sintering of the nanoparticles inside the matrix material. This significant enhancement in k_c by sintering or welding the silver particles is caused by an increase in the interfacial area between particles, and thus a considerable decrease in R_{pp}. This decrease in R_{pp}

dramatically improves conduction across the percolation network in the thermally insulating matrix material, reportedly by up to 40 times in the case of microwave welded silver nanowires.[119]

Some research even suggests that mechanical stress on silver particles is sufficient to mechanically weld the particles together, producing similar enhancements to the composites thermal conductivity as thermal and microwave sintering.[120] This suggests that good contact between silver interfaces along with the application of moderate mechanical force is sufficient to create decently conductive bonds between particles. This sintering and welding (electrical and mechanical) of the silver fill is enabled by the oxide-free,[113,114] soft[121] surface of silver. In this chapter, I leverage these unique silver-silver interface characteristics without the high costs of pure silver particles by using silver coated nickel particles.

4.4 Liquid Metal in TIMs

Liquid metals (LMs), such as eutectic GaIn and GaInSn, with melting temperatures near or below room temperature, have potential uses in flexible electronics, electronic packaging, and TIMs,[15,26,35,122–124] but their integration can be challenging due to their low viscosity, high surface tension, and rapidly oxidizing surface. Consequently, LMs often require a modification prior to use.[68] For example, more user-friendly LM pastes with improved mechanical, thermal, and electrical properties can be made by dispersing small amounts of solid metal particles in the LM base.[27,75,125,126] The liquid nature of these alloys and their composites enable them to conform to surface roughness and compress under loads to decrease thermal resistance. But these options are still susceptible to pump-out and have possible corrosion issues, depending on the material of the mating surfaces.[34]

LM has also been incorporated in a polymer matrix, showing promise in raising k, eliminating pump-out issues, and decreasing the risk of Ga-induced corrosion. But well dispersed LM inclusions in a polymer matrix still have a high potential for LM leakage and only raise k_{TIM} to 1.5 $Wm^{-1}K^{-1}$.[36]

Thus, similar to the silver coatings on the nickel particles, I use the LM to reduce the thermal resistance between solid metal particles. Unlike many previous studies that disperse solid metals in the LM, however, I disperse small amounts of LM into solid metal powders to produce LM coatings on the nickel particles. Since the oxidation of the LM has been shown to aid in wetting other metals, I mix the nickel powder with various amounts of LM with a mortar and pestle in an air environment.[27,125]

4.5 Methods

Nickel particles (average diameter of 21 μm) with silver coatings of 350nm, 750nm, and 850nm are evaluated against bare nickel particles and galinstan-coated nickel particles. Details on composite fabrication, materials, and methods used in this work can be found in the submitted manuscript (Appendix E) and further information is supplied in the supporting information of the respective manuscript.

4.6 Results and Discussion

The silver-coated nickel particles provide more than a 4-fold decrease in thermal resistance in a dry powder bed, even at pressures as low as 300 kPa. The silver-silver interfaces reduce the thermal boundary resistance at the particle-particle interfaces by deforming and increasing the interfacial area between particles. Magnetically aligned in the polymer matrix, these silver-coated nickel particles

produce a 1.8-fold increase in composite thermal conductivity over the aligned bare-nickel composites.

The LM-coatings on the nickel particles produce similar results to the silver-coatings, but require higher volumes of LM for similar boosts in composite thermal conductivity. This effect most likely stems from the presence of gallium oxide, which naturally forms when LM is exposed to air. This highly elastic, few nanometer thin oxide layer is prone to nanoscale and microscale wrinkling.[127,128] Thus, it likely provides an inferior geometrical contact between particles than the oxide-free silver coatings. Furthermore, the thermal conductivity of single crystal gallium oxide is much lower (13 $Wm^{-1}K^{-1}$)[129] than gallium (29±3 $Wm^{-1}K^{-1}$) and galinstan (25.4 $Wm^{-1}K^{-1}$)[130]. The oxide shell will be amorphous, resulting in an even lower thermal conductivity. In fact, Li et al. show more than a 100% increase in thermal resistance in oxidized LM, as compared to bulk LM.[27] The gallium oxide that forms between LM-coated nickel particles will act as a moderately-high thermal resistance at the particle-particle interface. Only when multiple nickel particles are encased within a single LM-oxide shell is a significant decrease in boundary resistance achieved.

4.7 Conclusions

The nearly oxide free silver-silver interfaces provide significantly less thermal resistance than nickel-nickel interfaces by deforming under low pressure and increasing the interfacial area between particles. This produces a significant increase in composite thermal conductivity when particle-particle contact is maximized through magnetically enforced percolation, achieving k = 3.7 $Wm^{-1}K^{-1}$ at $\phi = 0.4$.

The oxidation of the LM facilitates the wetting of the LM onto metal particles, but also has a negative effect on the thermal performance of the composite. The

following chapter will go into more detail of the thermal properties of the oxide on liquid metal droplets and the thermal ramifications of rupturing that oxide.

CHAPTER 5

THERMAL RAMIFICATIONS OF OXIDE RUPTURE

5.1 Introduction

As highlighted in the previous chapter, the oxide skin on the liquid metal is a major thermal bottleneck when using the LM to connect solid metal particles together inside the polymer matrix. As long as the particles are connected inside the oxide shell, it provides significant thermal conductivity enhancements. In this chapter, I seek to understand and overcome the negative effects of the gallium oxide shell by mechanically rupturing it and measuring, in situ, the thermal resistance.

5.2 Popping LMDs

I start by evaluating the force required to pop various sizes of LMDs and their thermal and electrical resistance as they are compressed. The size of the LMD and thickness of the oxide are the two main parameters that dictate how much force is required to pop them. Inside of a polymer matrix, large LMDs (2-30μm diameter, GaInSn) require 1.7 MPa to rupture and induce electrical conductivity.[44] Nano-LMDs (600nm diameter, EGaIn) require 500 nN to pop individual droplets.[37] But popping LMDs really comes down to applying enough pressure to achieve sufficient strain on the oxide to push it to failure. The ultimate tensile strength ($\sigma_{UTS)}$, of $\beta - Ga_2O_3$ in the [100] direction is calculated to be 27 GPa @ $\epsilon = 0.17$. Failure is around $\epsilon = 0.32$,[131] which coincides with previous computational models of fluid filled microcapsules that rupture near the elastic regime, though experiments produce slightly lower strain at failure.[132] This discrepancy between computation and experiment may be caused by increased stresses due to friction.[133] However, it has been reported that a bed of

nano-LMDs, rather than individual particles, is expected to rupture closer to ϵ = 0.44.

Assuming LMDs can be modeled as spherical thin-walled pressure vessels, the stress in the oxide shell can be simplified to

$$\sigma = \frac{Pr}{2t}$$

where σ is tensile strength of the oxide shell, P is pressure, r is the radius of the LMD, and t is the thickness of the oxide shell. Assuming the pressure inside the LMD is equal to the force applied to the outside of the LMD during compression, the pressure required to pop these LMDs is then

$$P = \frac{\sigma 2t}{r}$$

Figure 5.1 shows that as the UTS gets smaller, there is still a sharp increase in P at some critical diameter, d_c. For use in TIMs, it is desirable for the oxide on the LMDs to rupture under low pressures. Therefore, it is necessary to stay above d_c in order to remain in the zone of low-pressure oxide rupture for any given σ_{UTS}.

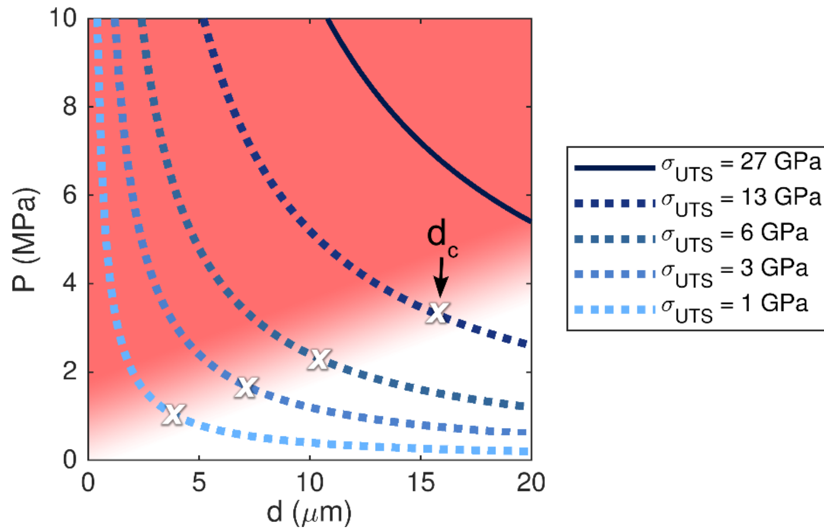

Figure 5.1: Pressure (P) vs LMD diameter (d) for various ultimate tensile strength values of the oxide shell when modeling the LMDs as thin walled, spherical pressure vessels. The red-shaded zone indicates where the pressure increases steeply as diameter is decreased

and the x's indicate the critical diameters for each plotted σ_{UTS}. The thickness, t, of the oxide shell is held constant at 1 nm.

The first goal of this preliminary research is to identify if a bed of LMD's will follow the trend set forth in Figure 5.1 as the individual LMD oxide shells are pushed to failure. The second is to validate the literature derived value for σ_{UTS} of the gallium oxide shells at 1 GPa.[37] From there, chemical modifications will be made to the oxide shells during LMD fabrication to modify the strength of the oxide. If the strength of the oxide can be controlled, then so can the pressure at which the LMDs rupture.

Previous work has been done using various methods to modify the oxide of gallium-based liquid metals, including: thiols,[31,40,134] hydrochloric acid,[40,73,135,136] acidic siloxanes,[137,138] electrolyte solutions and an applied voltage,[71,139] acetic acid,[140] phosphonic acids,[141,142] amino silanes,[143] and polyvinyl alcohol.[144] Additional studies have shown that the oxide thickness continues to grow and stabilize over several weeks, but that thiols can help minimize the growth by binding to the gallium, modifying the work function and minimizing the surface-accessible gallium.[134] The preliminary studies in this chapter will focus on the effect of dodecanethiol – in conjunction with hydrochloric acid - in modifying the strength of the oxide layer on LMDs.

Additionally, solid metal particles will be addedto the mix in an effort to provide more points of stress on which to pop the oxide shells. All of this knowledge can then be used in designing soft polymer composites with LMDs or LM-coated particles as fill with the intent to rupture oxide shells before or during TIM application to enhance thermal performance.

5.3 Methods

Liquid Metal Droplets (LMDs)

To simplify the system and isolate the effects of the oxide, I study various sizes of liquid metal droplets (LMDs) packed together in a dry particle bed. LMDs are fabricated similar to previous works by sonicating bulk gallium in ethanol.[31,40,69,145] Specifically, 0.4 mL of liquid gallium is placed in a 40 mL vial with 35 mL of ethanol. This solution is sonicated in an ultrasonic bath (Branson 1800) for 45-60 minutes, depending on the target size of droplets. Longer sonication times produce larger volumes of smaller LMDs. Various size distributions of LMDs are then separated through the use of sedimentation. The ethanol solution of LMDs is shaken to suspend all the particles and the larger particles will fall faster than the smaller ones. The smaller LMDs can be siphoned off the top after a desired amount of time and the larger particles can be collected from the bottom of the vial, as illustrated in Figure 5.2. Repeating this process three times, then repeating with the new vial of LMDs made it possible to further refine the LMD distributions. Various sedimentation times were used to produce LMD size distributions. Figure 5.3 provides the size distributions obtained from the following sedimentation times ranging from one minute to over 8 hours (1-2min, 2-6min, 10-20min, 90-180min, > 8hrs).

After making the desired distributions of LMDs, each suspension was drop-cast directly onto the bottom reference bar of the SBA, as illustrated in Figure 5.4a. This process was repeated 4-6 times to create a bed of LMDs between 500 and 1500 μm thick on the SBA reference bar. A Teflon gasket, polymer seal, and electrical tape retain the suspension on the reference bar while the ethanol evaporates (shown in Figure 5.4b), leaving the bed of LMDs behind.

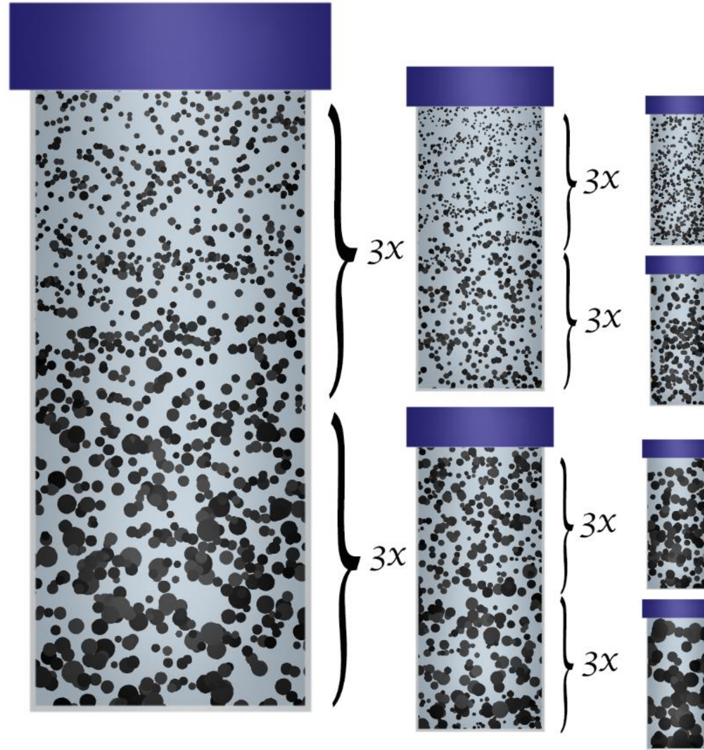

Figure 5.2: Illustration showing how sedimentation followed by siphoning off the top suspension and repeating can create multiple LMD size distributions.

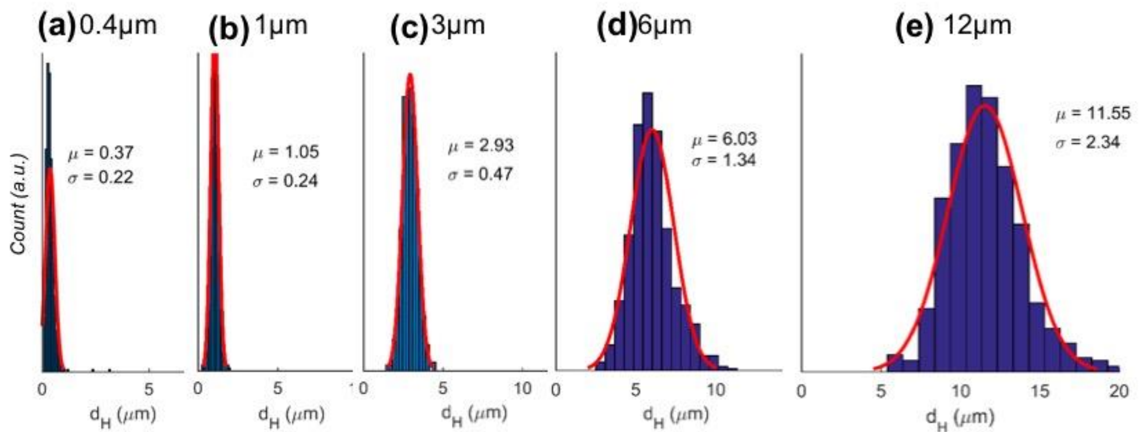

Figure 5.3: Several example LMD size distributions after the sedimentation and segregation process.

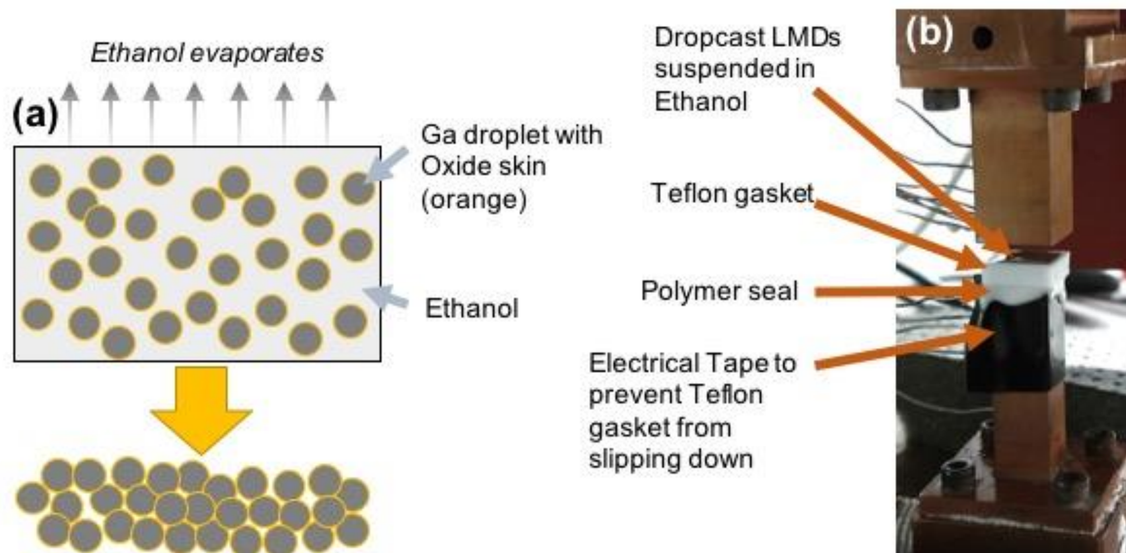

Figure 5.4: (a) Illustration of the drop cast process to create beds of LMDs and (b) an image showing the drop-cast suspension of LMDs and the Teflon gasket, polymer seal, and electrical used to retain the solution while the ethanol evaporates.

After the bed of LMDs is complete, the electrical tape is removed to allow the Teflon gasket to slide along the reference bar as the top bar is brought down into contact with the bed of LMDs. The bed of LMDs are compressed between the reference bars of the SBA and the thermal and electrical resistance is measured at various pressures. This results in measured thermal resistance values as the thickness decreases, as demonstrated in Figure 5.5b. At the top-right of this plot, the first few measurements are of uncompressed beds of LMDs, as shown in Figure 5.5a. The insets in Figure 5.5b illustrate how the LMDs (1) start as uncompressed mixtures of gallium droplets with gallium oxide shells in air, then (2) compress together, (3) start popping, and (4) end up with the liquid gallium flowing out from between the reference bars, leaving behind fragments of the solid oxide shells. Figure 5.5c shows the same bed of LMDs after compressing. From this image the empty gallium oxide shells are visible as flattened husks. Figure 5.5d shows the corresponding thermal

conductivity of the bed of LMDs. As the LMDs compress, they start to pop, increasing the thermal conductivity of the beds by displacing air between LMDs and by creating percolating networks of flowing liquid gallium. The peak in k signifies the majority of the air has been replaced by liquid gallium. The subsequent decline in k as the thickness decreases further marks the event of liquid gallium escaping out from between the reference bars, leaving behind a higher ratio of the lower thermal conductivity gallium oxide to the higher conductivity liquid gallium.

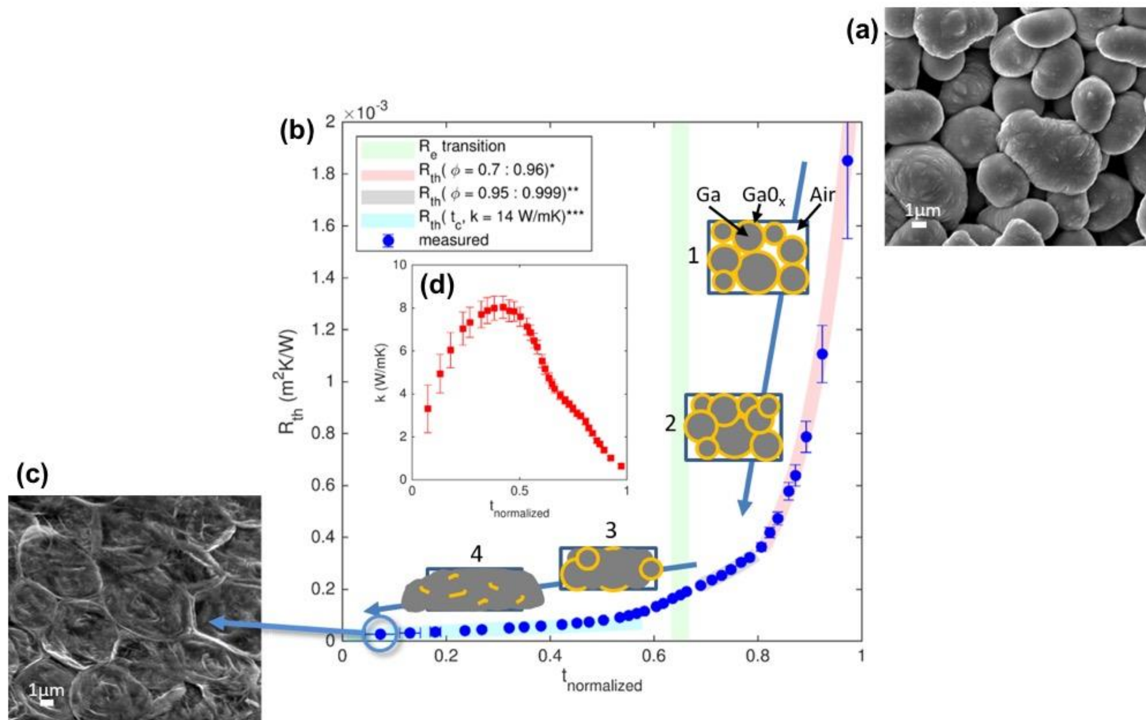

Figure 5.5: (a) SEM of the bed of LMDs prior to compression, (b) the raw thermal resistance data as the thickness is decreased with illustrations inset showing the process of popping the LMDs as well as some theoretical approximations fit to the data, (c) SEM of the fully compressed remains of the bed of LMDs showing the leftover gallium oxide husks, and (d) the corresponding thermal conductivity of the bed of LMDs under compression.

As the size of the LMDs decreases, the pressure required to pop them increases. The SBA used in this work was equipped with a load cell with a maximum

load of 500 N. Thus, the maximum pressure applied to these LMDs was 4 MPa – not high enough to rupture some of the smaller LMDs. Figure 5.6 presents SEM images of the uncompressed and fully compressed remains of a few size distributions of LMDs. These images show that LMDs smaller than 1 μm in diameter remain unruptured but the entire bed of larger LMDs are ruptured after measurement in the SBA.

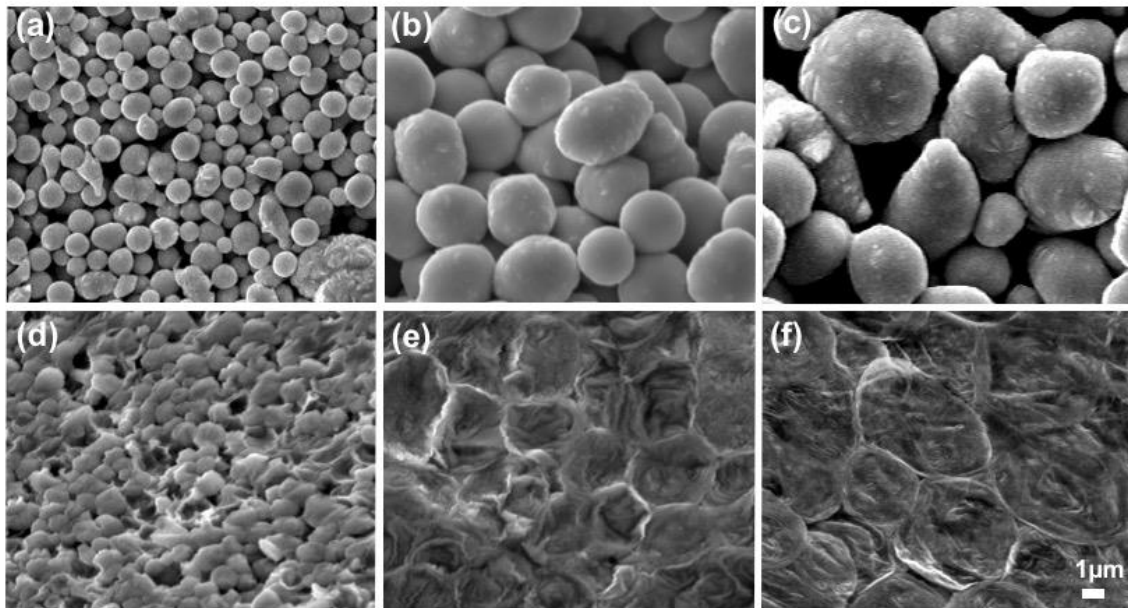

Figure 5.6: compressed and uncompressed beds of LMDs for the 1, 3, and 6 μm LMD distributions in Figure 5.3.

The temperature of the bottom ref bar was set to 30°C, just above the melting point of bulk Gallium, even though studies have shown the melting point to be much lower for Gallium droplets – as low as -14°C for gallium nanodroplets.[40,146]

Tungsten Particles and LMDs

To provide more stress points for the LMDs to pop and to try and further increase the thermal conductivity of the LMD beds, I dispersed tungsten particles in

with the LMDs prior to drop casting onto the SBA and measuring the thermal properties. I used two different sizes (0.4-1 μm and 12 μm) of tungsten particles with the LMDs in the ethanol solution at various volume ratios of tungsten to gallium. Tungsten was chosen because it is one of only a few metals that have no chemical reactions with gallium.

Chemical Modifications

Using the unmodified LMDs as a control, both thiolated LMDs and HCl-treated thiolated LMDs are studied. The process to make the HCl-treated thiolated LMDs is as follows:

i. Bring Ga and ethanolic thiol solution to temperature (36°C)
ii. Add 0.4mL Ga into 35mL ethanol with 10mM concentration of C12SH (in a 40mL vial)
iii. Sonicate @ 36°C for 50 minutes (form LMDs with thiol-coated oxide)
iv. Let the LMDs sediment and cool for 15 minutes
v. Add solution to 35mL of 10mM HCl in ethanol to achieve a final concentration of HCl of 5mM
vi. Split solution into 2 × 40mL vials and sonicate at room temperature for 10 minutes to etch the Gallium oxide with the HCl
vii. Sediment and rinse with ethanol at the 2-4 minute time interval to extract LMDs with an average diameter of 8μm and remove HCl and excess thiols
viii. Drop cast and measure thermal properties

The thiolated LMDs and the control LMDs follow the same procedure with the absence of HCl and thiols, respectively.

Based on previous works,[40,134] the thiols will bond to the gallium, hindering to some degree the formation of Ga_2O_3 (the most common oxide in LMDs), and the HCl will etch the oxide out from under the thiols, allowing the thiols to further bind and cover the exposed gallium, as illustrated in Figure 5.7a. The three configurations tested in this chapter are illustrated in Figure 5.7b, c, and d.

The age of the LMDs also plays a role in how thick the oxide layer grows to be.[134] Thus, some of the variation in these results may be from slight differences in LMD age due to timing constraints in fabrication and measurement.

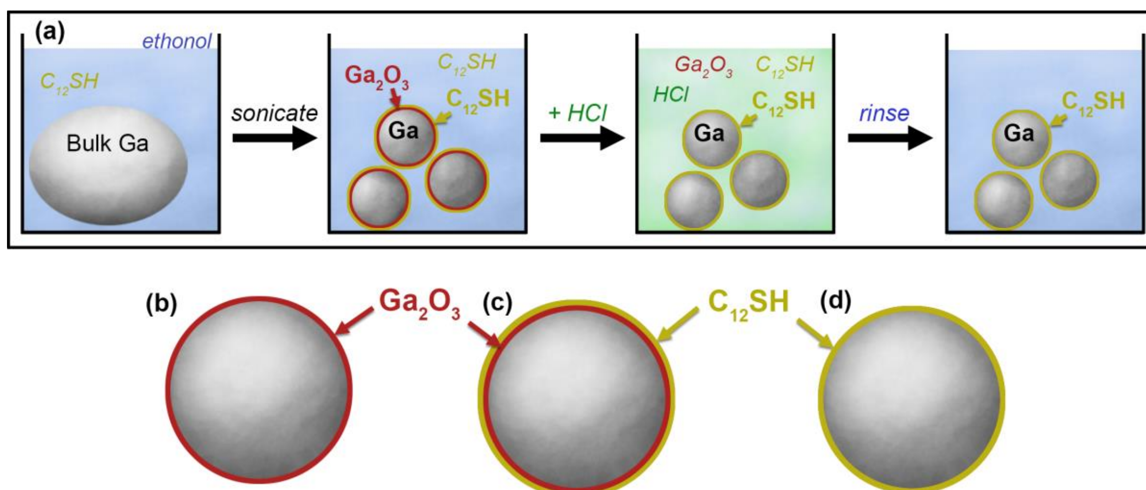

Figure 5.7. (a) process in which thiols and HCl are combined to obtain relatively oxide-free LMDs and the three resulting configurations that are tested herein, namely: (b) LMDs with native oxide (control), (c) thiolated LMDs, and (d) thiolated LMDs with oxide removal

5.4 Results and discussion

Size of LMDs

The results follow the expected trend that larger LMDs require less force to deform and rupture (compressing elastic capsules).[147] Figure 5.8a details the thermal conductivity of beds of various average diameter LMDs as the pressure increases and the beds are compressed. The larger diameter LMDs reach a k_{max} at much lower pressures than the smaller diameter LMD beds. Specifically, the 12 μm average diameter LMD bed reached a k_{max} of 8 $Wm^{-1}K^{-1}$ at a pressure of less than 1 MPa; the 0.4 μm average diameter LMD bed barely got above 1 $Wm^{-1}K^{-1}$ at 4 MPa (the maximum pressure measured on the SBA). Figure 5.8b details the thermal conductivity at a pressure of 0.75 MPa and the k_{max} value versus the average LMD diameter. Figure 5.8c plots the pressure at k_{max} for each LMD distribution versus the average diameter of the distribution on top of theoretical values for the failure of

thin-walled pressure vessels, discussed previously. The shaded region uses values from literature for σ of 1 GPa[37] and t of 0.5-2.5 nm.[66,67,127,134,148–150] Also shown in the figure are some values of rupturing nano-LMDs by Boley et al.[37] as well as the pressure values at which the samples in this study transitioned from electrically insulating to electrically conducting.

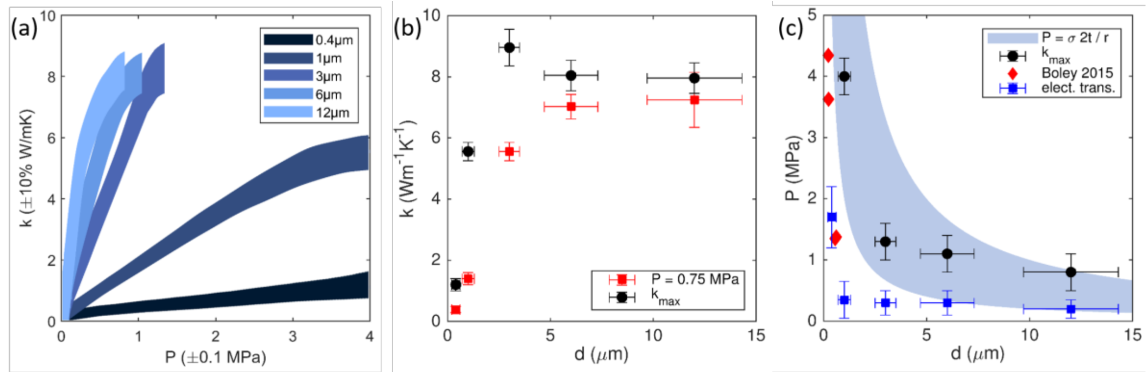

Figure 5.8: (a) Thermal conductivity (k) versus pressure (P) as the beds of LMDs are compressed for five different size distributions of LMDs (the distributions are shown in Figure 5.3), (b) k versus average LMD diameter at a pressure of 0.75 MPa and at $k_{\max}$ in (a), and (c) experimental data of pressure at $k_{\max}$ in (a) versus the average LMD diameter overlaid on theoretical values for thin-walled pressure vessels at failure assuming an oxide ultimate tensile strength, σ = 1 GPa, and a thickness of 1-3 nm. Also included in this plot are values for when the beds of LMDs transition from electrically insulating to electrically conducting as well as values reported by Boley for similar LMDs.[37] [X_err is the standard deviation of the particle size distributions.]

The lower thermal conductivity of with the smaller LMDs is also caused in part by the higher overall content of gallium oxide. Similar effects have been noted previously with nano-LMDs.[37] As the size of LMDs changes from $d_{ave} = 12\mu m$ down to $1\mu m$, the surface area of the LMDs increases by seven orders of magnitude (assuming a total LMD volume of 2×10^{-8} m^2). The k of the gallium oxide on the LMDs

will be much less than 13 $Wm^{-1}K^{-1}$ – that of single crystal β-Ga_2O_3.[129] Thus, the large increase in gallium oxide on the increased surface area as the size of LMDs decreases equates to a decrease in constituent thermal conductivity and an increase in thermal interfaces.

Figure 5.9 shows the thermal resistance of the five LMD distributions versus a normalized thickness. The steep slopes for the larger average diameter distributions at the right side of the plot suggest that they are popping under small amounts of compression while the smaller average diameter distributions require more compression before popping, which leads to lowering the thermal resistance.

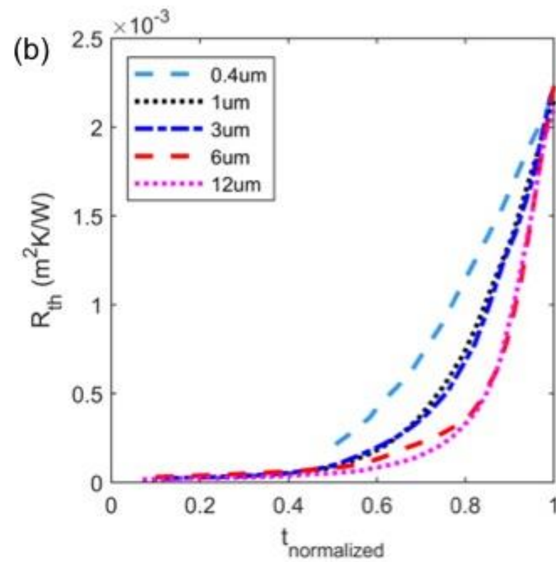

Figure 5.9: Measured thermal resistance of the five LMD distributions versus a normalized thickness of the LMD bed as it is compressed.

Tungsten assisted popping of LMDs

Tungsten may have some uses in controlling the rheological and mechanical properties of liquid gallium based TIMs,[75,125] but in LMD beds it does not provide any thermal benefit, as detailed in Figure 5.10. This data suggests (Figure 5.10a) that a

volume ratio of W to Ga of 1:3 provides the best thermal performance. In applications where high pressures are expected, this ratio of W to Ga would also maintain its high thermal conductivity better than large LMDs by themselves. Comparing Figure 5.10b to Figure 5.10a, it is evident that addition of small W particles produces much lower thermal conductivity than addition of the large W particles. This is due to the increased number of interfaces when using the small W particles and the overall increase in interfacial area. These two parameters increase the interfacial thermal boundary resistance and greatly decrease the thermal conductivity. Comparing Figure 5.10c to Figures 5.10a and 5.10b suggests that the thermal conductivity of these mixtures is much less sensitive to the size of LMDs than when LMDs are measured alone (compare to Figure 5.8a).

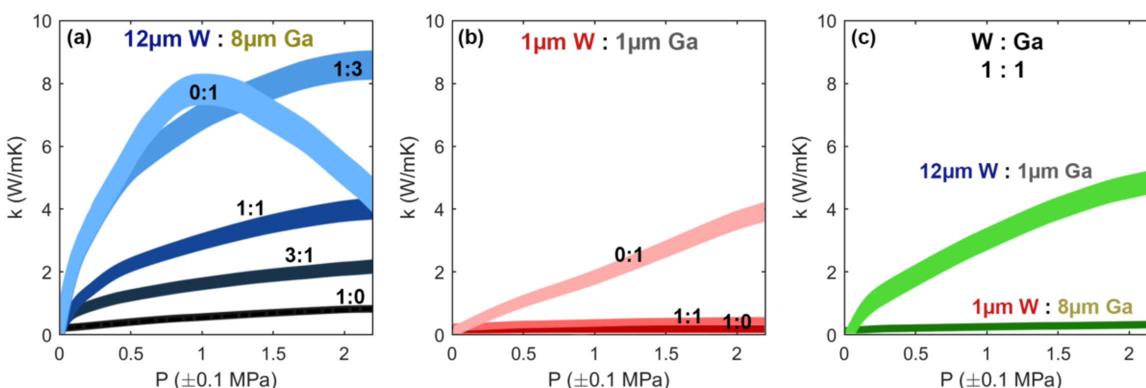

Figure 5.10: Plots of thermal conductivity, k, versus the applied pressure, P, for beds of (a) 12μm W + 8μm Ga, (b) 1μm W + 1μm Ga, and (c) a mixture of sizes at 1:1 volume ratios. The volume ratios are given next to each curve.

Chemical Modification

From previous reports, the thiol-capped LMDs should be softer and have a lower effective surface tension than oxide coated LMDs.[37] Indeed, Figure 5.11

confirms this. The figure shows that the use of dodecanethiol alone to modify the surface of the LMDs produces a lower thermal conductivity than the un-thiolated LMDs. Yet, when etched with HCl, the thiolated LMDs achieve the highest k out of the three options tested. This suggests that the dilute HCl solution does etch and weaken the oxide shell and that the thiol may prevent – or at least delay - oxide regrowth.

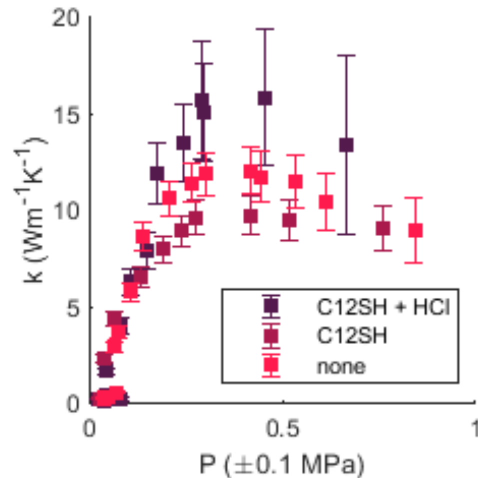

Figure 5.11: Thermal conductivity versus the applied pressure for thiolated LMDs, thiolated LMDs etched by HCl, and un-thiolated LMDs (control).

5.5 Conclusions

In measuring the thermal properties of these beds of LMDs, three main conclusions are apparent from the experiments performed in this chapter:

1) Large LMDs pop under less pressure than small LMDs, thus resulting in higher thermal conductivities at lower pressures.
2) The addition of large W particles can help stabilize the LMDs under high pressure without changing the thermal performance, but the addition of small W particles results in a decrease in thermal conductivity.

3) Exposer to dodecanethiol during LMD fabrication followed by an HCl rinse produces an even higher k than untreated LMDs at an even lower pressure.

In agreement with thin-walled pressure vessel theory, large LMDs require less force to pop than smaller LMDs. Because more of the LMDs are popped under less pressure, the large LMDs produce a higher k than smaller LMDs. The larger LMDs have more flowing metal under less pressure, less overall gallium oxide, and fewer thermal interfaces. The 12μm diameter LMDs achieve k of 8 $Wm^{-1}K^{-1}$ at a pressure of less than 1 MPa while the nano-LMDs only reach 1 $Wm^{-1}K^{-1}$ and at 4 MPa. Furthermore, by fitting the experimental results to some theoretical approximations, I estimate that the ultimate tensile strength of the gallium oxide shells on the LMDs is in the range of 1-2 GPa.

The addition of 12μm W particles to a bed of 8μm diameter LMDs at a 1:3 volume ratio of W to Ga stabilizes the bed and reaches a similar k to large LMDs alone, but at much higher pressures. Small W particles introduce many additional thermal interfaces and decreases the thermal performance of the bed of LMDs.

In agreement with our original hypothesis that LMDs could be weakened by chemical modifications, the LMDs responded as expected to dodecanethiol treatments. An additional thiol layer on top of the oxide layer resulted in a lower k_{max} than untreated LMDs while the thiol layer alone (oxide etched away with HCl) resulted in a higher k_{max}, in excess of 15 $Wm^{-1}K^{-1}$.

CHAPTER 6

CONCLUSIONS AND FUTURE WORK

In the search for the ideal thermal interface material, I advise that one look to magnetically aligned, soft polymer composites. Soft polymer composites provide the mechanical equilibrium required to balance low contact resistance and minimize pump-out. Magnetic alignment can provide significant boosts to the directional thermal conductivity of the composite without undue stiffening of the composites. A volume ratio of magnetically aligned fill of $\phi_{max}/2$ can minimize composite stiffness from the addition of the fill while maximizing the thermal conductivity. Magnetic alignment of spherical particles can double the thermal conductivity of a composite, as compared to the unaligned composites. High aspect ratio fill can benefit even more from magnetic alignment, as much as 3- and 4-fold over the unaligned composites.

The boost in composite thermal conductivity from magnetic alignment comes from an increase in particle-particle contact. The magnetic field drives the fill particles to create a percolation network inside and across the lower thermal conductivity polymer matrix. These percolation networks shift the governing interfacial thermal boundary resistance to the particle-particle interfaces, lowering the overall boundary resistance in the composite and increasing the thermal conductivity. With the particles in good contact with one another from the magnetically-induced percolation, particle-particle contact engineering can then be used to even further reduce the overall boundary resistance and boost the thermal conductivity of the composite.

Particle-particle contacts can be engineered to improve the thermal contact between particles. Hard, rigid fill particles connect to neighboring particles as point

contact with very little interfacial area connecting the two particles. Particle coatings are used to increase the interfacial area and improve the thermal connection between particles. Silver and liquid metal coatings both prove effective at decreasing the particle-particle boundary resistance and increasing the composites thermal conductivity. Magnetically aligned in the polymer matrix, 350nm-thick silver coatings on nickel particles produce a 1.8-fold increase in composite thermal conductivity over the aligned bare-nickel composites. The LM coatings provide similar enhancements, but require higher volumes of LM to do so. This is due to the rapid formation of gallium oxide, which introduces additional thermal boundaries and decreases the benefit of the LM coatings.

Through various experiments exploring the thermal ramifications of rupturing the oxide shell of liquid metal droplets, it is estimated that the Ga2O3 shell on the LMDs has ultimate tensile strength around 1-2 GPa. Large LMDs pop under less pressure than small LMDs. Furthermore, LMDs less than 2μm in diameter require too much force to pop for TIM applications. Adding in large tungsten particles to the bed of LMDs can help stabilize the mixture for applications where higher pressures are expected, while preserving the high thermal conductivity of large ruptured LMDs.

The LMDs can be weakened prior to compression by using thiols in conjunction with hydrochloric acid. The thiols create a layer on top of the oxide shell. A dilute solution of HCl is then used to etch the oxide layer out from under the thiol layer. This results in a 50% increase in thermal conductivity of the compressed bed of LMDs at pressures well below 1 MPa.

Future work will investigate using what was learned in chapter 5 in fabricating a LM-solid metal soft polymer composite that doesn’t suffer the same ill-effects from the LM-oxide as was evident in chapter 4. Additionally, greases made out of the chemically altered LMDs will be fabricated and tested. All these materials need to

undergo long term performance and reliability testing prior to being used as commercial TIMs, but this research shows several methods to increase $k_{TIM,eff}$ that can very positively impact the thermal management of electronics.

REFERENCES

1. Schaller, R. R. Moore's Law: past, present, and future. *IEEE Spectr.* (1997).

2. Ferain, I., Colinge, C. a. & Colinge, J.-P. Multigate transistors as the future of classical metal–oxide–semiconductor field-effect transistors. *Nature* **479,** 310–316 (2011).

3. Semiconductor Industry Association. *2015 International Technology Roadmap for Semiconductors (ITRS)*. (2015).

4. Intel. Intel® Xeon® Processor E5-2695 v4. (2016). Available at: http://ark.intel.com/products/91316/Intel-Xeon-Processor-E5-2695-v4-45M-Cache-2_10-GHz.

5. Moore, A. L. & Shi, L. Emerging challenges and materials for thermal management of electronics. *Mater. Today* **17,** 163–174 (2014).

6. Prasher, R. Thermal interface materials: historical perspective, status, and future directions. in *Proceedings of the IEEE* **94,** 1571–86 (IEEE, 2006).

7. McNamara, A. J., Joshi, Y. & Zhang, Z. M. Characterization of nanostructured thermal interface materials--a review. *Int. J. Therm. Sci.* **62,** 2–11 (2012).

8. Ralphs, M. I. Investigating the Effect of Carbon Nanotube Functionalization in Polydimethylsiloxane Composite through use of a Stepped Bar Apparatus. (Utah State University, 2016).

9. *2005 International Technology Roadmap for Semiconductors (ITRS)*. (2005).

10. Yang, Y. Physical Properties of Polymers Handbook. in *Zeitschrift für Physikalische Chemie* 155–163 (2007). doi:10.1007/978-0-387-69002-5

11. Mark, J. E. *Polymer Data Handbook*. (New York, Oxford University Press, 2009).

12. Bogatin, E. Chip Packaging: Thermal Requirements and Constraints. in *Roadmaps of Packaging Technology* (eds. Potter, D. & Peters, L.) 1–32 (Integrated Circuit Engineering, 1997).

13. Gwinn, J. P. & Webb, R. L. Performance and testing of thermal interface materials. **34,** 215–222 (2003).

14. Warzoha, R. J. & Donovan, B. F. High resolution steady-state measurements of thermal contact resistance across thermal interface material junctions. *Rev. Sci. Instrum.* **88,** (2017).

15. Roy, C. K. *et al.* Investigation into the application of low melting temperature

alloys as wet thermal interface materials. *Int. J. Heat Mass Transf.* **85,** 996–1002 (2015).

16. Prasher, R. S. & Chiu, C.-P. Thermal Interface Materials. in *Materials for Advanced Packaging* 511–535 (2017). doi:10.1007/978-3-319-45098-8

17. Pietrak, K. & Wisniewski, T. S. A review of models for effective thermal conductivity of composite materials. *Open Access J. J. Power Technol.* **95,** 14–24 (2015).

18. Tavangar, R., Molina, J. M. & Weber, L. Assessing predictive schemes for thermal conductivity against diamond-reinforced silver matrix composites at intermediate phase contrast. *Scr. Mater.* **56,** 357–360 (2007).

19. DuPont. DuPont Kapton HN Polyimide film. Available at: https://www.americandurafilm.com/data-sheets/kapton-hn.pdf. (Accessed: 12th December 2017)

20. Dupont. DuPont High Performance Materials Kapton MT Thermally Conductive Substrate polyimide film. Available at: https://www.americandurafilm.com/data-sheets/kapton-mt.pdf. (Accessed: 12th December 2017)

21. Zhang, R. *et al.* Thermal resistance analysis of Sn-Bi solder paste used as thermal interface material for power electronics applications. *J. Electron. Packag.* **136,** 11012 (2014).

22. Chung, D. D. . Materials for thermal conduction. *Appl. Therm. Eng.* **21,** 1593–1605 (2001).

23. Blazej, D. Thermal interface materials. *Electron. Cool.* **9,** 14–21 (2003).

24. Bar-Cohen, A., Matin, K. & Narumanchi, S. Nanothermal Interface Materials: Technology Review and Recent Results. *J. Electron. Packag.* **137,** 040803 (2015).

25. Gao, Y., Wang, X., Liu, J. & Fang, Q. Investigation on the optimized binary and ternary gallium alloy as thermal interface materials. *J. Electron. Packag.* **139,** 1–8 (2016).

26. Ma, K. & Liu, J. Liquid metal cooling in thermal management of computer chips. *Front. Energy Power Eng. China* **1,** 384–402 (2007).

27. Li, G., Ji, Y., Wu, M. & Ma, H. Highly Conductive thermal paste of liquid matal alloy dispersed with copper particles. in *Proceedings of the ASME 2016 Heat Transfer Summer Conference* (American Society of Mechanical Engineers, 2016).

28. Gao, Y. & Liu, J. Gallium-based thermal interface material with high compliance and wettability. *Appl. Phys. A* **107,** 701–708 (2012).

29. Lin, Y. *et al.* Handwritten, Soft Circuit Boards and Antennas Using Liquid Metal Nanoparticles. *Small* **11,** 6397–6403 (2015).

30. Mei, S., Gao, Y., Deng, Z. & Liu, J. Thermally Conductive and Highly Electrically Resistive Grease Through Homogeneously Dispersing Liquid Metal Droplets Inside Methyl Silicone Oil. *J. Electron. Packag.* **136,** 011009 (2014).

31. Ren, L. *et al.* Nanodroplets for Stretchable Superconducting Circuits. *Adv. Funct. Mater.* 1–8 (2016). doi:10.1002/adfm.201603427

32. Lyon, R. N. Liquid Metals Handbook, The Committee on the Basic Properties of Liquid Metals. *Off. Nav. Res. Dep. Navy* (1952).

33. Rajagopalan, M., Bhatia, M. A., Tschopp, M. A., Srolovitz, D. J. & Solanki, K. N. Atomic-scale analysis of liquid-gallium embrittlement of aluminum grain boundaries. *Acta Mater.* **73,** 312–325 (2014).

34. Deng, Y. G. & Liu, J. Corrosion development between liquid gallium and four typical metal substrates used in chip cooling device. *Appl. Phys. A Mater. Sci. Process.* **95,** 907–915 (2009).

35. Ndieguene, A., Albert, P., Fortin, C., Oberson, V. & Sylvestre, J. Eternal Packages: Liquid Metal Flip Chip Devices. *2016 IEEE 66th Electron. Components Technol. Conf.* 580–587 (2016). doi:10.1109/ECTC.2016.29

36. Jeong, S. H. *et al.* Mechanically Stretchable and Electrically Insulating Thermal Elastomer Composite by Liquid Alloy Droplet Embedment. *Sci. Rep.* **5,** 18257 (2015).

37. Boley, J. W., White, E. L. & Kramer, R. K. Mechanically sintered gallium-indium nanoparticles. *Adv. Mater.* **27,** 2355–2360 (2015).

38. Boley, J. W., White, E. L., Chiu, G. T. C. & Kramer, R. K. Direct writing of gallium-indium alloy for stretchable electronics. *Adv. Funct. Mater.* **24,** 3501–3507 (2014).

39. Zhang, W. *et al.* Liquid metal/metal oxide frameworks with incorporated Ga2O3 for photocatalysis. *ACS Appl. Mater. Interfaces* **7,** 1943–1948 (2015).

40. Yamaguchi, A., Mashima, Y. & Iyoda, T. Reversible size control of liquid-metal nanoparticles under ultrasonication. *Angew. Chemie - Int. Ed.* **54,** 12809–12813 (2015).

41. Markvicka, E. J., Bartlett, M. D., Huang, X. & Majidi, C. An autonomously electrically self-healing liquid metal-elastomer composite for robust soft-matter robotics and electronics. *Nat. Mater.* **17,** (2018).

42. Bartlett, M. D. *et al.* High thermal conductivity in soft elastomers with elongated liquid metal inclusions. *Proc. Natl. Acad. Sci.* **114,** 3–8 (2017).

43. Fassler, A. L. Application of Liquid-Metal GaIn Alloys to Soft- matter Capacitance and Related Stretchable Electronics. (2016).

44. Fassler, A. & Majidi, C. Liquid-Phase Metal Inclusions for a Conductive Polymer Composite. *Adv. Mater.* **27,** 1928–1932 (2015).

45. Bartlett, M. D. *et al.* Stretchable, High-k Dielectric Elastomers through Liquid-Metal Inclusions. *Adv. Mater.* **28,** 3726–3731 (2016).

46. Clarson, S. J. & Semlyen, A. *Siloxane Polymers*. (1993).

47. ABCR. *Research Chemicals and Metals Catalogue*. (1994).

48. Liu, M., Sun, J. & Chen, Q. Influences of heating temperature on mechanical properties of polydimethylsiloxane. *Sensors Actuators, A Phys.* **151,** 42–45 (2009).

49. *Dow Corning 2005 Product Information sheet of Sylgard 184*.

50. Schneider, F., Fellner, T., Wilde, J. & Wallrabe, U. Mechanical properties of silicones for MEMS. *J. Micromechanics Microengineering* **18,** 065008 (2008).

51. Corning, D. Electronics Sylgard ® 184 Silicone Elastomer. *Prod. Datasheet* 1–3 (2013). doi:10.1017/CBO9781107415324.004

52. Diani, J., Fayolle, B. & Gilormini, P. A review on the Mullins effect. *Eur. Polym. J.* **45,** 601–612 (2009).

53. Jeong, S. H., Zhang, S., Hjort, K., Hilborn, J. & Wu, Z. Stretchable Electronic Devices: PDMS-Based Elastomer Tuned Soft, Stretchable, and Sticky for Epidermal Electronics (Adv. Mater. 28/2016). *Adv. Mater.* **28,** 5765 (2016).

54. Wang, Z., Volinsky, A. A. & Gallant, N. D. Crosslinking effect on polydimethylsiloxane elastic modulus measured by custom-built compression instrument. *J. Appl. Polym. Sci.* **41050,** 1–4 (2014).

55. Maxwell, J. C. *A Treatise on Electricity and Magnetism, Vol.1. Clarendon Press (Oxford)* **I,** (Clarendon Press, 1881).

56. Rayleigh, Lord. On the influence of obstacles arranged in rectangular order upon the properties of a medium. *London, Edinburgh, Dublin Philos. Mag. J. Sci.* **34,** 481–502 (1892).

57. Hasselman, D. P. H. & Johnson, L. F. Effective Thermal Conductivity of Composites with Interfacial Thermal Barrier Resistance. *Compos. Mater.* **21,** 508–215 (1987).

58. Nan, C.-W., Birringer, R., Clark, D. R. & Gleiter, H. Effective thermal conductivity of paticulate composites with interfacial thermal resistance. *J. Appl. Physics1* **81,** 6692–6699 (997).

59. Bruggeman, D. A. G. The prediction of the thermal conductivity of heterogenous mixtures. *Ann Phys* **24,** 636–664 (1935).

60. Landauer, R. The Electrical Resistance of Binary Metallic Mixtures. *J. Appl. Phys.* **23,** 779–784 (1952).

61. Kanuparthi, S., Subbarayan, G., Siegmund, T. & Sammakia, B. An Efficient Network Model for Determining the Effective Thermal Conductivity of Particulate Thermal Interface Materials. *IEEE Trans. Components Packag. Technol.* **31,** 611–621 (2008).

62. Nielsen, L. E. The Thermal and Electrical Conductivity of Two-Phase Systems. *Ind. Eng. Chem. Fundam.* **13,** 17–20 (1974).

63. Devpura, a., Phelan, P. E. & Prasher, R. S. Percolation theory applied to the analysis of thermal interface materials in flip-chip technology. *Proc. of ITHERM* **1,** 21–28 (2000).

64. Prasher, R. S. & Phelan, P. E. Microscopic and macroscopic thermal contact resistances of pressed mechanical contacts. *J. Appl. Phys.* **100,** (2006).

65. Rai, A. & Moore, A. L. Enhanced thermal conduction and influence of interfacial resistance within flexible high aspect ratio copper nanowire/polymer composites. *Compos. Sci. Technol.* **144,** 70–78 (2017).

66. Regan, M. J. *et al.* X-ray study of the oxidation of liquid-gallium surfaces. *Phys. Rev. B* **55,** 10786–10790 (1997).

67. Scharmann, F. *et al.* Viscosity effect on GaInSn studied by XPS. *Surf. Interface Anal.* **36,** 981–985 (2004).

68. Dickey, M. D. Emerging applications of liquid metals featuring surface oxides. *ACS Appl. Mater. Interfaces* **6,** 18369–18379 (2014).

69. Zhang, W. *et al.* Liquid metal/metal oxide frameworks. *Adv. Funct. Mater.* **24,** 3799–3807 (2014).

70. Tevis, I. D., Newcomb, L. B. & Thuo, M. Synthesis of liquid core-shell particles and solid patchy multicomponent particles by shearing liquids into complex particles (SLICE). *Langmuir* **30,** 14308–14313 (2014).

71. Tang, S. Y. *et al.* Liquid-Metal Microdroplets Formed Dynamically with Electrical Control of Size and Rate. *Adv. Mater.* **28,** 604–609 (2016).

72. Hutter, T., Bauer, W. A. C., Elliott, S. R. & Huck, W. T. S. SI: Formation of Spherical and Non-Spherical Eutectic Gallium-Indium Liquid-Metal Microdroplets in Microfluidic Channels at Room Temperature: Supporting Information. *Adv. Funct. Mater.* **1,** 1–5 (2012).

73. Kim, D. *et al.* Recovery of nonwetting characteristics by surface modification of gallium-based liquid metal droplets using hydrochloric acid vapor. *ACS Appl. Mater. Interfaces* **5,** 179–185 (2013).

74. Zhou, Y. *et al.* Formation, etching and electrical characterization of a thermally grown gallium oxide on the Ga-face of a bulk GaN substrate. *Solid. State. Electron.* **52,** 756–764 (2008).

75. Tang, J. *et al.* Gallium-Based Liquid Metal Amalgams: Transitional-State Metallic Mixtures (TransM2ixes) with Enhanced and Tunable Electrical, Thermal, and Mechanical Properties. *ACS Appl. Mater. Interfaces* (2017). doi:10.1021/acsami.7b10256

76. Thompson, D. R., Rao, S. R. & Cola, B. a. A Stepped-Bar Apparatus for Thermal Resistance Measurements [1]. *J. Electron. Packag.* **135,** 041002 (2013).

77. Ralphs, M. I., Smith, B. L. & Roberts, N. A. Technique for direct measurement of thermal conductivity of elastomers and a detailed uncertainty analysis. *Meas. Sci. Technol.* **27,** 115014 (2016).

78. ASTM. Standard Test Method for Thermal Transmission Properties of Thermally Conductive Electrically Insulating Materials. *ASTM Int.* **D5470,** (2006).

79. Thompson, D. R., Rao, S. R. & Cola, B. A. A stepped-bar apparatus for thermal resistance measurements. *J. Electron. Packag.* **135,** 41002 (2013).

80. Ralphs, M., Scheitlin, C., Wang, R. Y. & Rykaczewski, K. Buckling of Magnetically-Formed Filler Fiber Columns under Compression Increases Thermal Resistance of Soft Polymer Composites. *J. Heat Transfer* **141,** 012001 (2019).

81. Ralphs, M., Kong, W., Wang, R. Y. & Rykaczewski, K. Thermal Conductivity Enhancement of Soft Polymer Composites through Magnetically-Induced Percolation and Particle-Particle Contact Engineering. *Adv. Mater. Interfaces* (Accepted Jan 2019)

82. Mamunya, Y. P., Davydenko, V. V., Pissis, P. & Lebedev, E. V. Electrical and thermal conductivity of polymers filled with metal powders. *Eur. Polym. J.* **38,** 1887–1897 (2002).

83. Lebovka, N., Lisunova, M., Mamunya, Y. P. & Vygornitskii, N. Scaling in percolation behaviour in conductive-insulating composites with particles of different size. *J. Phys. D. Appl. Phys.* **39,** 2264–2271 (2006).

84. Anderson, C. H., Balberg, I., Alexander, S. & Wagner, N. Excluded Volume and its relation to the onset of percolation. *Phys. Rev. B* **30,** 3933–3943 (1984).

85. Balberg, I., Binenbaum, N. & Wagner, N. Percolation thresholds in the three-dimensional sticks system. *Phys. Rev. Lett.* **52,** 1465–1468 (1984).

86. Consiglio, R., Baker, D. R., Paul, G. & Stanley, H. E. Continuum percolation thresholds for mixtures of spheres of different sizes. *Phys. A Stat. Mech. its Appl.* **319,** 49–55 (2003).

87. Douglas, J. F. & Thorpe, F. Geometrical percolation. **52,** 819–828 (1995).

88. Galam, S. & Mauger, A. Universal formulas for percolation thresholds. *Phys. Rev. E* **53,** 2177–2181 (1996).

89. Tutika, R., Zhou, S. H., Napolitano, R. E. & Bartlett, M. D. Mechanical and Functional Tradeoffs in Multiphase Liquid Metal, Solid Particle Soft Composites. *Adv. Funct. Mater.* 1804336 (2018). doi:10.1002/adfm.201804336

90. Xie, X. L., Mai, Y. W. & Zhou, X. P. Dispersion and alignment of carbon nanotubes in polymer matrix: A review. *Mater. Sci. Eng. R Reports* **49,** 89–112 (2005).

91. Jopek, H. & Strek, T. Optimization of the Effective Thermal Conductivity of a Composite. in *Convection and Conduction Heat Transfer* 197–213 (2009).

92. Feng, C. P. *et al.* A Facile Route to Fabricate Highly Anisotropic Thermally Conductive Elastomeric POE/NG Composites for Thermal Management. *Adv. Mater. Interfaces* **1700946,** 1–7 (2017).

93. Han, Z. & Fina, A. Thermal conductivity of carbon nanotubes and their polymer nanocomposites: A review. *Prog. Polym. Sci.* **36,** 914–944 (2011).

94. Renteria, J. *et al.* Magnetically-functionalized self-aligning graphene fillers for high-efficiency thermal management applications. *Mater. Des.* **88,** 214–221 (2015).

95. Tian, X., Itkis, M. E., Bekyarova, E. B. & Haddon, R. C. Anisotropic Thermal and Electrical Properties of Thin Thermal Interface Layers of Graphite Nanoplatelet-Based Composites. *Sci. Rep.* **3,** 1710 (2013).

96. Schmidt, G. & Malwitz, M. M. Properties of Polymer-Nanoparticle Composites. *Curr. Opin. Colloid Interface Sci.* **8,** 103–108 (2003).

97. Hill, R. F. & Supancic, P. H. Thermal Conductivity of Platelet-Filled Polymer Composites. *J. Am. Ceram. Soc.* **85,** 851–857 (2002).

98. Jin, S. *et al.* New, Z-direction anisotropically conductive composites. *J. Appl. Phys.* **64,** 6008–6010 (1988).

99. Jin, S., Tiefel, T. H. & Wolfe, R. Directionally-Conductive, Optically-Transparent Composites by Magnetic Alignment. *IEEE Trans. Magn.* **28,** 2211–2213 (1992).

100. Breval, E., Klimkiewicz, M., Shi, Y. T., Arakaki, D. & Dougherty, J. P. Magnetic alignment of particles in composite films. *J. Mater. Sci.* **38,** 1347–1351 (2003).

101. Ramkumar, S. & Srihari, K. A Novel Anisotropic Conductive Adhesive for Lead-Free Surface Mount Electronics Packaging. *J. Electron. Packag.* **129,** 149 (2007).

102. Lu, T., Wissman, J., Ruthika & Majidi, C. Soft anisotropic conductors as electric vias for Ga-based liquid metal circuits. *ACS Appl. Mater. Interfaces* **7,** 26923–26929 (2015).

103. Martin, J. E. & Gulley, G. Field-structured composites for efficient, directed heat transfer. *J. Appl. Phys.* **106,** 084301 (2009).

104. Su, J., Liu, X., Charmchi, M. & Sun, H. Experimental and numerical study of anisotropic thermal conductivity of magnetically aligned PDMS/Ni particle composites. *Int. J. Heat Mass Transf.* **97,** 645–652 (2016).

105. Solis, K. J. & Martin, J. E. Field-structured magnetic platelets as a route to improved thermal interface materials. *J. Appl. Phys.* **111,** 073507 (2012).

106. Yuan, C. *et al.* Thermal Conductivity of Polymer-Based Composites with Magnetic Aligned Hexagonal Boron Nitride Platelets. *ACS Appl. Mater. Interfaces* **7,** 13000–13006 (2015).

107. Martin, J. E. & Snezhko, A. Driving self-assembly and emergent dynamics in colloidal suspensions by time-dependent magnetic fields. *Reports Prog. Phys.* **76,** 126601 (2013).

108. Yan, H., Tang, Y., Long, W. & Li, Y. Enhanced thermal conductivity in polymer composites with aligned graphene nanosheets. *J. Mater. Sci.* **49,** 5256–5264 (2014).

109. Martin, J. E. Field-structured polymer composites. *Macromol. Symp.* **329,** 162–172 (2013).

110. Kimura, T. *et al.* Polymer Composites of Carbon Nanotubes Aligned by a Magnetic Field. *Advanded Mater.* **14,** 1380–1383 (2002).

111. Toll, S. Packing mechanics of fiber reinforcements. *Polym. Eng. Sci.* **38,** 1337–1350 (1998).

112. Ralphs, M. I. *et al.* In Situ Alloying of Thermally Conductive Polymer Composites by Combining Liquid and Solid Metal Microadditives. *ACS Appl. Mater. Interfaces* **10,** 2083–2092 (2018).

113. Buttner, F. H., Funk, E. R. & Udin, H. Adsorption of oxygen on silver. *J. Phys. Chem.* **56,** 657–660 (1952).

114. Moore, W. M. & Codella, P. J. Oxidation of silver films by atomic oxygen. *J. Phys. Chem.* **92,** 4421–4426 (1988).

115. Balachander, N. *et al.* Nanowire-filled polymer composites with ultrahigh thermal conductivity. *Appl. Phys. Lett.* **102,** 093117 (2013).

116. Pashayi, K. *et al.* High Thermal Conductivity epoxy-silver composites based on self-constructing nanostructured metallic networks. *J. Appl. Phys.* **111,** 104310 (2012).

117. Yu, H., Li, L. & Zhang, Y. Silver nanoparticle-based thermal interface materials with ultra-low thermal resistance for power electronics applications. *Scr. Mater.* **66,** 931–934 (2012).

118. Seshadri, I., Esquenazi, G. L., Cardinal, T., Borca-Tasciuc, T. & Ramanath, G. Microwave synthesis of branched silver nanowires and their use as fillers for high thermal conductivity polymer composites. *Nanotechnology* **27,** 175601 (2016).

119. Seshadri, I., Esquenazi, G. L., Borca-Tasciuc, T., Keblinski, P. & Ramanath, G. Multifold Increases in Thermal Conductivity of Polymer Nanocomposites through Microwave Welding of Metal Nanowire Fillers. *Adv. Mater. Interfaces* **2,** 1–6 (2015).

120. Hwang, B., Shin, H. A. S., Kim, T., Joo, Y. C. & Han, S. M. Highly reliable Ag nanowire flexible transparent electrode with mechanically welded junctions. *Small* **10,** 3397–3404 (2014).

121. Callister, J. W. D. *Material Science and Engineering An Introduction*. (John Wiley & Sons, Inc, 2007).

122. Hodes, M., Zhang, R., Lam, L. S., Wilcoxon, R. & Lower, N. On the potential of galinstan-based minichannel and minigap cooling. *IEEE Trans. Components, Packag. Manuf. Technol.* **4,** 46–56 (2014).

123. Park, C. W. *et al.* Photolithography-Based Patterning of Liquid Metal Interconnects for Monolithically Integrated Stretchable Circuits. *ACS Appl. Mater. Interfaces* **8,** 15459–15465 (2016).

124. Kazem, N., Hellebrekers, T. & Majidi, C. Soft Multifunctional Composites and Emulsions with Liquid Metals. *Adv. Mater.* **1605985,** 1605985 (2017).

125. Daalkhaijav, U., Yirmibesoglu, O. D., Walker, S. & Mengüç, Y. Rheological Modification of Liquid Metal for Additive Manufacturing of Stretchable Electronics. *Adv. Mater. Technol.* **3,** 1700351 (2018).

126. Ren, L. *et al.* A Liquid-Metal-Based Magnetoactive Slurry for Stimuli-Responsive Mechanically Adaptive Electrodes. *Adv. Mater.* **1802595,** 1802595 (2018).

127. Doudrick, K. *et al.* Different shades of oxide: From nanoscale wetting mechanisms to contact printing of gallium-based liquid metals. *Langmuir* **30,** 6867–6877 (2014).

128. Liu, S. *et al.* Can liquid metal flow in microchannels made of its own oxide skin? *Microfluid. Nanofluidics* **20,** 1–6 (2016).

129. Guo, Z. Anisotropic thermal conductivity in single crystal β-gallium oxide. **111909,** 1–6 (2015).

130. Yu, S. & Kaviany, M. Electrical, thermal, and species transport properties of liquid eutectic Ga-In and Ga-In-Sn from first principles. *J. Chem. Phys.* **140,** (2014).

131. Grashchenko, A. S. *et al.* Study of the Anisotropic Elastoplastic Properties of β - Ga 2 O 3 Films Synthesized on SiC / Si Substrates. *Phys. Solid State* **60,** 852–857 (2018).

132. Mercadé-Prieto, R. *et al.* Determination of the Failure Stresses for Fluid-filled Microcapsules that Rupture Near the Elastic Regime. *Exp. Mech.* **52,** 1435–1445 (2012).

133. Nezamabadi, S., Radjai, F., Averseng, J. & Delenne, J. Y. Implicit frictional-contact model for soft particle systems. *J. Mech. Phys. Solids* **83,** 72–87 (2015).

134. Farrell, Z. J. & Tabor, C. E. Control of Gallium Oxide Growth on Liquid Metal Eutectic Gallium/Indium Nanoparticles via Thiolation. *Langmuir* **34,** 234–240 (2018).

135. Koh, A., Mrozek, R. & Slipher, G. Characterization and Manipulation of Interfacial Activity for Aqueous Galinstan Dispersions. *Adv. Mater. Interfaces* **1701240,** 1–9 (2018).

136. Cumby, B. L., Mast, D. B., Tabor, C. E., Dickey, M. D. & Heikenfeld, J. Robust Pressure-Actuated Liquid Metal Devices Showing Reconfigurable Electromagnetic Effects at GHz Frequencies. *IEEE Trans. Microw. Theory Tech.* **63,** 3122–3130 (2015).

137. Holcomb, S. *et al.* Oxide-Free Actuation of Gallium Liquid Metal Alloys Enabled by Novel Acidified Siloxane Oils. *Langmuir* **32,** 12656–12663 (2016).

138. Diebold, A. V. *et al.* Electrowetting-actuated liquid metal for RF applications. *J. Micromechanics Microengineering* **27,** (2017).

139. Khan, M. R., Eaker, C. B., Bowden, E. F. & Dickey, M. D. Giant and switchable surface activity of liquid metal via surface oxidation. *Proc. Natl. Acad. Sci.* **111,** 14047–14051 (2014).

140. Tevis, I. D., Newcomb, L. B. & Thuo, M. Synthesis of liquid core-shell particles and solid patchy multicomponent particles by shearing liquids into complex particles (SLICE). *Langmuir* **30,** 14308–14313 (2014).

141. Ilyas, N., Cook, A. & Tabor, C. E. Designing Liquid Metal Interfaces to Enable Next Generation Flexible and Reconfigurable Electronics. *Adv. Mater. Interfaces* **4,** 6–11 (2017).

142. Farrell, Z. J., Reger, N., Anderson, I., Gawalt, E. & Tabor, C. Route to Universally Tailorable Room-Temperature Liquid Metal Colloids via Phosphonic Acid Functionalization. *J. Phys. Chem. C* **122,** 26393–26400 (2018).

143. Gelest. *Silane Coupling Agents*. *Gelest* (2014). doi:10.1016/B978-0-12-382239-0.00013-3

144. Thelen, J., Dickey, M. D. & Ward, T. A study of the production and reversible stability of EGaIn liquid metal microspheres using flow focusing. *Lab Chip* **12,** 3961–3967 (2012).

145. Hayashi, Y., Saneie, N., Yip, G., Kim, Y. J. & Kim, J. H. Metallic nanoemulsion with galinstan for high heat-flux thermal management. *Int. J. Heat Mass Transf.* **101,** 1204–1216 (2016).

146. Cicco, A. Di, Fusari, S. & Stizza, S. Phase transitions and undercooling in confined gallium. *Philos. Mag. B* **79,** 2113–2120 (1999).

147. Mercadé-Prieto, R. *et al.* Determination of the elastic properties of single microcapsules using micromanipulation and finite element modeling. *Chem. Eng. Sci.* **66,** 2042–2049 (2011).

148. Dickey, M. D. *et al.* Eutectic gallium-indium (EGaIn): A liquid metal alloy for the formation of stable structures in microchannels at room temperature. *Adv. Funct. Mater.* **18,** 1097–1104 (2008).

149. Regan, M. J. *et al.* X-ray reflectivity studies of liquid metal and alloy surfaces. *Phys. Rev. B* **55,** 15874–15884 (1997).

150. Dumke, M. F., Tombrello, T. A., Weller, R. A., Housley, R. M. & Cirlin, E. H. Sputtering of the gallium-indium eutectic alloy in the liquid phase. *Surf. Sci.* **124,** 407–422 (1983).

APPENDIX A

HEAT SINK SURFACE PROFILES

The roughness of three commercial heat sink surfaces were examined with optical profilometry to determine the surface roughness that a TIM 2 would need to address. Figures A1, A2, and A3 show the profiles and images of the Enzotech CNB-SI Forged copper 1100 (pin fins, mirror finish, $20), the Cooler Master Hyper 212 EVO (4 direct contact heat pipes, machine finish, $30), and the Cryorig H7 tower cooler (3 pure copper, indirect contact heat pipes, machine finish, $35), respectively.

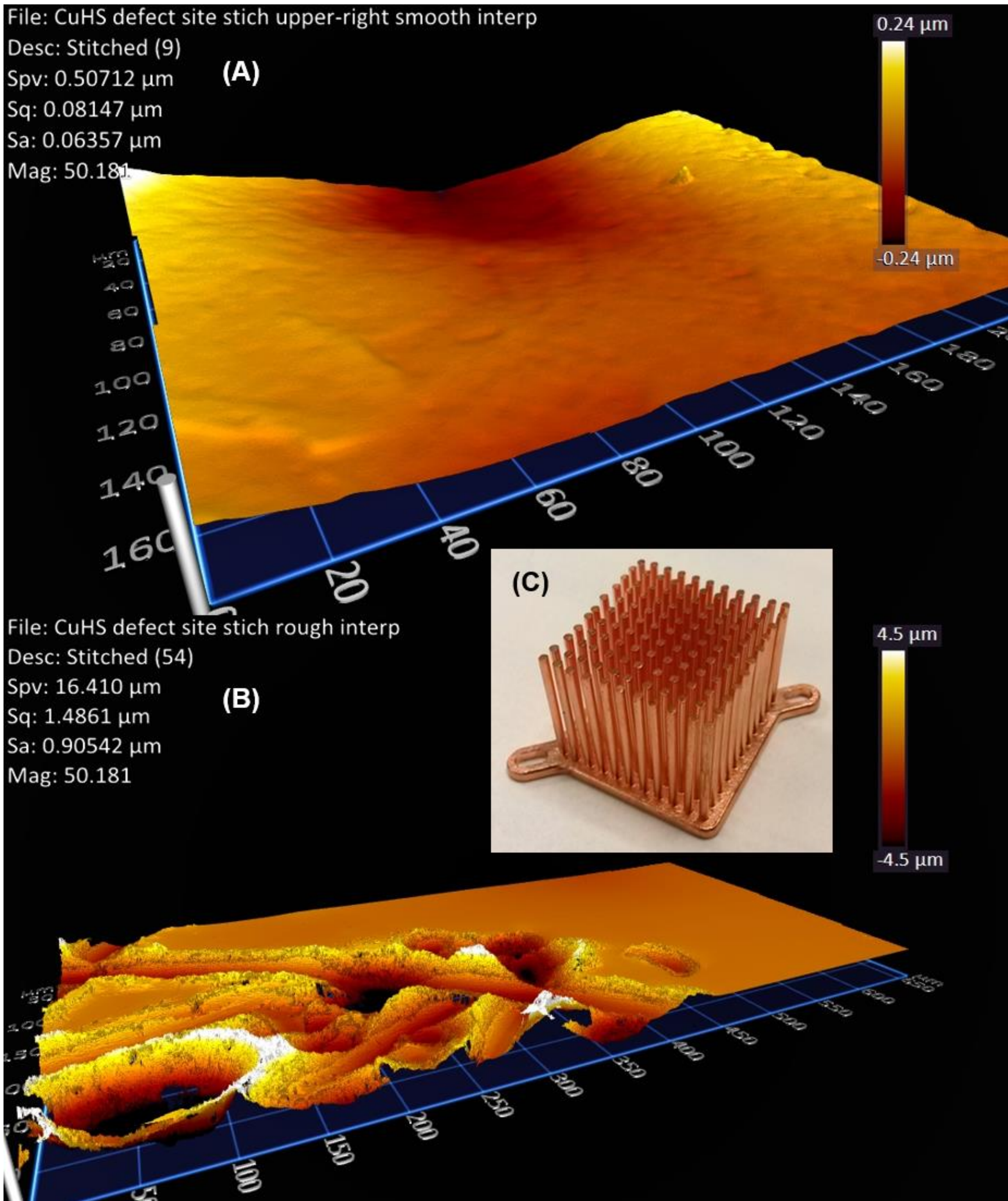

Figure A1: Surface profile of (A) the mirror finish and (B) a defect of the Enzotech CNB-SI forged copper heat sink along with (C) a photo.

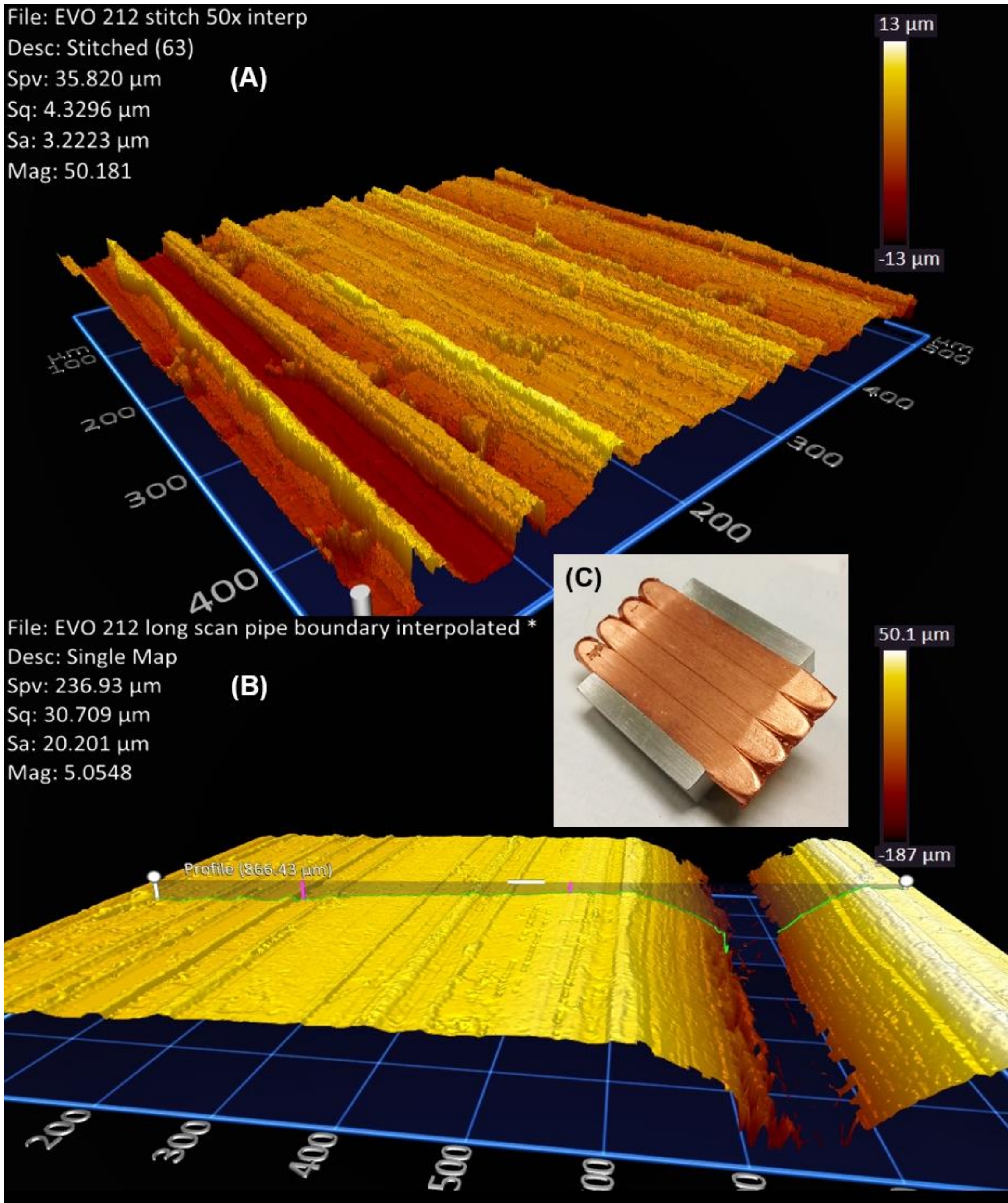

Figure A2: Surface profile of (A) the machined finish and (B) the gap between pipes of the Cooler Master Hyper 212 EVO heat sink along with (C) a photo.

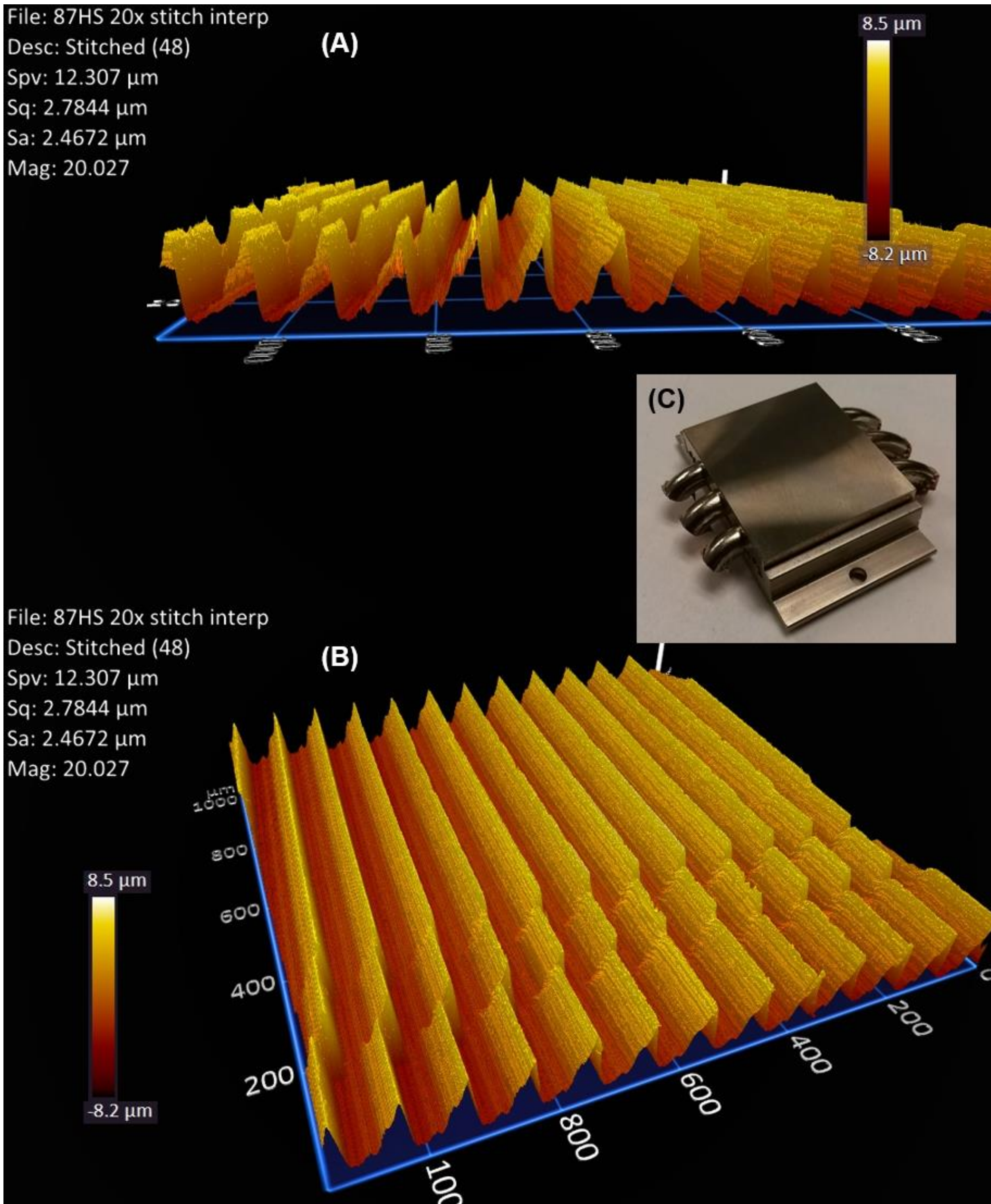

Figure A3: Surface profile of the machine finish (A,B) on the Cryorig H7 tower cooler heat sink along with (C) a photo.

APPENDIX B

APPROVALS TO USE PREVIOUSLY PUBLISHED WORKS

Approval has been given by JHT (Mary O'Brien, Nov 21, 2018) and all the co-authors to re-produce and use the following published work in this dissertation:

> Ralphs, M., Scheitlin, C., Wang, R. Y. & Rykaczewski, K. Buckling of Magnetically-Formed Filler Fiber Columns under Compression Increases Thermal Resistance of Soft Polymer Composites. *J. Heat Transfer* **141,** 012001 (2019).

Approval has been given by AMI ACS (Jamie Ferraioli for Prof. Vladimir Tsukruk, Nov 26, 2018) and all the co-authors to re-produce and use the following published work in this dissertation:

> Ralphs, M. I. *et al.* In Situ Alloying of Thermally Conductive Polymer Composites by Combining Liquid and Solid Metal Microadditives. *ACS Appl. Mater. Interfaces* **10,** 2083–2092 (2018).

Approval given by Wiley-VCH Verlag GmbH & Co. KGaA and Advanced Material Interfaces (Bettina Loycke, Nov 22, 2018) and all co-authors to re-produce and use the following submitted manuscript in this dissertation:

> Ralphs, M., Kong, W., Wang, R. Y. & Rykaczewski, K. Thermal Conductivity Enhancement of Soft Polymer Composites through Magnetically-Induced Percolation and Particle-Particle Contact Engineering. *Adv. Mater. Interfaces* (Submitted Nov 2018)

APPENDIX C

BUCKLING OF MAGNETICALLY-FORMED FILLER FIBER COLUMNS UNDER COMPRESSION INCREASES THERMAL RESISTANCE OF SOFT POLYMER COMPOSITES

Matthew Ralphs
School for Engineering of Matter,
Transport and Energy,
Arizona State University,
Tempe, AZ 85287

Chandler Scheitlin
School for Engineering of Matter,
Transport and Energy,
Arizona State University,
Tempe, AZ 85287

Robert Y. Wang[1]
School for Engineering of Matter,
Transport and Energy,
Arizona State University,
Tempe, AZ 85287
e-mail: rywang@asu.edu

Konrad Rykaczewski[1]
School for Engineering of Matter,
Transport and Energy,
Arizona State University,
Tempe, AZ 85287
e-mail: konradr@asu.edu

Buckling of Magnetically Formed Filler Fiber Columns Under Compression Increases Thermal Resistance of Soft Polymer Composites

Thermally conductive soft composites are in high demand, and aligning the fill material is a potential method of enhancing their thermal performance. In particular, magnetic alignment of nickel particles has previously been demonstrated as an easy and effective way to improve directional thermal conductivity of such composites. However, the effect of compression on the thermal performance of these materials has not yet been investigated. This work investigates the thermal performance of magnetically aligned nickel fibers in a soft polymer matrix under compression. The fibers orient themselves in the direction of the applied magnetic field and align into columns, resulting in a 3× increase in directional thermal conductivity over unaligned composites at a volume fraction of 0.15. Nevertheless, these aligned fiber columns buckle under strain resulting in an increase in the composite thermal resistance. These results highlight potential pitfalls of magnetic filler alignment when designing soft composites for applications where strain is expected such as thermal management of electronics. [DOI: 10.1115/1.4041539]

Introduction

By filling in air gaps, thermal interface materials (TIMs) reduce thermal contact resistance between mating electronic components in integrated circuits. These materials are integral to the operation of cell phones, laptops, servers, and wherever computer chips produce heat. Furthermore, improving the thermal performance of TIMs enables faster speeds and longer lifespans in these systems. Conversely, poor thermal management can lead to accelerated aging and rapid degradation [1–4].

Composites consisting of a soft polymer matrix with high thermal conductivity filler particles are commonly used as TIM "pads." These soft polymer composites have two primary advantages: (1) the low Young's modulus allows the TIM to conform to the geometrical imperfections of the two mating surfaces and (2) the polymer pads do not suffer from pump out issues like most thermal greases [2]. However, the soft polymer matrices have a low thermal conductivity of 0.1–0.4 W m^{-1} K^{-1} [5,6] that can only be moderately enhanced to around 1.5–3 W m^{-1} K^{-1} by solely dispersing traditional high thermal conductivity filler particles [7]. Consequently, much effort has been dedicated to developing novel fillers and their dispersion methods that increase the thermal conductivity of soft polymer composites to the ranges needed for current high performance applications [3,4,8,9].

Thermal conductivity of polymer composites is a function of fill thermal conductivity, fill volume ratio, fill aspect ratio, matrix thermal conductivity, interaction between fill and matrix, fill alignment, and dispersion [7]. In general, an increase in the value of the first four listed parameters will result in an increase in the composite thermal conductivity, as will a better chemical interaction between fill and matrix [10–17]. However, particle dispersion does not necessarily follow this trend—a composite with well-dispersed filler does not necessarily have a higher thermal conductivity than a composite with poorly dispersed filler. This ambiguity exists because aggregation and alignment of filler particles can increase the directional thermal conductivity of the composite [12,18–20]. Since TIM pads only require high heat transfer rates in the normal direction, vertically aligning the fill material in the matrix presents a path for increasing performance while holding all other parameters constant [21–24].

Previous works have demonstrated that aligned fill material in a polymer matrix can greatly enhance the directional thermal conductivity of the composite and that composites with high aspect ratio filler particles benefit most from alignment [25–27]. Flow of the uncured polymer, for example, is an effective method for aligning high aspect ratio particles [28,29]. However, in most microelectronics applications—such as the case of underfill—flow of the uncured composite is perpendicular to the direction of desired fill alignment. An alternative approach that enables high control over the preferential particle direction is alignment by a magnetic field.

Ferrous fill material in a polymer matrix can be easily aligned in a controlled magnetic field [25,30–32]. Furthermore, simple, uniaxial magnetic field alignment of spheroid nickel particles doubles the thermal conductivity of the composite (as compared to the unaligned particle composites), achieving a thermal conductivity enhancement of more than 4× at a fill volume fraction, ϕ, of 0.3 over the matrix alone [33]. Magnetic alignment of nickel platelets shows an even greater increase due to alignment and can do so at smaller fill volume fractions. For example, Solis et al. showed an enhancement in thermal conductivity of 20× at $\phi = 0.15$ over the matrix material (a 4× increase over unaligned sample) [34]. The authors of these two works [33,34] went on to further explore how various types of magnetic fields affect particle alignment and conclude that the applied magnetic field will align the particles in a structure that is optimal for good thermal transport [35]. Thus, magnetic alignment of fill in a polymer matrix is a simple and effective method for improving the composites thermal performance. However, the thermal performance of soft composites with magnetically aligned particles under compression in ranges relevant to microelectronic applications (strain of at least 25% or more [36]) has not been investigated. In this work, we experimentally fill this knowledge gap by (i) investigating thermal

[1]Corresponding authors.

Contributed by the Heat Transfer Division of ASME for publication in the Journal of Heat Transfer. Manuscript received June 18, 2018; final manuscript received August 29, 2018; published online October 24, 2018. Assoc. Editor: Ravi Prasher.

 Copyright © 2019 by ASME

Downloaded From: http://heattransfer.asmedigitalcollection.asme.org on 10/24/2018 Terms of Use: http://www.asme.org/about-asme/terms-of-use

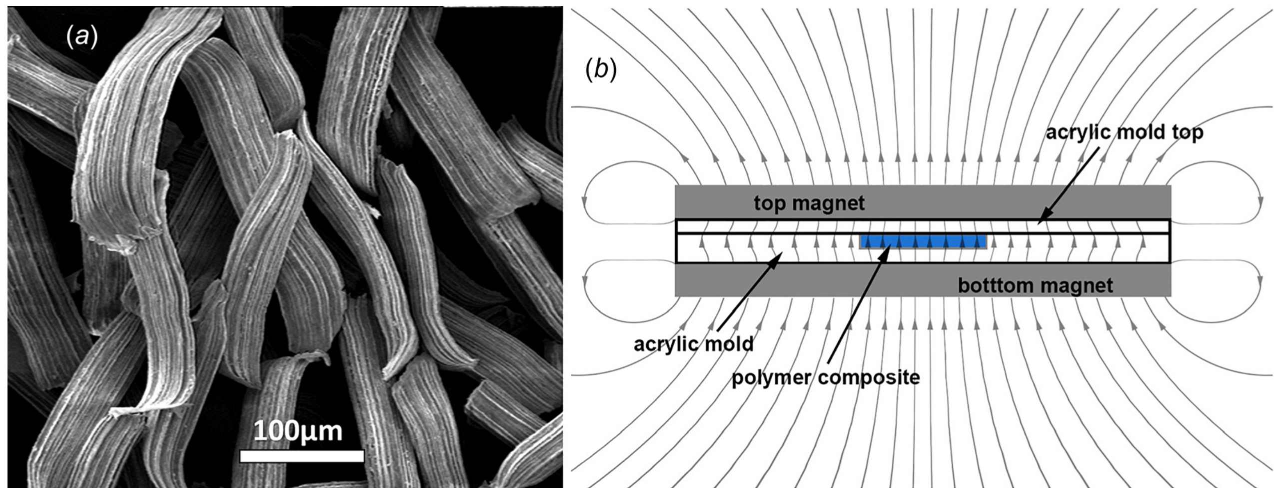

Fig. 1 (*a*) Scanning electron microscopy image of the nickel fibers used in these composites and (*b*) illustration showing the molding and magnetic alignment of the nickel fiber–polymer composites including a schematic of the applied magnetic field

transport changes caused by magnetically aligned nickel fibers in a soft silicone matrix and (ii) investigating the effects of compression on these composite pads. Intriguingly, we demonstrate that the thermal resistance of the pads with aligned fibers increases under compression. Using further experiments and theoretical arguments, we reveal that this increase stems from buckling of the fiber columns under compressive strain.

Methods

Fabrication. The matrix material in this work is Smooth-On EcoFlex 00-20, which is a very soft, platinum cured silicone elastomer with a thermal conductivity, k, of 0.3 ± 0.03 W m^{-1} K^{-1} (95% uncertainty). The nickel fibers (50 μm wide $\times$ 20 μm thick $\times$ 250 μm long from IntraMicron (Aubum, AL), Fig. 1(*a*)) are mixed into the matrix with a mortar and pestle. Large nickel fibers were selected for this work so that fiber alignment in the polymer matrix could be easily observed and characterized with an optical microscope. The uncured composite is vacuum degassed to remove air bubbles and then poured into a 1.5 mm $\times$ 12.7 mm $\times$ 12.7 mm acrylic mold. The top is placed on the mold, removing any excess material, and magnets (BY0Y02 from K&J Magnetics, Inc., 2 in $\times$ 2 in $\times$ 1/8 in, NdFeB, Grade N42) are placed on top and bottom of the mold for aligned fiber composites, as illustrated in Fig. 1(*b*). The magnetic field strength at the center of the sample is estimated at around 1400 gauss, based on estimates from the manufacturer's online calculator for magnetic field strength [37]. For unaligned composites, a weight is placed on top of the mold during cure. Since the samples with $\phi = 0.25$ and 0.35 are too viscous to pour, they are scooped into the mold and packed in with the pestle. The composites are cured in the mold at room temperature for 3 h.

Thermal Measurements. Thermal resistance is measured in the direction of fiber alignment with a stepped bar apparatus (SBA) [38,39], which is based on the ASTM D5470 standard for measuring thin, insulating materials. A linear encoder on the SBA measures the distance between the reference bars and, subsequently, the compressed thickness of the composite sample. Concurrent measurements of applied pressure were also performed using a load cell integrated with the SBA (see Fig. S1, which is available under the "Supplemental Materials" tab for this paper on the ASME Digital Collection). Thermal conductivities are calculated using the measured thermal resistance and thickness of the compressed sample as

$$k = \frac{t_c}{R} \tag{1}$$

where t_c is the compressed thickness of the sample in meters and R is the measured thermal resistance in m^2 K W^{-1}. The average temperature of the samples during thermal measurement is around 55 °C. The system has been validated using reference silicone samples (refer to Ralphs et al. [18] for details).

A thin layer of liquid galinstan (Rotometals) is applied on top and bottom of each sample to minimize contact resistance between the sample and reference bars. Note that the copper bars are not affected by gallium within the timeframe of the experiments [18]. Thus, while the measured values in this paper are effective thermal conductivities and include the thermal contact resistance between the sample and the reference bars, the difference between the measured value and the bulk composite thermal conductivity is assumed to be small. The effect of thermal contact resistance is also further minimized by our use of relatively thick samples that are 1.5 mm thick (no compression) and 0.85 mm thick (full compression with strain = 0.45).

Buckling. The buckling behavior of the nickel fiber columns encapsulated in the polymer was observed with an optical microscope (Zeiss Axio Zoom.V16 with an objective lens of 2.3×/0.57 FWD and 10.6 mm focal length Zeiss PlanNeoFluar Z) while the composites were compressed in a vise. The effects of the aligned nickel columns buckling are most easily visualized at $\phi = 0.05$ (Fig. 5(*b*) inset and Fig. S2 in supporting information, available under the "Supplemental Materials" tab for this paper on the ASME Digital Collection). This image clearly shows that the aligned columns of nickel fibers buckle with increased compressive strain. As illustrated in Fig. 2, the aligned columns buckle

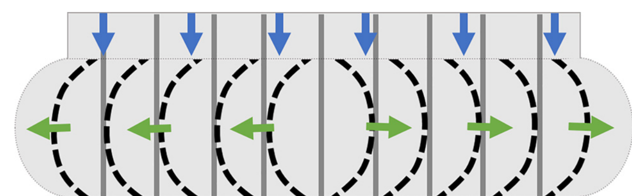

Fig. 2 Illustration of the Poisson's effect on the orientation of fiber buckling, which causes the fibers to buckle outward in the radial direction

Downloaded From: http://heattransfer.asmedigitalcollection.asme.org on 10/24/2018 Terms of Use: http://www.asme.org/about-asme/terms-of-use

outward, radially, which is most likely driven by Poisson's effect. Specifically, the nickel fiber columns appear to be tracking the continuum mechanics deformation field rather than buckling in random fashion. Since the pressure applied to these composites is not large enough to significantly deform the nickel fibers themselves (under 1 MPa), the length (or arc length) of the aligned nickel columns should remain constant as they buckle. However, because the optical images do not capture out of plane deformations (the columns could be buckling in or out of the plane of focus), it is difficult to confirm this. The increase in thermal resistance with strain is reversible (see Fig. S5 in supporting information for details, available under the "Supplemental Materials" tab for this paper on the ASME Digital Collection), signifying no permanent damage or deformations are incurred. Therefore, tears in the minimal amount of polymer matrix that hold the nickel fiber columns together can be ruled out along with nickel fibers slipping past each other as the composite is compressed. Thus, it is assumed that the length of the buckling nickel fiber columns remain constant as strain increases.

Image Processing for Fiber Alignment. Alignment of the nickel fibers was evaluated by image processing with ImageJ, by manually drawing lines on top of the individual fibers. The angle of the fibers varied from 0 deg to the right to 180 deg on the left with 90 deg corresponding to a fiber aligned from bottom to top of the composite. The angle measurements in Fig. 3 and histograms in Fig. S3 (see "Supplemental Materials" tab for this paper on the ASME Digital Collection) show the results from at least 200 fiber orientation measurements per ϕ for both aligned and unaligned composites. The angle measurements were sorted and every fourth to eighth angle was plotted in order to distinguish individual data points, depending on how many fiber orientation measurements were available.

Scanning Electron Microscopy of Nickel Fibers. Nickel fibers were suspended in ethanol and then drop cast on a piece of a silicon wafer to prepare them for scanning electron microscopy (SEM). Once the ethanol had evaporated, the SEM (Amray 1910 with field emission gun) was conducted at 20 kV, a working distance of 12.1 mm, and a SEM-software defined spot size of 0.0.

Results and Discussion

The nickel fibers used in this work have an aspect ratio around 7 (averaging the two transverse fiber dimensions), which is between that of the magnetically aligned spheroid nickel particles (aspect ratio = 1) and nickel platelets (aspect ratio = 20) utilized in previous work on thermal conductivity enhancement through magnetic alignment of filler particles in an epoxy matrix with $k = 0.23$ W m^{-1} K^{-1} [33,34]. Consequently, addition of the nickel fibers to the silicone matrix results in a thermal conductivity enhancement greater than that obtained by addition of the spheroid nickel particles but lower than that achieved by addition of the nickel platelets (see Fig. 4(*a*)). As the nickel fibers are exposed to the magnetic field, the fibers themselves become magnetized and aggregate together forming fiber columns inside the matrix. This segregation and alignment into columns is visually most notable at $\phi = 0.05$, but is also easy to observe with $\phi = 0.15$ (see Fig. 3). At $\phi = 0.25$ and 0.35, there is very little evidence of alignment or reorientation of the fibers. In more quantitative terms, the plots in Figs. 3(*b*), 3(*d*), 3(*f*), and 3(*h*) show graphical representations of the fiber alignment distribution estimated using image processing from the two-dimensional images. In our definition, the fiber alignment angle varies from 0 deg to 180 deg, where 90 deg corresponds to a line connecting from bottom to top of the composite. From these plots, it is evident that alignment by the magnetic field is less effective at higher ϕ (for more info, see Fig. S4 in the "Supplemental Materials" tab for this paper on the ASME Digital Collection). Specifically, the angular distributions of the aligned fibers at $\phi = 0.05$ and $\phi = 0.15$ are highly anisotropic and concentrated around 90 deg (vertical across the composite). In turn, those of the aligned fibers at $\phi = 0.25$ and $\phi = 0.35$ are isotropic (uniformly distributed) and indistinguishable from the isotropic angle distributions of the fibers that were not exposed to magnetic field. While, as expected from our alignment angle definition, for all distributions, the average fiber alignment angle is around 90 deg, the associated standard deviations increase dramatically from 11.3 deg and 27.8 deg for $\phi = 0.05$ and 0.15 to 46.3 deg and 47.6 deg for $\phi = 0.25$ and 0.35. The standard deviation of unaligned samples was measured to be between 48 and 55 deg, and so these angle measurements confirm our qualitative observations of diminishing effectiveness of magnetic field alignment at higher ϕ.

The decrease of the effect of magnetic field on fiber orientation at higher fill fraction likely stems from increased particle jamming and translates into diminishing thermal conductivity enhancements. Specifically, since the volume of the composites was confined in the mold during exposure to the magnetic field, the ability of the fibers to move in response to the field is highly dependent on their packing. According to Toll [40], the maximum packing factor for these fibers is around 35%, thus explaining the diminishing magnetic alignment as fiber volumetric fraction approaches this limit. In essence, at lower volumetric ratios, particles can freely reorient themselves in response to the magnetic field without interacting with other particles. Near the packing limit, however, volume around the fibers is predominantly occupied by other fibers, which restrict each other's movements. This diminishing ability of the fibers to align at high volume fractions naturally translates into a decreasing magnetic enhancement in thermal conductivity for composites measured at low strain, ϵ, below 0.05 (see Fig. 4(*b*)). Specifically, magnetic alignment more than doubles (from 0.4 to 1.1 W m^{-1} K^{-1}) and triples (from 0.7 to 2.2 W m^{-1} K^{-1}) the thermal conductivity of the composite at $\phi = 0.05$ and $\phi = 0.15$, respectively. In contrast, at $\phi = 0.25$ magnetic alignment enhances the thermal conductivity only by a factor of 1.3 (from 1.4 to 1.9 W m^{-1} K^{-1}) and has no detectable effect at $\phi = 0.35$. Thus, magnetic alignment of fibers provides a significant thermal conductivity enhancement only at fill fractions appreciably below the packing limit.

The plots in Fig. 5 demonstrate that, intriguingly, the thermal properties of the magnetically enhanced composite pads deteriorate with increased compressive strain. Specifically, for the sample with $\phi = 0.05$, inducing compressive strain up to 0.45 decreases the thermal conductivity of the composite from 1.15 to 0.6 W m^{-1} K^{-1} (increases thermal resistance from 1.32×10^{-3} to 1.52×10^{-3} m^2 K W^{-1}). The corresponding side-view images of the pads under compression shown in the inset in Fig. 5(*b*) reveal gradual buckling of the fiber columns. Consequently, the counterintuitive degradation of thermal properties of the magnetically enhanced composites under compression likely stems from column-buckling induced changes to the conduction path and/or interparticle thermal resistance.

In order to quantify the role of the nickel fiber column buckling, we have developed two simple models for the thermal conductivity of the compressed composites. The first, most basic model treats the composite as a parallel network of nickel fiber columns and silicone. During compression, the length of the nickel fiber column is assumed to remain constant while the thickness of the matrix material decreases. This simple parallel model is given by

$$k = \frac{t_c}{A}\left(\frac{k_{\mathrm{NFC}}A_{\mathrm{NFC}}}{t_0} + \frac{k_p A_p}{t_c}\right) = \left(k_{\mathrm{NFC}}\frac{t_c}{t_0}\frac{A_{\mathrm{NFC}}}{A} + k_p\frac{A_p}{A}\right) \tag{2}$$

where t_c is the compressed thickness of the composite, t_0 is the uncompressed thickness of the composite, A is the area of the composite, A_{NFC} is the area of the aligned nickel fiber column (NFC), A_p is the area of the polymer matrix, k_p is the thermal conductivity of the polymer, and

Downloaded From: http://heattransfer.asmedigitalcollection.asme.org on 10/24/2018 Terms of Use: http://www.asme.org/about-asme/terms-of-use

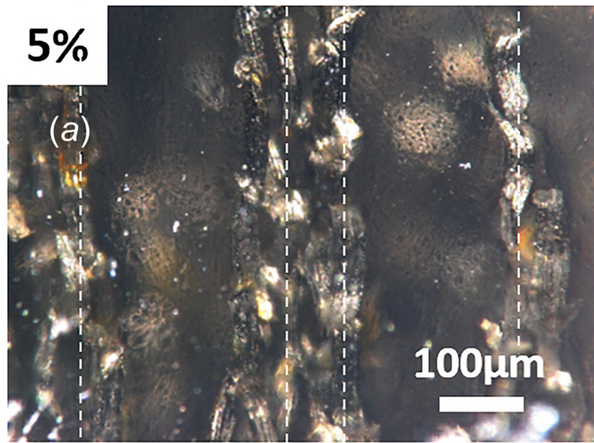

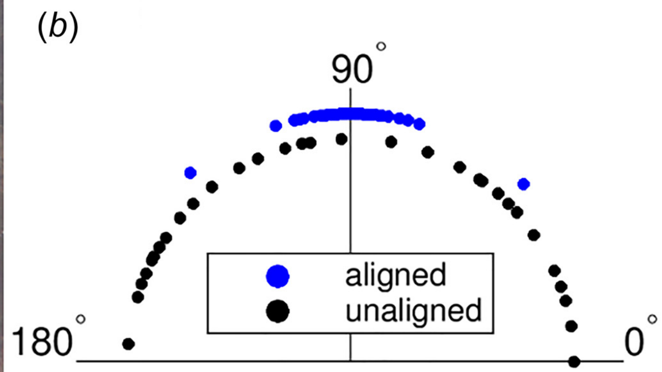

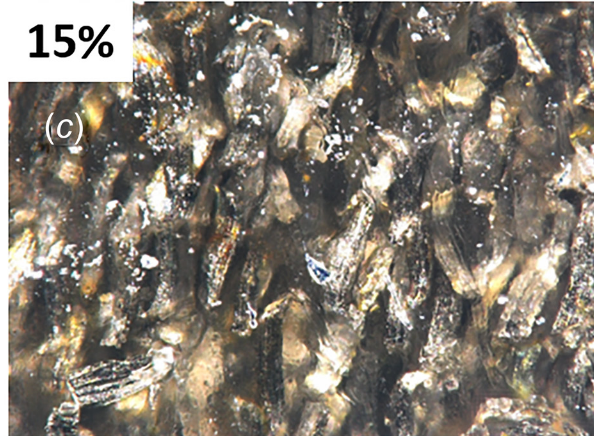

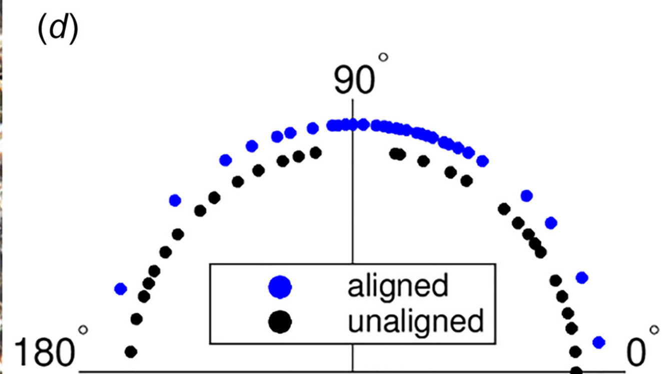

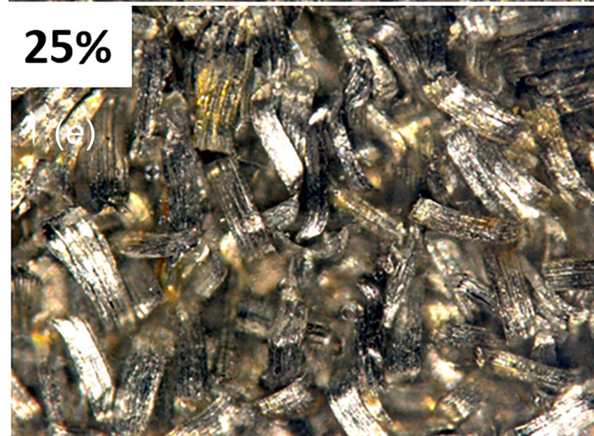

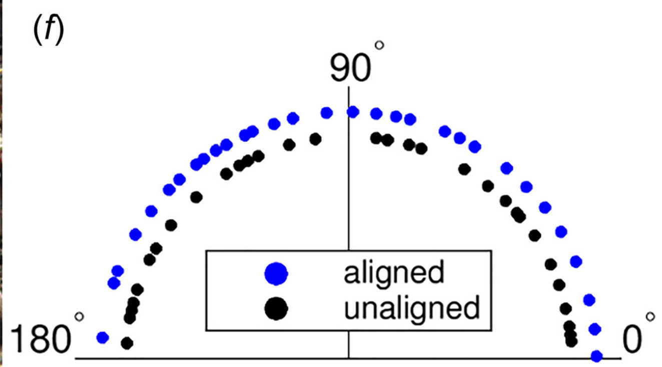

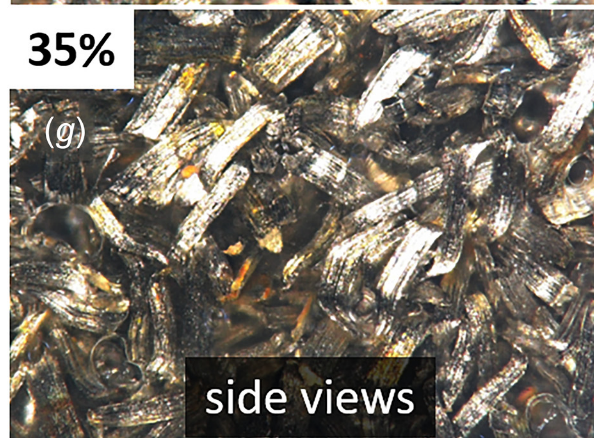

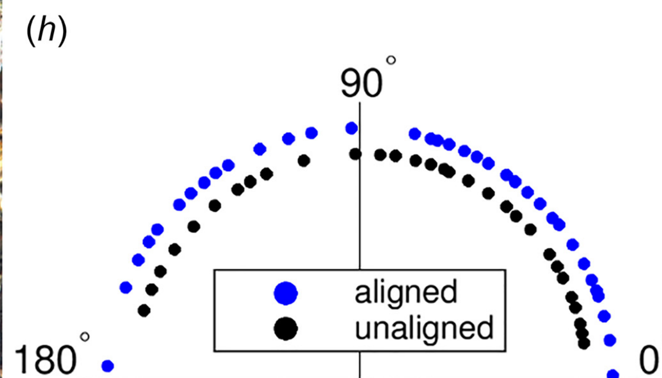

Fig. 3 Optical microscope images of the aligned (top to bottom) nickel fiber–polymer composites under zero compressive strain at nickel fiber volume fractions of 0.05 (*a*), 0.15 (*c*), 0.25 (*e*), and 0.35 (*g*) along with fiber alignment measurements ((*b*), (*d*), (*f*), and (*h*)), respectively. White lines in (*a*) highlight aligned fiber column axis.

Downloaded From: http://heattransfer.asmedigitalcollection.asme.org on 10/24/2018 Terms of Use: http://www.asme.org/about-asme/terms-of-use

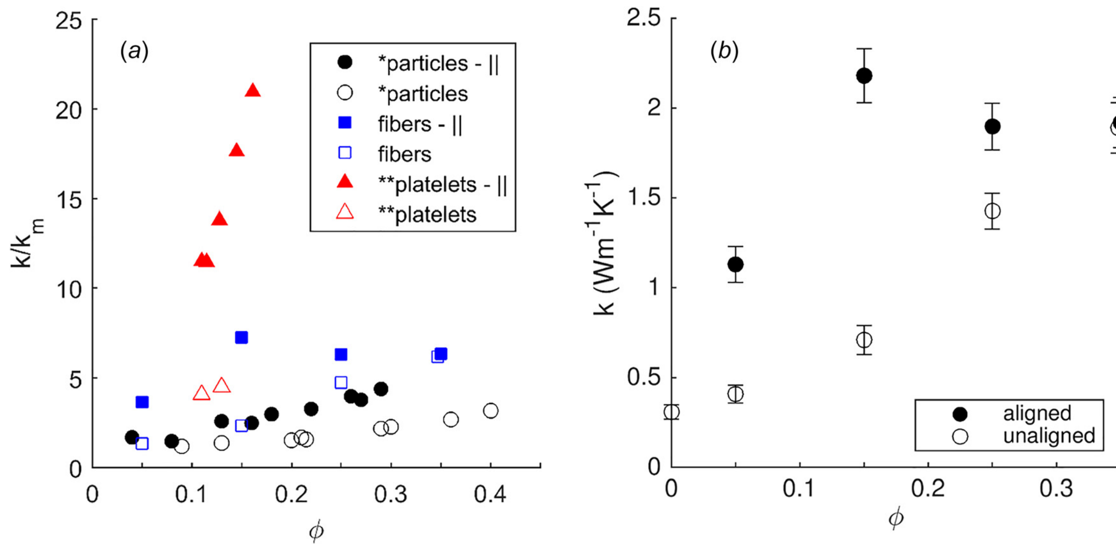

Fig. 4 (a) Fill volume fraction, ϕ, versus the thermal conductivity enhancement over that of the matrix material for aligned (||) and unaligned nickel particles, nickel fibers, and nickel platelets. Data for the nickel particles* and nickel platelets are taken from Refs. [33] and [34], respectively. (b) Measured thermal conductivity for aligned and unaligned nickel fibers in the polymer matrix at various ϕ. Nickel fiber measurements are at low strain ($\epsilon < 0.05$).**

$$k_{\mathrm{NFC}} = \frac{t_0}{A_{\mathrm{NFC}} R_{\mathrm{NFC}}} \tag{3}$$

R_{NFC} is calculated from

$$R_{\mathrm{NFC}} = R_p + R_N + R_b \tag{4}$$

where R_p, R_N, and R_b are the total thermal resistances of the polymer, nickel, and interfacial boundary resistance at the nickel–polymer interfaces within the fiber columns, respectively. This model, and all following models, assumes one-dimensional heat transfer, constant temperature boundary conditions on top and bottom of the sample, constant properties, and neglects any geometrical variation from Poisson's effect as the composite is compressed. For this nickel fiber–polymer column series model, illustrated in Fig. 5(c), we used image processing to roughly estimate that 99% of the column length is occupied by nickel ($k_N = 90$ W m^{-1} K^{-1} [41,42]), while the remaining 1% is occupied by the polymer ($k_p = 0.3 \pm 0.03$ W m^{-1} K^{-1}, 95% confidence interval). We derived these geometrical estimates by drawing lines on top of aligned nickel fiber columns in the cross-sectional images and used ImageJ to measure the length of distinct polymer junctions between nickel fibers along that line, resulting in an estimate of 1.2±0.6% (68% confidence interval) of the line being occupied by the polymer. This value has a measurable effect on the calculated thermal conductivity of the composite, with a change in the thickness of the polymer in the calculations from 1% of the total column length to 0.5% and 1.5% resulting in a change in thermal conductivities of the uncompressed composite from 1.2 W m^{-1} K^{-1} to 1.6 and 1.0 W m^{-1} K^{-1}, respectively. Since in our simple models we are using a highly idealized nickel–polymer–nickel gap geometry that does not account for

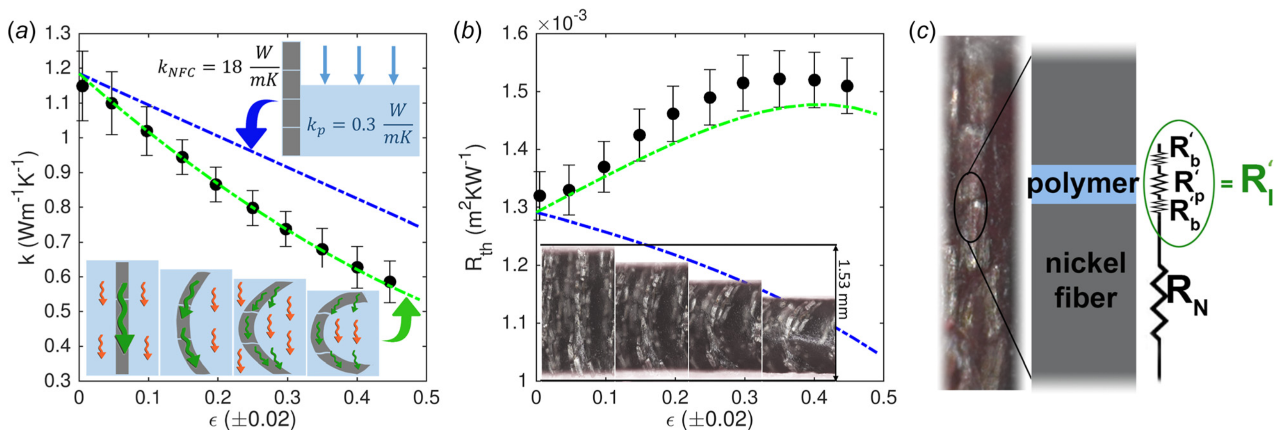

Fig. 5 Measured (points) and theoretical (lines) values for (a) thermal conductivity and (b) thermal resistance at a nickel fiber volume fraction of 0.05 as compressive strain increases; and (c) a simple resistance network at the junction between two aligned nickel fibers in the polymer matrix. Inset (a) (bottom) shows a schematic illustrating the transition from parallel to series heat conduction (see Fig. S4 which is available under the "Supplemental Materials" tab for this paper on the ASME Digital Collection, for a more detailed schematic) that is the basis for the theoretical model for the dashed line that more closely fits the measured values in both (a) and (b) and inset (b) shows optical microscope images supporting the schematic in inset (a) (bottom). Inset (a) (top) shows a schematic for the theoretical model on which the line well above the measured values in (a) and well below the measured values in (b) is based.

Downloaded From: http://heattransfer.asmedigitalcollection.asme.org on 10/24/2018 Terms of Use: http://www.asme.org/about-asme/terms-of-use

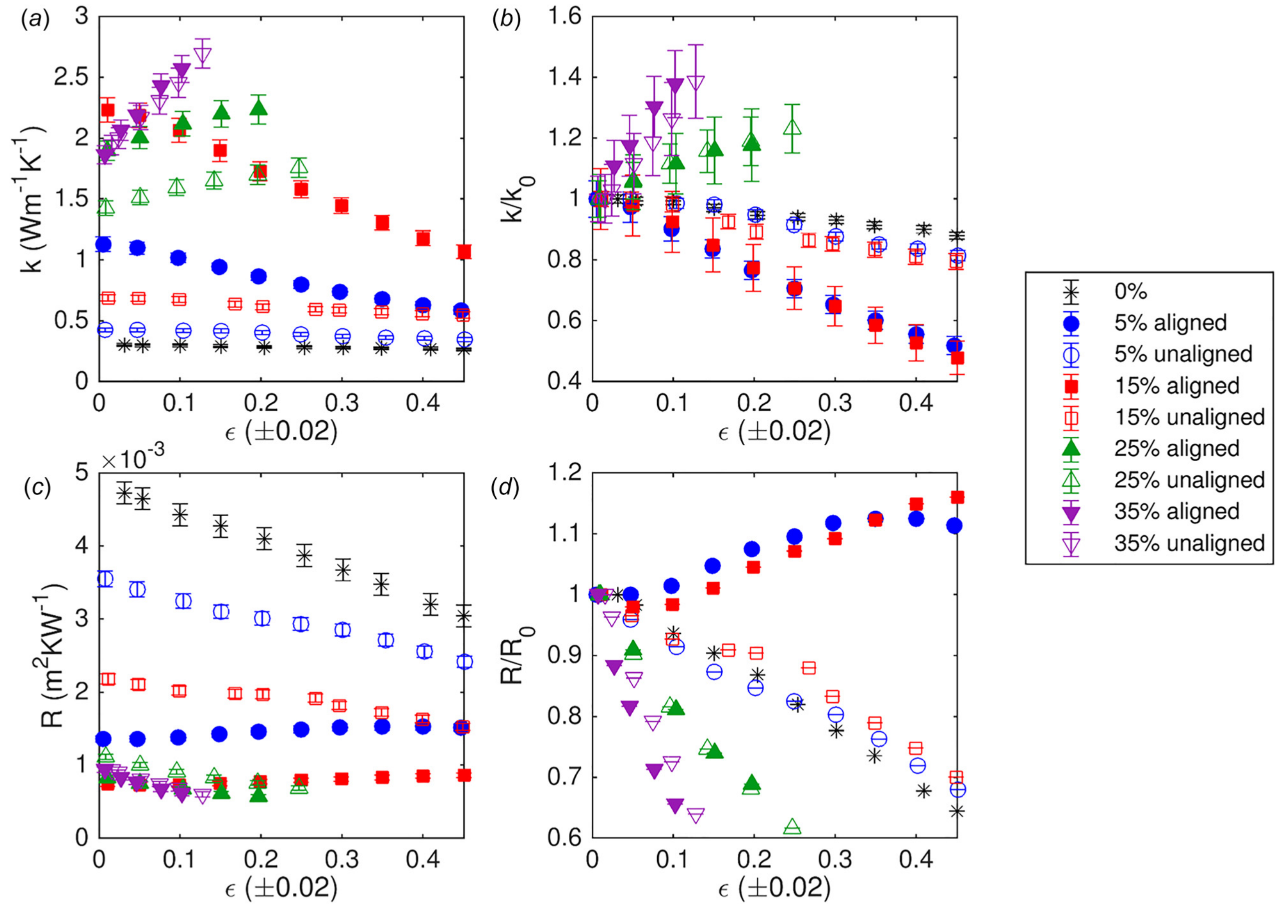

Fig. 6 **(*a*) Measured thermal conductivity, (*b*) ratio of compressed thermal conductivity to uncompressed thermal conductivity, (*c*) measured thermal resistance, and (*d*) ratio of compressed thermal resistance to uncompressed thermal resistance for various nickel fiber volume fractions and increasing compressive strain, ϵ**

any three-dimensional geometrical imperfections (e.g., fiber misalignment, partial overlapping, etc.), we use the representative rounded-down value of 1% within the models. Use of this value is validated by matching of the calculated and measured thermal conductivity of the uncompressed composite of 1.2 W m^{-1} K^{-1}. To calculate this value, we also had to set R_b, which, overall, has a minor effect on thermal conductivity of the composite. Specifically, we set R_b to 1.7×10^{-5} m^2 K W^{-1}. Such values are typical if little to no effort is taken to achieve a chemically clean interface between particles and matrix [2,43]. We note that in our definition of R_b, it corresponds to the sum over all interfaces in the fiber column. Since there are five to six fibers with 0.25 mm height in the 1.5 mm thick samples, there are about ten such interfaces per column. Thus, the per interface R'_b illustrated in Fig. 5(*c*) is 1.7×10^{-6} m^2 K W^{-1}, corresponding to the middle of the 10^{-5} to 10^{-7} m^2 K W^{-1} range applicable for metal particle-laden composites. With these parameters, the thermal conductivity for the aligned NFCs is estimated at 18 W m^{-1} K^{-1}. Decreasing R_b to 5×10^{-6} m^2 K W^{-1} results in a NFC thermal conductivity of 21 W m^{-1} K^{-1} and a minor increase of the composite thermal conductivity to 1.3 W m^{-1} K^{-1}. Thus, while R_b is incorporated in this model, its effect on the composites' thermal conductivity is small.

The trend line that lies well above the data in Fig 5(*a*) and well below the data in Fig 5(*b*) shows the predicted change in the thermal conductivity and resistivity, respectively, of the composite at $\phi = 0.05$ as compressive strain increases using the basic parallel resistance model. This model reproduces the experimentally observed decreasing trend in thermal conductivity, but fails to account for the extent of degradation on the thermal conductivity at high strain. It also fails to capture the trend of increasing thermal resistance at high strain. We note that the discrepancy between experimental and predicted trends (decreasing/decreasing in Fig. 5(*a*) versus increasing/decreasing in Fig. 5(*b*)) stems from our model definitions. Specifically, both the parallel model of k in Eq. (2) and the corresponding parallel composite resistance model, t_c/kA, decrease as the sample is compressed. Similarly, compression of the sample should comparably decrease the thermal conductivity of the sample calculated from the measured thermal resistance and sample thickness (see Eq. (1)). However, the measured thermal resistance does not explicitly incorporate the sample thickness and, consequently, can either decrease or increase during compression.

As illustrated in the lower inset in Fig. 5(*a*), the discrepancy between the experimental data and the basic parallel resistance model could stem from a gradual transition of the mode of heat transfer from purely parallel heat conduction to a mixture of parallel and series conduction. This transition from parallel to series conduction is caused by the nickel columns bending out of parallel with the temperature gradient. From this observed behavior, it is assumed that the transition from parallel to series heat conduction can be scaled with increasing strain and modeled by

$$k_{\text{parallel+series}} = k_{\text{parallel}}(1-\epsilon) + k_{\text{series}}\epsilon \tag{5}$$

where k_{parallel} is given previously in Eq. (2) and

$$k_{\text{series}} = \frac{t_c}{A}\left(\frac{1}{\frac{\phi_N t_c}{k_{\text{NFC}} A} + \frac{\phi_p t_c}{k_p A}}\right) = \left(\frac{1}{\frac{\phi_N}{k_{\text{NFC}}} + \frac{\phi_p}{k_p}}\right) \tag{6}$$

where ϕ_N and ϕ_p are the volume fraction of nickel and polymer matrix, respectively. The calculated thermal conductivity and

Downloaded From: http://heattransfer.asmedigitalcollection.asme.org on 10/24/2018 Terms of Use: http://www.asme.org/about-asme/terms-of-use

thermal resistance from this model are shown by the lighter dashed line that more closely fits the data in Figs. 5(*a*) and 5(*b*), respectively, for $\phi = 0.05$. This model more accurately represents the unique thermal degradation of these aligned composites under strain and matches fairly well with the experimental values.

Although this hybrid parallel/series model fits our data, there are additional factors that may contribute to the increased thermal resistance under strain. As the aligned nickel fiber columns buckle, the interface between two fibers suffers from localized strain. This localized strain can increase the thermal resistance at the interface by either geometrical changes of the polymer filled gap, R_p, or by an increase in interfacial boundary resistance between metal and polymer, R_b. An increase in either of these resistances will increase the resistance at the interfaces, R_I (illustrated in Fig. 5(*c*)) further increasing the resistance of the composite as a whole.

The composites with $\phi = 0.15$ show a similar trend to those with $\phi = 0.05$, decreasing k and increasing R as strain increases, but $\phi = 0.25$ and 0.35 do not follow this trend. Specifically, the plots in Fig. 6 show the measured thermal conductivity and thermal resistance for various ϕ with both aligned and unaligned nickel fibers. For composites with ϕ of 0.25 and above, increasing strain increases k and decreases R. These trends stem from the previously discussed composite microstructure evolution during magnetic alignment and buckling of nickel fiber columns under compression. Specifically, compression only increases thermal resistance of samples with filler volume fraction appreciably below the packing limit, for which exposure to the magnetic field resulted in aligned nickel fiber column formation. The fiber columns, in turn, buckle under compression, leading to gradual degradation of thermal properties from mixing of parallel and series heat conduction modes.

Conclusions

Magnetic alignment of nickel fibers with an aspect ratio of 7 in a soft polymer matrix more than triple the directional thermal conductivity over unaligned fibers at $\phi = 0.15$, more than a 7× increase in thermal conductivity over the polymer matrix. Aligned nickel fibers have a higher increase in directional thermal conductivity over the matrix thermal conductivity than aligned spheroid nickel particles, but not as high as aligned nickel platelets. At $\phi = 0.05$ and 0.15 with aligned fibers, there is more than a 10% increase in thermal resistance as the composite is compressed. This increase in resistance is caused by a transition from purely parallel heat conduction at $\epsilon \approx 0$ between aligned nickel columns and the polymer matrix to a combination of parallel and series heat conduction scaled with strain.

The increase in thermal resistance as the composite is compressed highlights a potential pitfall when using fill material alignment to increase soft composite thermal conductivity. Many soft composites are put under strain for standard operations and must perform well under those circumstances. Thermal interface materials, for example, are put under a set and constant load when installed, and then undergo further fluctuations in strain as the neighboring components undergo thermal cycling. Thus, the increase in thermal resistance with strain in aligned soft composites must be considered when designing TIMs for these applications.

Acknowledgment

The authors would like to thank Mr. Praveen Kotagama and Mr. Wilson Kong from ASU for commenting on the manuscript.

Funding Data

- M. I. R. acknowledges support through Arizona State University's (ASU) Fulton Schools of Engineering Dean's Fellowship. K. R. and R. Y. W. acknowledge funds from the Ira A. Fulton Schools of Engineering at ASU.

Nomenclature

A = area
k = thermal conductivity
NFC = nickel fiber column
R, R_{th} = thermal resistance
R_b = cumulative thermal boundary resistance at all nickel-polymer interfaces in an aligned NFC
R_b' = thermal boundary resistance at the interface between a single fiber and the polymer matrix in the interface between two fibers in a NFC
R_I' = resistance at the interface between two nickel fibers in a NFC
R_p' = thermal resistance of the polymer between two nickel fibers in a NFC
t_c = compressed thickness
ϵ = compressive strain
ϕ = fill volume fraction

Subscripts

N = nickel
NFC = nickel fiber column
P = polymer

References

[1] Bartlett, M. D., Kazem, N., Powell-Palm, M. J., Huang, X., Sun, W., Malen, J. A., and Majidi, C., 2017, "High Thermal Conductivity in Soft Elastomers With Elongated Liquid Metal Inclusions," Proc. Natl. Acad. Sci., **114**(9), pp. 3–8.
[2] Prasher, R. S., and Chiu, C.-P., 2017, "Thermal Interface Materials," Materials for Advanced Packaging, springer, New York, pp. 511–535.
[3] Gurrum, S. P., Suman, S. K., Joshi, Y. K., and Fedorov, A. G., 2004, "Thermal Issues in Next-Generation Integrated Circuits," IEEE Trans. Device Mater. Reliab., **4**(4), pp. 709–714.
[4] Moore, A. L., and Shi, L., 2014, "Emerging Challenges and Materials for Thermal Management of Electronics," Mater. Today, **17**(4), pp. 163–174.
[5] Mark, J. E., 2009, *Polymer Data Handbook*, Oxford University Press, New York.
[6] Choy, C. L., 1977, "Thermal Conductivity of Polymers," Polymer, **18**(10), pp. 984–1004.
[7] Chen, H., Ginzburg, V. V., Yang, J., Yang, Y., Liu, W., Huang, Y., Du, L., and Chen, B., 2016, "Thermal Conductivity of Polymer-Based Composites: Fundamentals and Applications," Prog. Polym. Sci., **59**, pp. 41–85.
[8] Sarvar, F., Whalley, D., and Conway, P., 2006, "Thermal Interface Materials - A Review of the State of the Art," First Electronic Systemintegration Technology Conference, Dresden, Germany, Sept. 5–7, pp. 1292–1302.
[9] Schaller, R. R., 1997, "Moore's Law: Past, Present, and Future," IEEE Spectr., **34**(6), pp. 52–59.
[10] Burger, N., Laachachi, A., Ferriol, M., Lutz, M., Toniazzo, V., and Ruch, D., 2016, "Review of Thermal Conductivity in Composites: Mechanisms, Parameters and Theory," Prog. Polym. Sci., **61**, pp. 1–28.
[11] Xue, Q., 2004, "The Influence of Particle Shape and Size on Electric Conductivity of Metal-Polymer Composites," Eur. Polym. J., **40**(2), pp. 323–327.
[12] Mamunya, Y. P., Davydenko, V. V., Pissis, P., and Lebedev, E. V., 2002, "Electrical and Thermal Conductivity of Polymers Filled With Metal Powders," Eur. Polym. J., **38**(9), pp. 1887–1897.
[13] Wong, C. P., and Bollampally, R. S., 1999, "Thermal Conductivity, Elastic Modulus, and Coefficient of Thermal Expansion of Polymer Composites Filled With Ceramic Particles for Electronic Packaging," J. Appl. Polym. Sci., **74**(14), pp. 3396–3403.
[14] Seshadri, I., Esquenazi, G. L., Borca-Tasciuc, T., Keblinski, P., and Ramanath, G., 2015, "Multifold Increases in Thermal Conductivity of Polymer Nanocomposites Through Microwave Welding of Metal Nanowire Fillers," Adv. Mater. Interfaces, **2**(15), pp. 1–6.
[15] Hong, W.-T., and Tai, N.-H., 2008, "Investigations on the Thermal Conductivity of Composites Reinforced With Carbon Nanotubes," Diamond Relat. Mater., **17**(7–10), pp. 1577–1581.
[16] Balberg, I., Binenbaum, N., and Wagner, N., 1984, "Percolation Thresholds in the Three-Dimensional Sticks System," Phys. Rev. Lett., **52**(17), pp. 1465–1468.
[17] Lonjon, A., Demont, P., Dantras, E., and Lacabanne, C., 2012, "Low Filled Conductive P(VDF-TrFE) Composites: Influence of Silver Particles Aspect Ratio on Percolation Threshold From Spheres to Nanowires," J. Non. Cryst. Solids, **358**(23), pp. 3074–3078.
[18] Ralphs, M. I., Kemme, N., Vartak, P. B., Joseph, E., Tipnis, S., Turnage, S., Solanki, K. N., Wang, R. Y., and Rykaczewski, K., 2018, "In Situ Alloying of Thermally Conductive Polymer Composites by Combining Liquid and Solid Metal Microadditives," ACS Appl. Mater. Interfaces, **10**(2), pp. 2083–2092.

Downloaded From: http://heattransfer.asmedigitalcollection.org/ on 10/24/2018 Terms of Use: http://www.asme.org/about-asme/terms-of-use

[19] Kusy, R. P., and Corneliussen, R. D., 1975, "The Thermal Conductivity of Nickel and Copper Dispersed in Poly (Vinyl Chloride)," Polym. Eng. Sci., **15**(2), pp. 107–112.
[20] Lebovka, N., Lisunova, M., Mamunya, Y. P., and Vygornitskii, N., 2006, "Scaling in Percolation Behaviour in Conductive-Insulating Composites With Particles of Different Size," J. Phys. D, **39**(10), pp. 2264–2271.
[21] Xie, X. L., Mai, Y. W., and Zhou, X. P., 2005, "Dispersion and Alignment of Carbon Nanotubes in Polymer Matrix: A Review," Mater. Sci. Eng., R, **49**(4), pp. 89–112.
[22] Jopek, H., and Strek, T., 2009, "Optimization of the Effective Thermal Conductivity of a Composite," Convection Conduction Heat Transfer, InTech, London, pp. 197–213.
[23] Feng, C. P., Bai, L., Shao, Y., Bao, R. Y., Liu, Z. Y., Yang, M. B., Chen, J., Ni, H. Y., and Yang, W., 2017, "A Facile Route to Fabricate Highly Anisotropic Thermally Conductive Elastomeric POE/NG Composites for Thermal Management," Adv. Mater. Interfaces, **5**(2), pp. 1–7.
[24] Han, Z., and Fina, A., 2011, "Thermal Conductivity of Carbon Nanotubes and Their Polymer Nanocomposites: A Review," Prog. Polym. Sci., **36**(7), pp. 914–944.
[25] Yuan, C., Duan, B., Li, L., Xie, B., Huang, M., and Luo, X., 2015, "Thermal Conductivity of Polymer-Based Composites With Magnetic Aligned Hexagonal Boron Nitride Platelets," ACS Appl. Mater. Interfaces, **7**(23), pp. 13000–13006.
[26] Renteria, J., Legedza, S., Salgado, R., Balandin, M. P., Ramirez, S., Saadah, M., Kargar, F., and Balandin, A. A., 2015, "Magnetically-Functionalized Self-Aligning Graphene Fillers for High-Efficiency Thermal Management Applications," Mater. Des., **88**, pp. 214–221.
[27] Tian, X., Itkis, M. E., Bekyarova, E. B., and Haddon, R. C., 2013, "Anisotropic Thermal and Electrical Properties of Thin Thermal Interface Layers of Graphite Nanoplatelet-Based Composites," Sci. Rep., **3**(1), p. 1710.
[28] Schmidt, G., and Malwitz, M. M., 2003, "Properties of Polymer-Nanoparticle Composites," Curr. Opin. Colloid Interface Sci., **8**(1), pp. 103–108.
[29] Hill, R. F., and Supancic, P. H., 2002, "Thermal Conductivity of Platelet-Filled Polymer Composites," J. Am. Ceram. Soc., **85**(4), pp. 851–857.
[30] Yan, H., Tang, Y., Long, W., and Li, Y., 2014, "Enhanced Thermal Conductivity in Polymer Composites With Aligned Graphene Nanosheets," J. Mater. Sci., **49**(15), pp. 5256–5264.
[31] Martin, J. E., 2013, "Field-Structured Polymer Composites," Macromol. Symp., **329**(1), pp. 162–172.
[32] Kimura, T., Ago, H., Tobita, M., Ohshima, S., Kyotani, M., and Yumura, M., 2002, "Polymer Composites of Carbon Nanotubes Aligned by a Magnetic Field," Adv. Mater, **14**(19), pp. 1380–1383.
[33] Martin, J. E., and Gulley, G., 2009, "Field-Structured Composites for Efficient, Directed Heat Transfer," J. Appl. Phys., **106**(8), p. 084301.
[34] Solis, K. J., and Martin, J. E., 2012, "Field-Structured Magnetic Platelets as a Route to Improved Thermal Interface Materials," J. Appl. Phys., **111**(7), p. 073507.
[35] Martin, J. E., and Snezhko, A., 2013, "Driving Self-Assembly and Emergent Dynamics in Colloidal Suspensions by Time-Dependent Magnetic Fields," Rep. Prog. Phys., **76**(12), p. 126601.
[36] Otiaba, K. C., Ekere, N. N., Bhatti, R. S., Mallik, S., Alam, M. O., and Amalu, E. H., 2011, "Thermal Interface Materials for Automotive Electronic Control Unit: Trends, Technology and R&D Challenges," Microelectron. Reliab., **51**(12), pp. 2031–2043.
[37] K&J Magnetics, Inc., 2018, "The Original K&J Magnet Calculator," K&J Magnetics, Inc., Pipersville, PA, accessed July 10, 2018, https://www.kjmagnetics.com/calculator.asp?calcType=block
[38] Thompson, D. R., Rao, S. R., and Cola, B. A., 2013, "A Stepped-Bar Apparatus for Thermal Resistance Measurements," ASME J. Electron. Packag., **135**(4), p. 041002.
[39] Ralphs, M. I., Smith, B. L., and Roberts, N. A., 2016, "Technique for Direct Measurement of Thermal Conductivity of Elastomers and a Detailed Uncertainty Analysis," Meas. Sci. Technol., **27**(11), p. 115014.
[40] Toll, S., 1998, "Packing Mechanics of Fiber Reinforcements," Polym. Eng. Sci., **38**(8), pp. 1337–1350.
[41] Touloukian, Y. S., Powell, R. W., Ho, C. Y., and Klemens, P. G., 1970, *Thermal Conductivity: Metallic Elements and Alloys* (Thermophysical Properties of Matter), Vol. 1, IFI/Plenum, New York, p. 237.
[42] Powell, R. W., Tye, R. P., and Hickman, M. J., 1965, "The Thermal Conductivity of Nickel," Int. J. Heat Mass Transfer, **8**(5), pp. 679–688.
[43] Rai, A., and Moore, A. L., 2017, "Enhanced Thermal Conduction and Influence of Interfacial Resistance Within Flexible High Aspect Ratio Copper Nanowire/Polymer Composites," Compos. Sci. Technol., **144**, pp. 70–78.

Downloaded From: http://heattransfer.asmedigitalcollection.asme.org on 10/24/2018 Terms of Use: http://www.asme.org/about-asme/terms-of-use

APPENDIX D

IN SITU ALLOYING OF THERMALLY CONDUCTIVE POLYMER COMPOSITES BY COMBINING LIUQUID AND SOLID METAL MICRO-ADDITIVES

ACS APPLIED MATERIALS & INTERFACES

Research Article

Cite This: ACS Appl. Mater. Interfaces 2018, 10, 2083−2092

www.acsami.org

In Situ Alloying of Thermally Conductive Polymer Composites by Combining Liquid and Solid Metal Microadditives

Matthew I. Ralphs, Nicholas Kemme, Prathamesh B. Vartak, Emil Joseph, Sujal Tipnis, Scott Turnage, Kiran N. Solanki, Robert Y. Wang,* and Konrad Rykaczewski*

School for Engineering of Matter, Transport, and Energy, Arizona State University, Tempe, Arizona 85287, United States

Supporting Information

ABSTRACT: Room-temperature liquid metals (LMs) are attractive candidates for thermal interface materials (TIMs) because of their moderately high thermal conductivity and liquid nature, which allow them to conform well to mating surfaces with little thermal resistance. However, gallium-based LMs may be of concern due to the gallium-driven degradation of many metal microelectronic components. We present a three-component composite with LM, copper (Cu) microparticles, and a polymer matrix, as a cheaper, noncorrosive solution. The solid copper particles alloy with the gallium in the LM, in situ and at room temperature, immobilizing the LM and eliminating any corrosion issues of nearby components. Investigation of the structure−property−process relationship of the three-component composites reveals that the method and degree of additive blending dramatically alter the resulting thermal transport properties. In particular, microdispersion of any combination of the LM and Cu additives results in a large number of interfaces and a thermal conductivity below 2 W m^{-1} K^{-1}. In contrast, a shorter blending procedure of premixed LM and Cu particle colloid into the polymer matrix yields a composite with polydispersed filler and effective intrinsic thermal conductivities of up to 17 W m^{-1} K^{-1} (effective thermal conductivity of up to 10 W m^{-1} K^{-1}). The LM−Cu colloid alloying into $CuGa_2$ provides a limited, but practical, time frame to cast the uncured composite into the desired shape, space, or void before the composite stiffens and cures with permanent characteristics.

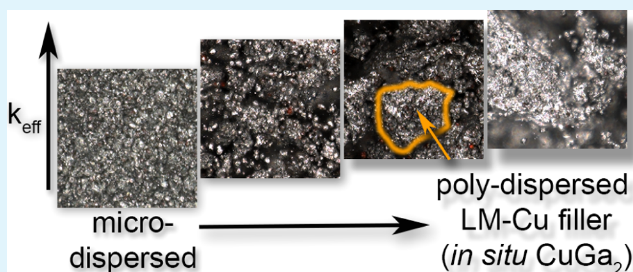

KEYWORDS: *liquid metal, thermal conductivity, in situ alloying, polymer composite, thermal interface material, particulate filler, copper, galinstan*

1. INTRODUCTION

Thermal management of integrated circuits (ICs) has become a limiting factor for transistor frequency, which has stalled around a few gigahertz over the past decade.[1,2] The large thermal loads stem from extremely densely packed, nanometer-sized features of modern ICs,[2−4] which provide minimal surface area for dissipation of the generated heat. This limitation has motivated the development of novel materials that can more efficiently conduct heat away from such hotspots.

Thermal interface materials (TIMs) play an integral role in dissipating heat away from ICs. Specifically, TIMs minimize the thermal contact resistance between electronic packaging components, such as processors and heat sinks, which stems from air gaps formed by surface mismatches of the two mating components. TIMs eliminate these air gaps by filling the geometrical imperfections with materials that have a high thermal conductivity (k). Some of the best performing commercial TIMs consist of thin metal foils with moderately low melting temperatures (T_{melt}) such as indium (T_{melt} = 157 °C, $k \approx 80$ W m^{-1} K^{-1}) or alloys such as SnBi (T_{melt} = 138 °C, $k \approx 20$ W m^{-1} K^{-1}).[5,6] However, these relatively low melting temperature materials have low mechanical compliance (as compared to that of, for example, polymer composites), which results in thermal fatigue in the IC because of the large mismatch in coefficients of thermal expansion between IC components.[7,8] This issue, along with the higher temperature required to melt and apply the indium and related films, makes room-temperature liquid metals (LMs) attractive alternatives. LMs have inherently good mechanical compliance because of their liquid state at normal IC operating temperatures.

Although a TIM made up of an array of mercury microdroplets has been described,[9] the limit of 100 ppm of mercury in any piece of electronic equipment (as dictated by the European Union's Restriction of Hazardous Substances Directive[10]), as well as general toxicity concerns, discourages the use of this metal. These limitations make gallium-based eutectic alloys such as GaIn (T_{melt} = 15.5 °C, $k \approx 32$−39 W m^{-1} K^{-1}) or GaInSn (T_{melt} = −19 °C, $k \approx 16$−39 W m^{-1} K^{-1}) much more practical for use in a TIM.[11−19] TIMs consisting of such LMs are commercially available, and several methods have been recently proposed to improve their thermal properties and wettability.[14,15]

Received: October 17, 2017
Accepted: December 13, 2017
Published: December 13, 2017

 © 2017 American Chemical Society

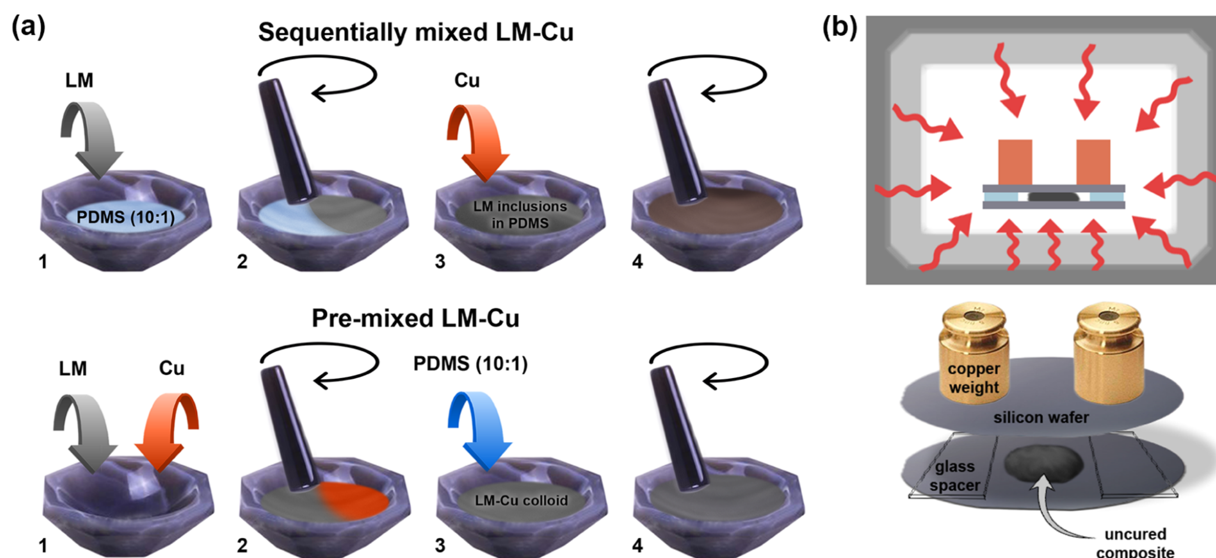

Figure 1. Schematic demonstrating the (a) difference between sequential mixing and premixing of liquid metal (LM) and copper microparticles (Cu) prior to blending into the PDMS matrix and (b) remaining fabrication procedure consisting of molding and curing.

One major concern with gallium-based LMs being used in TIMs for ICs is the rapid gallium-induced degradation of many metals used in IC packaging.[20−22] This concern is particularly severe with aluminum (one of the most common heat sink materials), which becomes extremely brittle when exposed to gallium.[21] To prevent corrosion, the mating materials can be modified through surface treatments (e.g., anodizing or introducing a tungsten barrier layer[23]), but, alternatively, gallium can be encapsulated and immobilized in a polymer matrix. This encapsulation process also resolves so-called pump-out issues, whereby voids (and correspondingly, hotspots) are created when the liquid metal is squeezed out from the gap during thermal cycling-induced device warping (see illustrative images of liquid metal side-leakage under minor compression in the Supporting Information, Figure S7).

To make polymers attractive as TIMs, thermally conductive particles are commonly added as fillers to increase the inherently low thermal conductivity of the matrix.[24−28] While the addition of many advanced materials such as carbon nanotubes, graphene, metal nanowires, boron nitride, and others has been recently investigated,[1,29−37] the majority of commercial TIMs rely on lower-cost ceramic or metal additives such as silver flakes, alumina, and graphite.[38,39] In nearly all cases, however, the effective intrinsic thermal conductivity of the composite, k, is limited by interface thermal resistances. These interface thermal resistances exist between the particles and the matrix and, when the percolation threshold is crossed, between the particle−particle contacts. Recent work has shown that k can be increased either by decreasing the particle−particle resistance (e.g., by microwave welding[31,40]) or by decreasing the number of interfaces through the matrix (e.g., by alignment of long particles[41−44]). Using LM as filler in a poly(dimethylsiloxane) (PDMS) matrix, Bartlett et al.[45] demonstrated that a high directional thermal conductivity of up to 10 W m^{-1} K^{-1} can be achieved by strain-induced spherical-to-cylindrical deformation of the microscale LM inclusions. Unfortunately, surface leakage of LM is a problem when composites with large LM inclusions[45−47] are cut or compressed (as with typical TIM applications). These types of mechanical forces drive the LM out of the polymer matrix (see Figure S5a in the Supporting Information) and hence Ga-induced corrosion of adjacent materials is still a concern.

In this work, we seek to simultaneously resolve the LM leakage issue and enhance the thermal properties of the composite by embedding both LM inclusions and copper (Cu) microparticles in a polymer matrix. In these three-component composites, the LM "glues" the copper particles together and eventually solidifies via in situ alloying of the LM and Cu into crystalline $CuGa_2$. In other words, the presented filler material system can be viewed as a solder that is molten at room temperature but then solidifies via chemical reaction (as opposed to freezing). We assert that this effect increases percolation and improves thermal pathways through the composite, thus increasing k, as well as immobilizing the LM to prevent gallium-induced degradation of nearby components. We investigate the structure−property−process relationship of these three-component composites and discuss the physical mechanisms underlying their performance.

2. EXPERIMENTAL SECTION

2.1. Composite Fabrication. We fabricated the three-component composites using the procedure outlined by Fassler et al.[46] and Bartlett et al.[45] In particular, we manually mixed together the GaInSn LM (Rotometals), Cu microparticles (10 μm APS, Alfa Aesar), and the poly(dimethylsiloxane) matrix (PDMS, Sylgard 184 with 10:1 base-to-curing agent ratio by weight) with mortar and pestle (see Figure 1a). We then poured the mixture into an open silicon mold and cured it in an oven (see Figure 1b). We controlled particle dispersion using the mixing time. Because our goal was to maximize the thermal conductivity of the composite, all samples were made at a filler volume fraction of ϕ = 0.5, which is also the highest fraction tested by Bartlett et al.[45] We note that Jeong et al.[48] made LM nanodroplet−PDMS composites with ϕ up to 0.66; however, these samples were, comparatively, very brittle. In our own attempts to go higher than ϕ = 0.5, the samples became difficult to fabricate and handle. Additionally, because copper is the most thermally conductive constituent of our three-phase composites, we used the highest practical fraction of the copper particles (i.e., 25% Cu, 25% LM, and 50% PDMS for the three-phase composites). We found that higher than 25% Cu was difficult to fully manually premix into the LM.

DOI: 10.1021/acsami.7b15814
ACS Appl. Mater. Interfaces 2018, 10, 2083−2092

The casting mold consists of top and bottom silicon wafers with glass slide spacers that determine the sample thickness (see Figure 1b). To maintain contact between the silicon wafers and the glass spacers, which will ensure a constant thickness throughout the sample, we placed two 200 g weights on top of the mold assembly for the duration of the cure. All samples in this work were about 2 mm thick prior to compression during the thermal transport measurement. All samples were cured in an oven (Fisher Scientific Isotemp 280A) at 100 °C for 2 h.

We used two approaches to combine the LM and Cu additives with the PDMS matrix. We either sequentially mixed the additives into PDMS (LM followed by Cu) or premixed the LM and Cu together prior to dispersing them in PDMS, as illustrated in Figure 1a. The sequential additive mixing method results in predominantly isolated microfillers with minimal LM−Cu interactions. Conversely, the additive premixing method ensures maximal interaction between the LM and Cu. This method produces initially heterogeneous LM−Cu particles that spontaneously alloy into $CuGa_2$ over time and in situ.

2.2. Composite Characterization. We imaged the morphology of the composites using high-magnification optical microscopy (Zeiss Axio Zoom.V16) with an objective lens of 2.3×/0.57 FWD and 10.6 mm focal length (Zeiss PlanNeoFluar Z) as well as scanning electron microscopy (SEM) (Amray 1910 with field emission gun). Because of the microscopic size of the particles and ease of their differentiation through color, optical imaging of the polymer composites proved to be much more insightful than SEM images. Consequently, we present optical images of the polymer composite samples. For characterization of solidified LM−Cu alloy cross sections, which were mirror-polished using standard procedures,[49] we utilized SEM imaging as well as energy-dispersive X-ray (EDS) mapping (performed with electron beam energy of 15 keV and spot setting of −15 using an EDAX Apollo detector with Genesis software). X-ray diffraction (XRD) was performed using a PANalytical X'Pert PRO MRD with a Cu Kα X-ray source operating at 40 kV and 40 mA.

We used two image processing methods to quantify the extent of filler dispersion in the samples. For the samples with microdispersed spheroidlike fillers, we calculated an equivalent diameter, D_{EQ}, to evaluate particle size such that

$$D_{EQ} = \sqrt{\frac{4A_p}{\pi}} \tag{1}$$

where A_p is the area of the particles as identified with ImageJ. For the samples with strongly polydispersed LM−Cu fillers, however, determination of an equivalent diameter was not representative because of the highly random nature of the filler shapes. Consequently, for these samples, we report the particle area distribution (PAD). Furthermore, because the PAD is highly non-Gaussian (a large number of particles with small areas and a few particles with very large areas), we present the PAD in cumulative terms. Specifically, the cumulative particle area distribution corresponds to the summation of the particle areas, sorted from the smallest to the largest, up to a given area value. The distribution is normalized by the total cumulative area. As a representative measure of the cumulative particle area, we used the 50 percentile (referred to as $PAD_{50\%}$). For each sample, we analyzed 8−10 images of the surface at various locations and separated filler from matrix through manual thresholding.

We measured the thermal resistance of the samples using a stepped-bar apparatus (SBA),[50,51] which is based on the ASTM D5470 standard[52] for measuring the thermal resistance of thin materials. Our custom SBA includes a linear encoder and a load cell that measure sample thickness and pressure, respectively, during thermal resistance measurements. Figure S1a in the Supporting Information illustrates the measurement principle of the ASTM D5470 method. Measuring thermal conductivity fundamentally requires applying a known heat flux to a sample of known geometry and then measuring the temperature drop across the sample. In this method, a steady-state temperature gradient across the sample is created using a heat source and a heat sink. The sample is placed between two metallic reference bars of known cross-sectional area and thermal conductivity. To minimize errors from misalignment, the top bar has a larger cross section than that of the bottom bar.[50] The temperature distribution in the reference bars (measured via thermocouples in precision-machined holes along the reference bar lengths) is then used to measure the heat flux, q, in the bars. Because the system is well insulated, the measured heat flow through the bars is equal to the measured heat flow through the sample. Extrapolating the temperature distributions of the reference bars to the bar−sample interfaces allows the temperature drop across the sample, ΔT, to be determined. The measured thermal resistance, R_{th}, across the sample is then obtained with

$$R_{th} = \frac{\Delta T}{q} \tag{2}$$

This thermal resistance represents the summation of the sample's intrinsic thermal resistance, R_s, as well as the thermal contact resistance, R_c, between the sample and the reference bars (note that R_c is the sum of two contact resistances, the contact resistance between the top reference bar and the top of the sample, and the contact resistance between the bottom reference bar and the bottom of the sample). The samples are under pressure during thermal resistance measurements to minimize R_c, which will bring k_{eff} closer to the true k of the composite. Various loads are used to gauge sample properties, but the target pressure for the results of this study is 1.5 MPa, which is near the high end of the pressure range applicable to electronic cooling.[32]

The measured thermal resistances, R_{th}, can be converted into intrinsic thermal conductivity values if the sample thickness, t_c, and the sample contact resistance, R_c, are known. We obtained the sample thickness during our measurements via the linear encoder that is integrated into our stepped-bar apparatus thermal transport measurement system. We also estimated R_c of our samples by measuring the thermal resistance of several samples with varying thicknesses and extrapolating to zero thickness. We estimate the values for R_c to be approximately 1.2×10^{-4} and 8×10^{-5} m^2 K W^{-1} at 1.5 MPa for well-dispersed samples and less-dispersed samples, respectively. The single-side contact resistance, $R_c/2$, (4×10^{-5} m^2 K W^{-1}) is comparable to that of Si−Al interfaces at the same pressure (2×10^{-5} m^2 K W^{-1}).[53] With R_{th} and t_c known, the effective thermal conductivity can be calculated by

$$k_{eff} = \frac{t_c}{R_{th}} = \frac{t_c}{R_c + R_s} \tag{3}$$

This effective thermal conductivity includes the combined effects of the intrinsic sample resistance and the sample contact resistance. Consequently, the effective thermal conductivity is smaller than the intrinsic sample thermal conductivity. However, strictly speaking, we cannot describe our samples with a single intrinsic thermal conductivity value because many of our samples are heterogeneous with large inclusions of several hundred microns in size. Consequently, we describe them with an effective intrinsic thermal conductivity, $\bar{k}$, of the composite, which can be calculated via the following equation

$$\bar{k} = \frac{t_c}{R_{th} - R_c} \tag{4}$$

Because of the Mullins effect of PDMS,[54] which results in a change or relaxation of the modulus between the first and second loadings, each sample is measured only once and only with increasing pressure. We estimate that the overall measurement uncertainty in k_{eff} ranges from 4 to 6% (68% confidence). Additional uncertainty arises as the thermal conductivities of the sample and reference bars become more similar, and this corresponds to the higher end of the previously mentioned uncertainty range. We validated our thermal conductivity measurements against literature results on PDMS−liquid metal composites[45,48] (see Figure S1b in the Support Information). Our measured PDMS thermal conductivity of 0.27 ± 0.01 W m^{-1} K^{-1} also

DOI: 10.1021/acsami.7b15814
ACS Appl. Mater. Interfaces 2018, 10, 2083−2092

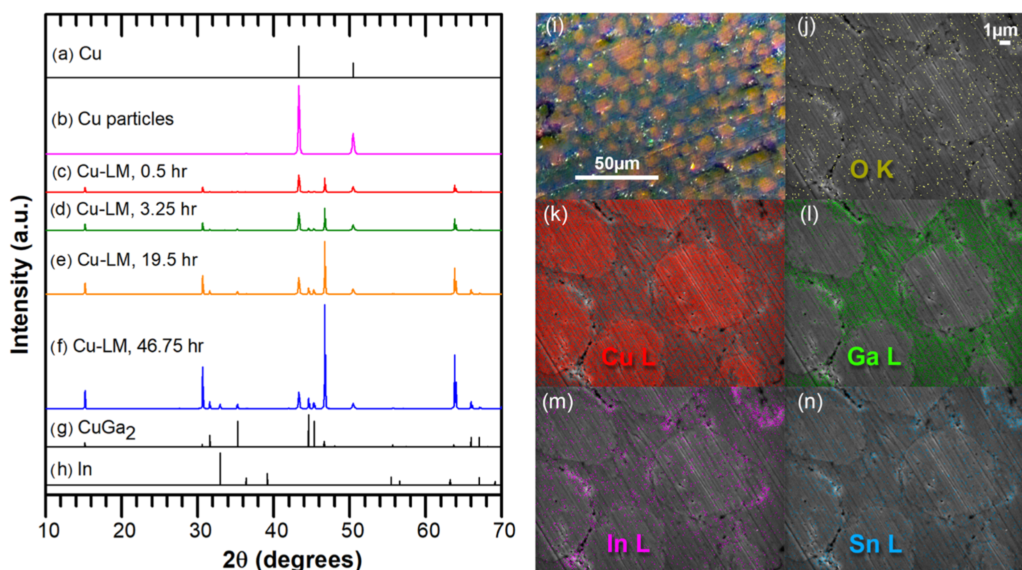

Figure 2. X-ray diffraction patterns of (a) Cu powder diffraction file 00-004-0836; (b) as-received Cu microparticles; LM−Cu mixtures (50:50 ratio) at (c) 0.5 h, (d) 3.25 h, (e) 19.5 h, and (f) 46.75 h after mixing; (g) $CuGa_2$ powder diffraction file 00-025-0275; and (h) In powder diffraction file 00-005-0642. An optical image (i) and a SEM image along with energy-dispersive X-ray spectroscopy (EDS) elemental maps (j−n) of a mirror-polished cross section of Cu particles mixed in LM at a 1:1 ratio 5 months after mixing.

matches well with the thermal conductivity stated by the manufacturer (Sylgard 184), 0.27 W m^{-1} K^{-1}.[55]

We also conducted a limited set of mechanical measurements. Specifically, we performed compressive relaxation tests on an INSTRON 5969 mechanical tester. Composites with large LM−Cu colloids have comparable properties to those of composites with 10 μm copper particles embedded in the PDMS matrix. Further details of the procedure and results of the mechanical tests can be found in the Supporting Information.

3. RESULTS AND DISCUSSION

3.1. LM−Cu Colloid and Alloy Characterization. Prior to discussing thermal properties of the polymer composites, we first discuss our material characterization of the LM−Cu colloid and $CuGa_2$ formation. Formation of the latter compound is thermodynamically favorable at room temperature, as illustrated in the Cu−Ga phase diagram,[56,57] and likely kinetically facilitated by the liquid state of the Ga in the LM. Indeed, X-ray diffraction (XRD) spectra presented in Figure 2 directly confirm $CuGa_2$ formation. In fact, Figure 2c shows that $CuGa_2$ diffraction peaks can be observed in as little as 30 min after mixing the Cu and LM together. Continual formation of $CuGa_2$ is also observed as the intensity ratio of the $CuGa_2$ peaks relative to the Cu peaks increases over time (Figure 2c−f). Extraction of Ga from the LM is also indirectly observed via the appearance of an In diffraction peak at 33.0° at 46.75 h (Figure 2f). This diffraction peak indicates the formation of crystalline In, which results due to LM solidification (i.e., extracting Ga from the LM changes the LM elemental composition and increases the melting temperature to above room temperature). Although this in situ alloying process is favorable from the perspective of immobilizing Ga and preventing damage to neighboring IC components, it also limits the time frame for shaping and molding the composites.[58] Markedly, mixing LM and Cu particles at a 1:1 ratio exhibits notable signs of hardening from $CuGa_2$ formation in under an hour, as observed in this study and by Hong and Suryanarayana.[59]

Because we are using a 50:50 ratio of Cu/LM, excess Cu remains after the formation of $CuGa_2$. This is evidenced by the presence of both Cu and $CuGa_2$ peaks in the XRD patterns. The In content in the LM is also revealed via the formation of the diffraction peak at 33.0° (Figure 2f). The presence of Sn in the LM is not directly detected by our XRD. This suggests that the Sn signal is too weak (the Sn content in our Cu/LM composite is just ∼3.5 atom %) or that Sn has dissolved/alloyed into one of the other metallic phases. Note that the colocation of Sn and In in the SEM EDS mapping (Figure 2m,n) suggests that Sn may have alloyed with the In phase; however, more precise characterization is needed to definitely confirm this hypothesis.

We used optical and SEM imaging as well as EDS mapping of the mirror-polished LM−Cu colloid cross section after full alloying occurred to evaluate the spatial distribution of $CuGa_2$ when Cu particles are mixed into LM at a 50:50 ratio. The results shown in Figure 2i−n clearly show that, at a 50:50 LM-to-Cu mixing ratio, the colloid alloys into a $CuGa_2$ matrix with the In, Sn, and O content surrounding Cu microparticles. Specifically, contrasting Cu and Ga distributions in Figure 2k,l indicates that Cu is mixing with the LM to form $CuGa_2$ in the space between pure Cu particles.

It is also important to acknowledge the effect of gallium oxide on the fabrication and performance of these composites. The LM−Cu colloids and all composites in this study were made in the presence of air, without any attempt to prevent LM oxidation. Gallium oxide forms readily on the surface of gallium-based LMs when exposed to even trace amount of oxygen and changes three main properties of the LM: viscosity, thermal conductivity, and wetting properties.[15,60,61] Specifically, when gallium oxide is present in the LM, the thermal conductivity of the resulting colloid (LM−solid oxide) is significantly decreased,[14,15,19] the viscosity significantly increased,[19,62] and the wetting properties are generally improved.[11,14,63,64] However, Li et al.[15] demonstrated that when Cu particles at ϕ_{Cu} = 0.07 are added to LM in the presence of oxygen (i.e., with oxide formation), the effective

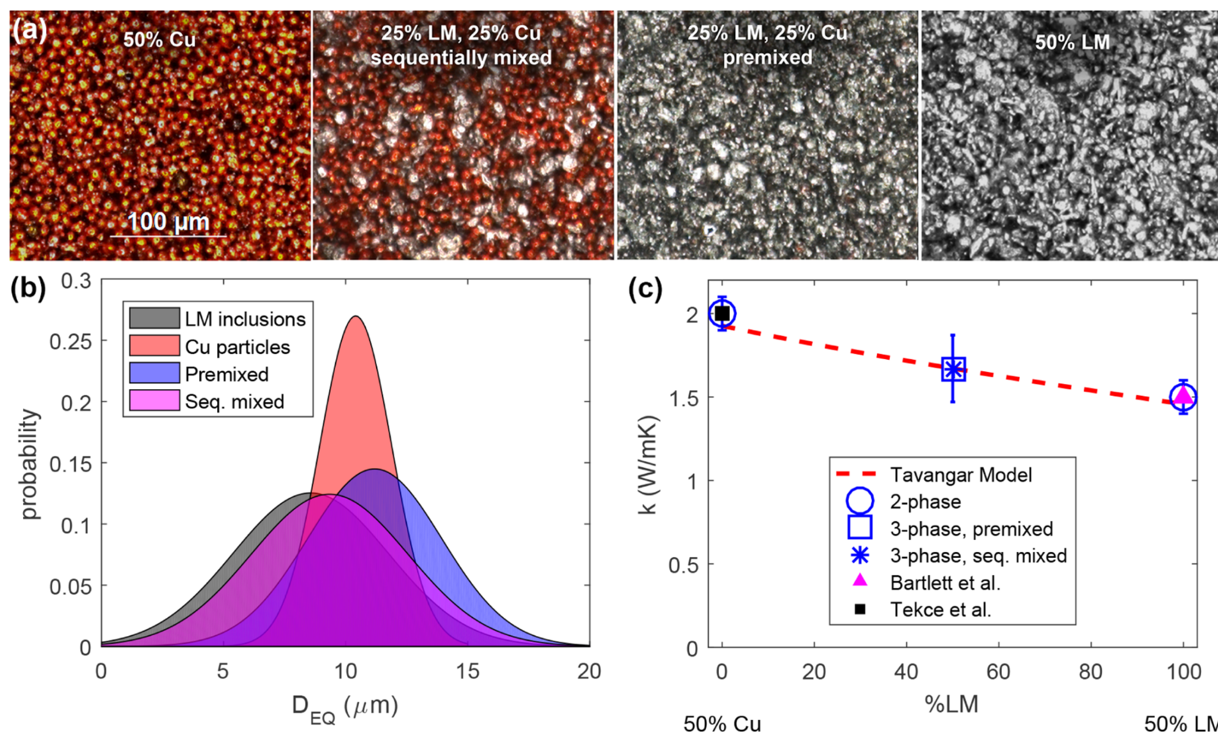

Figure 3. (a) Optical images of Cu-only PDMS, sequentially mixed LM−Cu−PDMS, premixed LM−Cu−PDMS, and LM-only PDMS composites at $\phi = 0.5$ with comparable inclusion size distributions, (b) plot of the particle size distributions where D_{EQ} is the equivalent diameter based on the particle and inclusion areas from image particle analysis, and (c) plots of the measured and theoretically predicted two-component and three-component composite thermal conductivities including literature data from Bartlett et al.[45] and Tekce et al.[68]

thermal conductivity of the colloid (LM with solid oxide and Cu which alloys into $CuGa_2$) is near that of pure LM. Taking into account that we use $\phi_{Cu} = 0.5$ in the LM colloid, the effect of oxide on the resulting thermal properties should be negligible. The Cu particles are likely well wetted by LM predominantly due to reactive wetting (via in situ alloying),[65] and not only by oxide formation. The oxide, however, forms on the surface of the colloid during blending into PDMS and likely facilitates the dispersion process.[61] It is also worth noting that, despite being only 1−2 nm thick, the oxide shell is strong enough to support free-standing LM structures[66] and even internal LM flow in pipes made out of oxide shells.[67] However, its presence is unlikely to have a major impact on mechanical properties of the three-phase composites once the alloying (i.e., solidification of the colloid) process occurs.

3.2. Thermal Properties of Composites with Microdispersed Fillers. We first evaluated the thermal properties of three-component composites with inclusion size distribution comparable to that of two-component Cu-only and LM-only composites. The images in Figure 3a show that the manual blending process can produce uniformly microdispersed Cu-only, LM-only, sequentially mixed LM−Cu, and premixed LM−Cu filler in the PDMS matrix. The particle size probability distribution plots in Figure 3b show that the manual blending process can produce LM microdroplets with $D_{EQ} = 8.6 \pm 3.2$ μm (68% confidence interval) and LM−Cu particles with $D_{EQ} = 11.2 \pm 2.8$ μm (for premixed) and 9.3 ± 3.2 μm (for sequentially mixed) close to that of the Cu particles ($D_{EQ} = 10.5 \pm 1.5$ μm). These probability distributions are fit from particle size distributions of the well-dispersed samples, assuming normal distributions (see Figure S2 in the Support Information). Because the particle distributions are similar in average size, the difference in the thermal conductivity of the composites should theoretically be predominantly determined by the thermal properties of the constituents and their volume fractions.

To predict the thermal conductivity of our composites, we start with the model as described by Tavangar[69] and add in a shape factor, L, to adjust for ellipsoidal LM inclusions when under load. The Tavangar model is a differential effective medium (DEM) scheme that accounts for interface thermal resistance between particles and the matrix and is fairly accurate at high-volume-fraction filler.[69,70] The Tavangar model is given as

$$1 - \phi = \frac{(k_m)^L (k_p k_c R_b + a k_c - a k_p)}{(k_c)^L (k_p k_m R_b + a k_m - a k_p)} \qquad (5)$$

where L is the shape factor and is equal to 1/3 when the filler particles are spherical, k_p is the thermal conductivity of the particles or inclusions, k_m is the thermal conductivity of the matrix, k_c is the thermal conductivity of the composite, R_b is the interface thermal resistance, a is the radius of the particles (see the Supporting Information for the values of our specific inputs into the Tavangar model). Because the Tavangar model considers only composites with two components, we sequentially applied the Tavangar model for our composites with three components. More specifically, for our composites with PDMS, Cu, and LM, we first used the Tavangar model to calculate the thermal conductivity of a composite consisting of LM particles in a PDMS matrix, $k_{LM-PDMS}$. We then considered a composite consisting of Cu particles in a matrix and used $k_{LM-PDMS}$ as the matrix thermal conductivity, k_m, to yield the overall thermal conductivity of a Cu−LM−PDMS composite. Calculating k_c by adding LM into a Cu−PDMS matrix results in the same value as that obtained on adding Cu into a LM−

DOI: 10.1021/acsami.7b15814
ACS Appl. Mater. Interfaces 2018, 10, 2083−2092

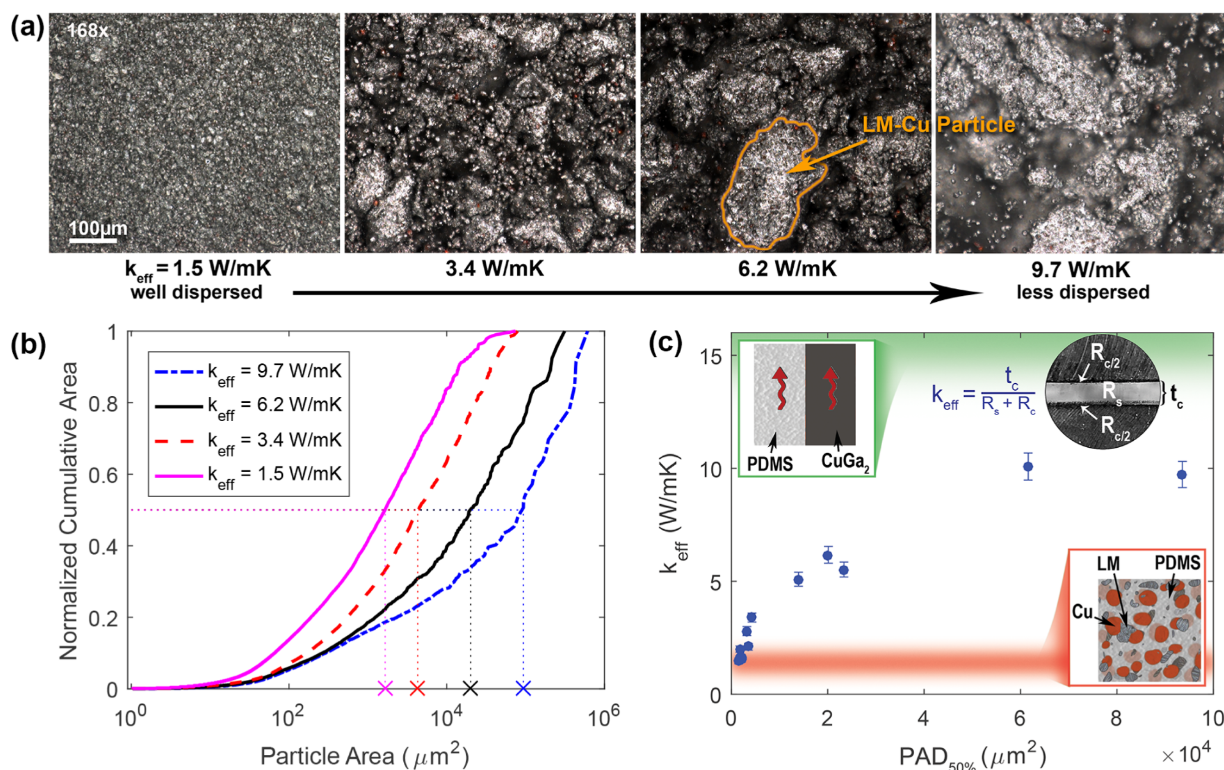

Figure 4. Premixed Cu–LM–PDMS composite structure–property–process results: (a) optical images of composites at 25% Cu, 25% LM, and 50% PDMS going from uniformly microdispersed on the left to highly polydispersed on the right, with their respective effective thermal conductivities; (b) normalized cumulative area distributions with indication of the 50th percentile ($PAD_{50\%}$) utilized to characterize each distribution; (c) effective thermal conductivity against the $PAD_{50\%}$ along with theoretical upper (green) and lower (red) bounds based on filler dispersion: from a block of $CuGa_2$ in parallel to a block of PDMS to microdispersed LM + Cu in PDMS.

PDMS matrix, but the latter sequence is used because it is the sequence whereby the actual samples are made.

Figure 3c shows measured and theoretically predicted values of k_c for the two-component and three-component composites as the ratio of LM to Cu is varied and ϕ is held constant at 0.5 (i.e., 50% PDMS and the other 50% is a ratio of LM and Cu). As predicted, the three-component composites have thermal conductivities in between 2.0 ± 0.1 W m^{-1} K^{-1} for the Cu-only PDMS composite and 1.5 ± 0.1 W m^{-1} K^{-1} for the LM-only PDMS composite. Specifically, the sequentially mixed and premixed LM–Cu–PDMS composites both have thermal conductivities of 1.65 ± 0.15 W m^{-1} K^{-1}. All of the measured composite thermal conductivities with well-dispersed fillers are about an order of magnitude higher than those of the matrix material (0.27 ± 0.01 W m^{-1} K^{-1}) and are comparable to previously described results.[45,68] These results demonstrate that increasing the thermal conductivity of the filler particles has diminishing returns. In particular, a 14-fold change in the thermal conductivity of the filler from 28 W m^{-1} K^{-1} for LM to 400 W m^{-1} K^{-1} for Cu results in only about a 1.3-fold increase in the thermal conductivity of the composite. Thus, substantial thermal conductivity enhancements can only be achieved by increasing the polymer thermal conductivity and/or improving the interfacial thermal transport (i.e., decreasing the number of interfaces and/or decreasing the thermal interface resistance).

3.3. Thermal Properties of Premixed Three-Phase Composites.

Premixing the Cu particles into bulk LM provides a unique opportunity to enhance the composite thermal conductivity by decreasing the number of filler–PDMS boundaries via different levels of the LM–Cu colloid dispersion. Figure 4a shows that, by adjusting the manual blending time of the LM–Cu colloid into PDMS, we achieved dramatically different morphologies of the inclusions. In particular, decreasing the mixing time from 300 s (used for the microdispersed composites) to ~20–30 s results in a broad particle distribution with feature sizes ranging from a few microns to hundreds of microns. To quantify the filler dispersion in these samples, we used image processing to evaluate the particle cluster area distributions as described in Section 2.2. Figure 4b shows the normalized cumulative cluster area distributions corresponding to the example sample images in Figure 4a. In turn, Figure 4c presents the effective thermal conductivities of premixed LM–Cu–PDMS composites against their 50th percentile normalized cumulative cluster area distribution achieved through varied mixing times (see Section 2.2 for the reasoning behind the use of this distribution characteristic). These results demonstrate that retaining large fill structures within the matrix enhances thermal performance up to an effective thermal conductivity of 10 ± 0.6 W m^{-1} K^{-1} (or an effective intrinsic thermal conductivity of $\bar{k} \approx 17 \pm 3$ W m^{-1} K^{-1} if R_c is accounted for; see Figure S3 in the Supporting Information). One limitation to this work is that, although samples with such high thermal conductivity were repeatedly fabricated, it is difficult to fabricate them consistently because of variability associated with the short manual mixing time (we frequently observed a $k_{eff} \approx 4–8$ W m^{-1} K^{-1} for a short mixing time). These inconsistencies could be resolved by replacing the simple mortar and pestle mixing method outlined by Fassler et al.[46] and Bartlett et al.[45] with an alternate automated process.

DOI: 10.1021/acsami.7b15814
ACS Appl. Mater. Interfaces 2018, 10, 2083–2092

All of the thermal conductivity data in Figure 4c falls between the lower bound of uniformly microdispersed particles ($k_{eff} \approx 2$ W m^{-1} K^{-1}) and the upper bound of a two-part composite with 50% PDMS and 50% $CuGa_2$ ($k = 98$ W m^{-1} K^{-1})[71] blocks arranged in parallel ($k_{eff} \approx 16$ W m^{-1} K^{-1}, accounting for R_c of the same magnitude seen with our samples), as shown in the top left of Figure 4c.

We hypothesize that the thermal conductivity increase stems from two key factors: (i) the small thermal interface resistance of metal−metal interfaces with respect to that of the polymer−metal interfaces and (ii) the increased likelihood of percolation for large colloids relative to that for small colloids (i.e., the polydispersed colloids and well-dispersed colloids in this work, respectively). A review of the literature reveals that typical polymer−metal interfaces have thermal interface resistances of 10^{-6}−10^{-7} m^2 K W^{-1}, whereas typical metal−metal interfaces are several orders of magnitude lower (e.g., 2.5×10^{-10} m^2 K W^{-1} for an Al−Cu interface).[36,37,72] Consequently, we expect thermal transport through our $CuGa_2$−Cu interfaces to be orders of magnitude better than the transport through polymer−$CuGa_2$ or polymer−Cu interfaces.

It is also useful to analyze these numbers in the context of Kapitza lengths, L_K = TBR× k_{ref}, where L_K, TBR, and k_{ref} are the Kapitza length, thermal boundary resistance, and reference thermal conductivity, respectively.[73] The Kapitza length relates the thermal boundary resistance to an equivalent slab of material with a thickness and thermal conductivity equivalent to L_K and k_{ref}. For example, a typical polymer−metal interface with TBR = 1×10^{-7} m^2 K W^{-1} poses a resistance equivalent to about 10 μm of $CuGa_2$ ($k_{CuGa_2} = 98$ W m^{-1} K^{-1}).[71] This value is significant because it is comparable to the 10 μm diameter of our well-dispersed particles (Figure 3b). Furthermore, considering that each particle has two heat transfer interfaces (i.e., going into and leaving the particle), thermal transport through the filler particles is bottlenecked by thermal transport through the polymer−particle interface. Relative to a polymer−metal interface, a typical metal−metal interface with TBR = 1×10^{-10} m^2 K W^{-1} poses a resistance equivalent to ∼0.01 μm of $CuGa_2$, which is negligibly small. This means that the internal Cu−$CuGa_2$ interfaces within our large LM−Cu colloids can be ignored and that these large colloids can be thought as large single particles with thermal conductivities on the order of 10^2 W m^{-1} K^{-1}. This high thermal conductivity should also allow these large particles to effectively short circuit around the low-thermal-conductivity PDMS ($k_{PDMS} = 0.27$ W m^{-1} K^{-1}).

We also hypothesize that the larger size of our polydispersed colloids with respect to that of our well-dispersed colloids (i.e., characteristic lengths of ∼100 and ∼ 10 μm, respectively) also plays a key role with respect to increased thermal conductivity. The classical percolation theory focuses on the probability of forming an infinite network in an infinite lattice. Naturally, such conditions are never perfectly achieved in the lab. Percolation studies on finite systems have shown that the percolation threshold decreases as a system becomes more finite.[74] This suggests that our larger colloids should more easily percolate than our smaller colloids. This is intuitive given our sample thickness, large colloid effective diameter, and small colloid effective diameter of ∼2 mm, ∼100 μm, and ∼ 10 μm, respectively. To a first approximation, percolation for our large colloids is a 20-body interaction and should be significantly more common than percolation for our small colloids, which is a 200-body interaction. Moreover, the thermal conductivity of the large colloid samples should also be improved because the thermal conductance for a percolating thread formed by ∼100 μm particles should be significantly larger than the thermal conductance for a percolating thread formed by ∼10 μm particles.

3.4. Ga Leakage and Corrosion Issues. Another benefit of the in situ $CuGa_2$ formation is that it immobilizes Ga, preventing any liquid leakage and associated corrosion of surrounding metals. This characteristic makes our composites safe to use with aluminum heat sinks and other metal components. Figure 5 shows a premixed composite sample pad

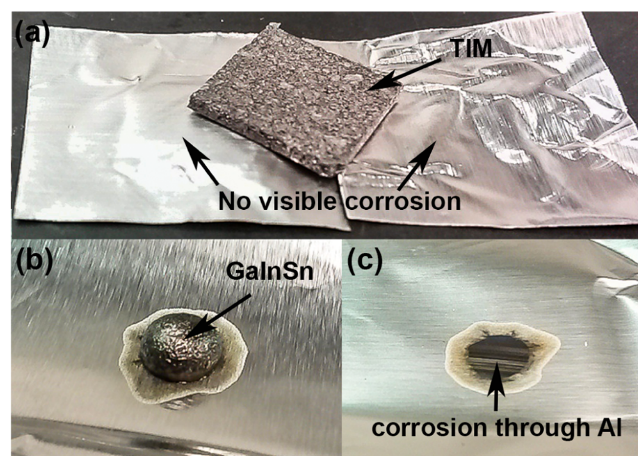

Figure 5. (a) 25% LM, 25% Cu, 50% PDMS sample made using the premixed method after being sandwiched between aluminum foil at 55 °C and 3 MPa for 40 h, (b) GaInSn on aluminum foil after 24 h at room temperature, and (c) the hole it corroded through the aluminum.

after 40 h of being sandwiched between aluminum foil at 55 °C and 3 MPa (a) next to aluminum foil that was exposed to a drop of LM at room temperature for 24 h with no applied pressure (b, c). No macroscopic corrosion of the aluminum foil occurs with the premixed composite samples. Furthermore, to demonstrate that our samples can be applied with LM−Cu in the colloidal state, we cured a three-component sample in between two pieces of aluminum foil for 2 h at 100 °C (see Supporting Information). As in the previous case, we did not observe any evidence of corrosion of the aluminum foil. These results indicate that the affinity of Ga to Cu is sufficient to prevent Ga from leaching from the polymer and reacting with Al. Thus, the three-component composites should be safe to cure in place next to aluminum components.

4. CONCLUSIONS

Our work demonstrates that gallium-based LMs have a great potential as filler in polymer TIMs once their leakage, and associated degradation of nearby components, is resolved. We showed that adding Cu particles as a third component to LM−polymer composites improves the chemical stability and effective thermal conductivity of the material over either two-component counterparts. The addition of Cu eliminates LM leakage from the composite via in situ $CuGa_2$ formation as well as by displacing the overall content of LM needed to achieve enhanced thermal conductivity. The formation of $CuGa_2$ is sufficiently slow to cast or mold this composite into any desired shape or void but fast enough to inhibit leaching of

DOI: 10.1021/acsami.7b15814
ACS Appl. Mater. Interfaces 2018, 10, 2083−2092

Ga to surrounding metals during the molding process. We note that, if found necessary, the rate of $CuGa_2$ formation could be altered through change of the sample processing temperature. Prevention of Ga leaching makes these composites safe to use with aluminum IC components.

Synergistically, the LM helps to glue or solder the Cu particles together forming LM−Cu colloids. The precoating of the Cu particles with LM facilitates the formation of large highly conductive filler structures that can more readily percolate and thermally short circuit through the polymer matrix. This leads to effective intrinsic thermal conductivity of up to 17 W m^{-1} K^{-1} ($k_{eff} \approx 10$ W m^{-1} K^{-1}) and represents a 10-fold improvement over the microdispersed composites with the same filler ratio and a 70-fold improvement over the polymer matrix itself.

■ ASSOCIATED CONTENT

Supporting Information

The Supporting Information is available free of charge on the ACS Publications website at DOI: 10.1021/acsami.7b15814.

Details of measurement and characterization techniques (PDF)

■ AUTHOR INFORMATION

Corresponding Authors

*E-mail: rywang@asu.edu (R.Y.W.).
*E-mail: konradr@asu.edu (K.R.).

ORCID

Konrad Rykaczewski: 0000-0002-5801-7177

Author Contributions

The manuscript was written through contributions of all authors. All authors have given approval to the final version of the manuscript.

Funding

M.I.R. acknowledges support through ASU's Fulton Schools of Engineering Dean's Fellowship. K.R. acknowledges startup funds from Fulton Schools of Engineering at ASU. P.B.V. and R.Y.W. acknowledge support from the National Science Foundation through award number DMR-1506829.

Notes

The authors declare no competing financial interest.

■ ACKNOWLEDGMENTS

We gratefully acknowledge the use of the facilities within the LeRoy Eyring Center for Solid State Science at Arizona State University.

■ REFERENCES

(1) Moore, A. L.; Shi, L. Emerging Challenges and Materials for Thermal Management of Electronics. *Mater. Today* **2014**, *17*, 163−174.

(2) *2015 International Technology Roadmap for Semiconductors (ITRS)*; Semiconductor Industry Association, 2015.

(3) Intel. Intel Xeon Processor E5-2695 v4. http://ark.intel.com/products/91316/Intel-Xeon-Processor-E5-2695-v4-45M-Cache-2_10-GHz.

(4) Ferain, I.; Colinge, C. A.; Colinge, J.-P. Multigate Transistors as the Future of Classical Metal−oxide−semiconductor Field-Effect Transistors. *Nature* **2011**, *479*, 310−316.

(5) Zhang, R.; Cai, J.; Wang, Q.; Li, J.; Hu, Y.; Du, H.; Li, L. Thermal Resistance Analysis of Sn-Bi Solder Paste Used as Thermal Interface Material for Power Electronics Applications. *J. Electron. Packag.* **2014**, *136*, No. 011012.

(6) Chung, D. D. Materials for Thermal Conduction. *Appl. Therm. Eng.* **2001**, *21*, 1593−1605.

(7) Blazej, D. Thermal Interface Materials. *Electron. Cool.* **2003**, *9*, 14−21.

(8) Bar-Cohen, A.; Matin, K.; Narumanchi, S. Nanothermal Interface Materials: Technology Review and Recent Results. *J. Electron. Packag.* **2015**, *137*, No. 040803.

(9) Hamdan, A.; McLanahan, A.; Richards, R.; Richards, C. Characterization of a Liquid−metal Microdroplet Thermal Interface Material. *Exp. Therm. Fluid Sci.* **2011**, *35*, 1250−1254.

(10) Directive 2011/65/EU of the European Parliament and the Council of 8 June 11 on the Restriction of the Use of Certain Hazardous Substances in Electrical and Electronic Equipment. *Off. J. Eur. Union* **2011**, *54* 88.

(11) Gao, Y.; Liu, J. Gallium-Based Thermal Interface Material with High Compliance and Wettability. *Appl. Phys. A* **2012**, *107*, 701−708.

(12) Roy, C. K.; Bhavnani, S.; Hamilton, M. C.; Johnson, R. W.; Knight, R. W.; Harris, D. K. Thermal Performance of Low Melting Temperature Alloys at the Interface between Dissimilar Materials. *Appl. Therm. Eng.* **2016**, *99*, 72−79.

(13) Roy, C. K.; Bhavnani, S.; Hamilton, M. C.; Johnson, R. W.; Knight, R. W.; Harris, D. K. Accelerated Aging and Thermal Cycling of Low Melting Temperature Alloys as Wet Thermal Interface Materials. *Microelectron. Reliab.* **2015**, *55*, 2698−2704.

(14) Gao, Y.; Wang, X.; Liu, J.; Fang, Q. Investigation on the Optimized Binary and Ternary Gallium Alloy as Thermal Interface Materials. *J. Electron. Packag.* **2016**, *139*, No. 011002.

(15) Li, G.; Ji, Y.; Wu, M.; Ma, H. In *Highly Conductive Thermal Paste of Liquid Metal Alloy Dispersed with Copper Particles*, Proceedings of the ASME 2016 Heat Transfer Summer Conference; American Society of Mechanical Engineers: Washington, DC, 2016.

(16) Plevachuk, Y.; Sklyarchuk, V.; Eckert, S.; Gerbeth, G.; Novakovic, R. Thermophysical Properties of the Liquid Ga−In−Sn Eutectic Alloy. *J. Chem. Eng. Data* **2014**, *59*, 757−763.

(17) Wilcox, M.; Ghoshal, U.; Grimm, D.; Ibrani, S.; Feicht, D.; Miner, A. High-performance liquid metal cooling loops. In *Semiconductor Thermal Measurement and Management Symposium*, 2005 IEEE Twenty First Annual IEEE; pp 19−19.

(18) Geratherm Medical AG. Safety Data Sheet for Galinstan fluid. http://www.rgmd.com/msds/msds.pdf (accessed Oct 6, 2017).

(19) Mei, S.; Gao, Y.; Deng, Z.; Liu, J. Thermally Conductive and Highly Electrically Resistive Grease Through Homogeneously Dispersing Liquid Metal Droplets Inside Methyl Silicone Oil. *J. Electron. Packag.* **2014**, *136*, No. 011009.

(20) Lyon, R. N. *Liquid Metals Handbook, The Committee on the Basic Properties of Liquid Metals*; Off. Nav. Res. Dep. Navy, 1952.

(21) Rajagopalan, M.; Bhatia, M. A.; Tschopp, M. A.; Srolovitz, D. J.; Solanki, K. N. Atomic-Scale Analysis of Liquid-Gallium Embrittlement of Aluminum Grain Boundaries. *Acta Mater.* **2014**, *73*, 312−325.

(22) Deng, Y. G.; Liu, J. Corrosion Development between Liquid Gallium and Four Typical Metal Substrates Used in Chip Cooling Device. *Appl. Phys. A: Mater. Sci. Process.* **2009**, *95*, 907−915.

(23) Ndieguene, A.; Albert, P.; Fortin, C.; Oberson, V.; Sylvestre, J. In *Eternal Packages: Liquid Metal Flip Chip Devices*, 2016 IEEE 66th Electronic Components and Technology Conference 2016; pp 580−587.

(24) Han, Z.; Fina, A. Thermal Conductivity of Carbon Nanotubes and Their Polymer Nanocomposites: A Review. *Prog. Polym. Sci.* **2011**, *36*, 914−944.

(25) Saba, N.; Tahir, P. M.; Jawaid, M. A Review on Potentiality of Nano Filler/natural Fiber Filled Polymer Hybrid Composites. *Polymers* **2014**, *6*, 2247−2273.

(26) Huang, X.; Jiang, P.; Tanaka, T. A Review of Dielectric Polymer Composites with High Thermal Conductivity. *IEEE Electr. Insul. Mag.* **2011**, *27*, 8−16.

(27) Sarvar, F.; Whalley, D.; Conway, P. In *Thermal Interface Materials - A Review of the State of the Art*, 2006 1st Electronics Systemintegration Technology Conference, 2006; Vol. 2, pp 1292−1302.
(28) Hussain, F.; Hojjati, M.; Okamoto, M.; Gorga, R. E. Review Article: Polymer-Matrix Nanocomposites, Processing, Manufacturing, and Application: An Overview. *J. Compos. Mater.* **2006**, *40*, 1511−1575.
(29) Ralphs, M. I. *Investigating the Effect of Carbon Nanotube Functionalization in Polydimethylsiloxane Composite through Use of a Stepped Bar Apparatus*; Utah State University, 2016.
(30) Suh, D.; Moon, C. M.; Kim, D.; Baik, S. Ultrahigh Thermal Conductivity of Interface Materials by Silver-Functionalized Carbon Nanotube Phonon Conduits. *Adv. Mater.* **2016**, *28*, 7220−7227.
(31) Seshadri, I.; Esquenazi, G. L.; Borca-Tasciuc, T.; Keblinski, P.; Ramanath, G. Multifold Increases in Thermal Conductivity of Polymer Nanocomposites through Microwave Welding of Metal Nanowire Fillers. *Adv. Mater. Interfaces* **2015**, *2*, No. 1500186.
(32) Prasher, R. In *Thermal Interface Materials: Historical Perspective, Status, and Future Directions*, Proceedings of the IEEE; IEEE, 2006; Vol. *94*, pp 1571−1586.
(33) McNamara, A. J.; Joshi, Y.; Zhang, Z. M. Characterization of Nanostructured Thermal Interface Materials–a Review. *Int. J. Therm. Sci.* **2012**, *62*, 2−11.
(34) Wang, S.; Cheng, Y.; Wang, R.; Sun, J.; Gao, L. Highly Thermal Conductive Copper Nanowire Composites with Ultralow Loading: Toward Applications as Thermal Interface Materials. *ACS Appl. Mater. Interfaces* **2014**, *6*, 6481−6486.
(35) Zhu, H.; Li, Y.; Fang, Z.; Xu, J.; Cao, F.; Wan, J.; Preston, C.; Yang, B.; Hu, L. Highly Thermally Conductive Papers with Percolative Layered Boron Nitride Nanosheets. *ACS Nano* **2014**, *8*, 3606−3613.
(36) Prasher, R. S.; Chiu, C.-P. Thermal Interface Materials. *Materials for Advanced Packaging*; Springer, 2017; pp 511−535.
(37) Rai, A.; Moore, A. L. Enhanced Thermal Conduction and Influence of Interfacial Resistance within Flexible High Aspect Ratio Copper Nanowire/polymer Composites. *Compos. Sci. Technol.* **2017**, *144*, 70−78.
(38) Fu, Y. X.; He, Z. X.; Mo, D. C.; Lu, S. S. Thermal Conductivity Enhancement with Different Fillers for Epoxy Resin Adhesives. *Appl. Therm. Eng.* **2014**, *66*, 493−498.
(39) Yim, M. J.; Li, Y.; Moon, K.; Paik, K. W.; Wong, C. P. Review of Recent Advances in Electrically Conductive Adhesive Materials and Technologies in Electronic Packaging. *J. Adhes. Sci. Technol.* **2008**, *22*, 1593−1630.
(40) Seshadri, I.; Esquenazi, G. L.; Cardinal, T.; Borca-Tasciuc, T.; Ramanath, G. Microwave Synthesis of Branched Silver Nanowires and Their Use as Fillers for High Thermal Conductivity Polymer Composites. *Nanotechnology* **2016**, *27*, No. 175601.
(41) Balachander, N.; Seshadri, I.; Mehta, R. J.; Schadler, L. S.; Borca-Tasciuc, T.; Keblinski, P.; Ramanath, G. Nanowire-Filled Polymer Composites with Ultrahigh Thermal Conductivity. *Appl. Phys. Lett.* **2013**, *102*, No. 093117.
(42) Xie, X. L.; Mai, Y. W.; Zhou, X. P. Dispersion and Alignment of Carbon Nanotubes in Polymer Matrix: A Review. *Mater. Sci. Eng., R* **2005**, *49*, 89−112.
(43) Taphouse, J. H.; Bougher, T. L.; Singh, V.; Abadi, P. P. S. S.; Graham, S.; Cola, B. A. Carbon Nanotube Thermal Interfaces Enhanced with Sprayed on Nanoscale Polymer Coatings. *Nanotechnology* **2013**, *24*, No. 105401.
(44) Marconnet, A. M.; Yamamoto, N.; Panzer, M. A.; Wardle, B. L.; Goodson, K. E. Thermal Conduction in Aligned Carbon Nanotube-Polymer Nanocomposites with High Packing Density. *ACS Nano* **2011**, *5*, 4818−4825.
(45) Bartlett, M. D.; Kazem, N.; Powell-palm, M. J.; Huang, X.; Sun, W.; Malen, J. A.; Majidi, C. High Thermal Conductivity in Soft Elastomers with Elongated Liquid Metal Inclusions. *Proc. Natl. Acad. Sci. U.S.A.* **2017**, *114*, 2143−2148.
(46) Fassler, A.; Majidi, C. Liquid-Phase Metal Inclusions for a Conductive Polymer Composite. *Adv. Mater.* **2015**, *27*, 1928−1932.
(47) Bartlett, M. D.; Fassler, A.; Kazem, N.; Markvicka, E. J.; Mandal, P.; Majidi, C. Stretchable, High-K Dielectric Elastomers through Liquid-Metal Inclusions. *Adv. Mater.* **2016**, *28*, 3726−3731.
(48) Jeong, S. H.; Chen, S.; Huo, J.; Gamstedt, E. K.; Liu, J.; Zhang, S.-L.; Zhang, Z.-B.; Hjort, K.; Wu, Z. Mechanically Stretchable and Electrically Insulating Thermal Elastomer Composite by Liquid Alloy Droplet Embedment. *Sci. Rep.* **2015**, *5*, No. 18257.
(49) Doudrick, K.; Chinn, J.; Williams, J.; Chawla, N.; Rykaczewski, K. Rapid Method for Testing Efficacy of Nano-Engineered Coatings for Mitigating Tin Whisker Growth. *Microelectron. Reliab.* **2015**, *55*, 832.
(50) Thompson, D. R.; Rao, S. R.; Cola, B. a. A Stepped-Bar Apparatus for Thermal Resistance Measurements. *J. Electron. Packag.* **2013**, *135*, No. 041002.
(51) Ralphs, M. I.; Smith, B. L.; Roberts, N. A. Technique for Direct Measurement of Thermal Conductivity of Elastomers and a Detailed Uncertainty Analysis. *Meas. Sci. Technol.* **2016**, *27*, No. 115014.
(52) ASTM D5470. *Standard Test Method for Thermal Transmission Properties of Thermally Conductive Electrically Insulating Materials*; ASTM International, 2006.
(53) Ohsone, Y.; Dryden, J.; et al. Optical Measurement of Thermal Contact Conductance between Wafer-like Thin Solid Samples. *J. Heat Transfer* **1999**, *121*, 954−963.
(54) Diani, J.; Fayolle, B.; Gilormini, P. A Review on the Mullins Effect. *Eur. Polym. J.* **2009**, *45*, 601−612.
(55) Dow Corning. Electronics Sylgard 184 Silicone Elastomer. *Product Datasheet* 2013; pp 1−3. http://www.dowcorning.com/DataFiles/090276fe80190b08.pdf (accessed Oct 10, 2017).
(56) Predel, B. *Cu-Ga (Copper Gallium)*; Springer, 1994.
(57) Li, J. B.; Ji, L. N.; Liang, J. K.; Zhang, Y.; Luo, J.; Li, C. R.; Rao, G. H. A Thermodynamic Assessment of the Copper-Gallium System. *Calphad* **2008**, *32*, 447−453.
(58) Tang, J.; Zhao, X.; Li, J.; Guo, R.; Zhou, Y.; Liu, J. Gallium-Based Liquid Metal Amalgams: Transitional-State Metallic Mixtures (TransM2ixes) with Enhanced and Tunable Electrical, Thermal, and Mechanical Properties. *ACS Appl. Mater. Interfaces* **2017**, *9*, 35977−35987.
(59) Hong, S. J.; Suryanarayana, C. Mechanism of Low-Temperature Cu Ga 2 Phase Formation in Cu-Ga Alloys by Mechanical Alloying. *J. Appl. Phys.* **2004**, *96*, 6120−6126.
(60) Dickey, M. D.; Chiechi, R. C.; Larsen, R. J.; Weiss, E. A.; Weitz, D. A.; Whitesides, G. M. Eutectic Gallium-Indium (EGaIn): A Liquid Metal Alloy for the Formation of Stable Structures in Microchannels at Room Temperature. *Adv. Funct. Mater.* **2008**, *18*, 1097−1104.
(61) Doudrick, K.; Liu, S.; Mutunga, E. M.; Klein, K. L.; Damle, V.; Varanasi, K. K.; Rykaczewski, K. Different Shades of Oxide: From Nanoscale Wetting Mechanisms to Contact Printing of Gallium-Based Liquid Metals. *Langmuir* **2014**, *30*, 6867.
(62) Scharmann, F.; Cherkashinin, G.; Breternitz, V.; Knedlik, C.; Hartung, G.; Weber, T.; Schaefer, J. A. Viscosity Effect on GaInSn Studied by XPS. *Surf. Interface Anal.* **2004**, *36*, 981−985.
(63) Liu, T.; Sen, P.; Kim, C. J. Characterization of Nontoxic Liquid-Metal Alloy Galinstan for Applications in Microdevices. *J. Microelectromech. Syst.* **2012**, *21*, 443−450.
(64) Kazem, N.; Hellebrekers, T.; Majidi, C. Soft Multifunctional Composites and Emulsions with Liquid Metals. *Adv. Mater.* **2017**, *29*, No. 1605985.
(65) Kramer, R. K.; Boley, J. W.; Stone, H. A.; Weaver, J. C.; Wood, R. J. Effect of Microtextured Surface Topography on the Wetting Behavior of Eutectic Gallium-Indium Alloys. *Langmuir* **2014**, *30*, 533−539.
(66) Dickey, M. D. Emerging Applications of Liquid Metals Featuring Surface Oxides. *ACS Appl. Mater. Interfaces* **2014**, *6*, 18369−18379.
(67) Liu, S.; Sun, X.; Kemme, N.; Damle, V. G.; Schott, C.; Herrmann, M.; Rykaczewski, K. Can Liquid Metal Flow in

Microchannels Made of Its Own Oxide Skin? *Microfluid. Nanofluid.* **2016**, *20*, 1−6.
(68) Tekce, H. S.; Kumlutas, D.; Tavman, I. H. Effect of Particle Shape on Thermal Conductivity of Copper Reinforced Polymer Composites. *J. Reinf. Plast. Compos.* **2007**, *26*, 113−121.
(69) Tavangar, R.; Molina, J. M.; Weber, L. Assessing Predictive Schemes for Thermal Conductivity against Diamond-Reinforced Silver Matrix Composites at Intermediate Phase Contrast. *Scr. Mater.* **2007**, *56*, 357−360.
(70) Pietrak, K.; Wisniewski, T. S. A Review of Models for Effective Thermal Conductivity of Composite Materials. *J. Power Technol.* **2015**, *95*, 14−24.
(71) Kulikova, T. V.; Bykov, V. A.; Shunyaev, K. Y.; Shubin, A. B. Thermal Properties of CuGa2 Phase in Inert Atmosphere. *Defect Diffus. Forum* **2012**, *326*−*328*, 227−232.
(72) Gundrum, B. C.; Cahill, D. G.; Averback, R. S. Thermal Conductance of Metal-Metal Interfaces. *Phys. Rev. B - Condens. Matter Mater. Phys.* **2005**, *72*, No. 245426.
(73) Cahill, D. G.; Ford, W. K.; Goodson, K. E.; Mahan, G. D.; Majumdar, A.; Maris, H. J.; Merlin, R.; Phillpot, S. R. Nanoscale Thermal Transport. *J. Appl. Phys.* **2003**, *93*, 793−818.
(74) Stauffer, D.; Aharony, A. *Introduction to Percolation Theory*, 2nd ed.; Taylor and Francis Inc., 1992.

DOI: 10.1021/acsami.7b15814
ACS Appl. Mater. Interfaces 2018, 10, 2083−2092

APPENDIX E

THERMAL CONDUCTIVITY ENHANCEMENTS OF SOFT POLYMER COMPOSITES THROUGH MAGNETICALLY-INDUCED PERCOLATION AND PARTICLE-PARTICLE CONTACT ENGINEERING

ADVANCED MATERIALS INTERFACES
www.advmatinterfaces.de

Thermal Conductivity Enhancement of Soft Polymer Composites through Magnetically Induced Percolation and Particle–Particle Contact Engineering

Matthew Ralphs, Wilson Kong, Robert Y. Wang, and Konrad Rykaczewski**

Despite major advancements in the performance of thermal interface materials (TIMs), contact resistance between components persists as a major thermal bottleneck in electronics packaging. In this work, the thermal performance of composite TIMs is enhanced through a synergistic coupling of magnetic alignment and engineered particle coatings that reduce the thermal resistance between particles. By itself, magnetically induced percolation of nickel particles within a cross-linked silicone matrix doubles the thermal conductivity of the composite. This process significantly increases contact between particles, making the interfacial particle–particle resistance a major contributor to the composites thermal performance. The resistance at these interfaces can be reduced by introducing soft metal (silver) or liquid metal coatings onto the nickel particles. Compressing powder beds of these hybrid particles reveals that, dependent on coating thickness, the contact engineering approach provides multifold increases in thermal conductivity at mild pressures. When dispersed in a polymer matrix and magnetically aligned, the coated particles provide a threefold increase in composite thermal conductivity, as compared to unaligned samples (up to nearly 6 W m^{-1} K^{-1} with volumetric fill fraction of 0.5). For equivalent coating thicknesses, silver coatings achieve better performance than liquid metal coatings.

1. Introduction

Thermal interface materials (TIMs) significantly enhance the heat removal from integrated circuits (ICs) by filling in the air gaps that result from geometrical imperfections at mating component surfaces. This greatly reduces the thermal contact resistance (R_c) between electronic components and enables better heat transfer.[1,2] TIMs are typically composites that consist of a base material in which thermally conductive particles are added. The base material is generally a cross-linked polymer matrix (i.e., a TIM "pad") or grease. The resulting composite thermal conductivity (k_c) of the TIM is typically up to an order of magnitude higher than the base material (e.g., up to 2 W m^{-1} K^{-1} vs 0.2 W m^{-1} K^{-1}). However, as transistor density has increased over the last decade, TIMs persist as a major thermal bottleneck in the thermal management of modern ICs.[3,4] Consequently, considerable research effort is dedicated to improving thermal performance of TIMs.

The thermal conductivity of TIM composites is traditionally improved by increasing the particle thermal conductivity (k_p) and the overall particle volumetric fraction (ϕ).[5–8] The most significant improvements to k_c are achieved by increasing ϕ to well above the percolation threshold (ϕ_p, typically around $\phi_p = 0.3$ for spheroidal particles).[9–11] Unfortunately, increasing the particle volume fraction to $\phi \geq 0.5$ in TIM pads, where significant k_c enhancements are made, also stiffens the composite.[12] This produces undesirable effects for microelectronics packaging applications, including increasing R_c at the surface of the TIM.[2] Recent advances have shown that using liquid metal inclusions in a polymer matrix can prevent composite stiffening, however, very high ϕ along with additional processing that elongates the inclusions is required to achieve notable thermal conductivity.[12–15]

Percolation can be enforced at $\phi \ll \phi_p$ by imposing a magnetic field on an uncured polymer composite with magnetically permeable fill particles. This simple and cost-effective process creates composites with highly anisotropic electrical and thermal conductivities that are significantly enhanced along the direction in which the particles are aligned.[15–20] For example, magnetically aligning spherical nickel particles in a polymer matrix provides a twofold improvement for k_c in the direction of particle alignment.[22,23] Furthermore, aligning particles with higher aspect ratios provides an even higher enhancement to k_c—up to three- and fourfold for particles with aspect ratios between 7 and 20.[24–27]

The direct contact between particles in these percolating networks decreases the interfacial thermal boundary resistance

M. Ralphs, W. Kong, Dr. R. Y. Wang, Dr. K. Rykaczewski
School for Engineering of Matter
Transport and Energy
Arizona State University
Tempe, AZ 85287, USA
E-mail: rywang@asu.edu; konradr@asu.edu

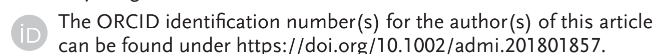
The ORCID identification number(s) for the author(s) of this article can be found under https://doi.org/10.1002/admi.201801857.

DOI: 10.1002/admi.201801857

© 2019 WILEY-VCH Verlag GmbH & Co. KGaA, Weinheim

(R_b). This boundary resistance—also referred to as Kapitza resistance[28]—is widely responsible for the diminishing returns seen in k_c when increasing k_p (e.g., a k_p increase from 20 to 400 W m^{-1} K^{-1} with $\phi = 0.5$ improves k_c by only 25%).[12,28,29] Note that, while R_c and R_b are both resistances due to interfaces, these two parameters differ from one another. In this paper, we use R_c to describe the interface resistance between macroscopic objects (e.g., electronic components in an IC) which is primarily due to imperfect physical contact. In contrast, we use R_b to describe the interface resistance between microscopic objects within the TIM composite. Both particle–matrix (R_{pm}) and particle–particle interfaces (R_{pp}) contribute to R_b, but the limiting thermal boundary resistance shifts from R_{pm} to R_{pp} when significant percolating networks are established and particle–particle contact is significantly increased.[30] Furthermore, R_{pp} can be reduced when using silver fill particles through welding or mechanical sintering.[31–36] These processes are enabled by the soft, nearly oxide-free silver surfaces and can lead to a 40-fold improvement in k_c.[37–40] Liquid metal can also lower R_{pp} by "soldering" particles together and improving the contact at the particle–particle interfaces.[12,21,29]

In this work, we aim to significantly enhance the thermal performance of composite TIM pads with $\phi \leq 0.5$ through the synergistic coupling of magnetically induced percolation and reduction of R_{pp} with particle–particle contact engineering. To enable the combination of these two approaches, we use nickel particles with two types of coatings: silver and liquid metal. To provide insight into the performance of these coatings, we first study the thermal resistance of bare nickel and coated nickel particle beds during compression. Next, we fabricate polymer matrix composites with a wide range of process parameters and quantify thermal conductivity enhancements that can be achieved through magnetic alignment and particle coating. Through additional characterization, we then relate these enhancements to the percolated structure of the composite and to the individual particle–particle interfaces.

2. Results and Discussion

2.1. Microscale Structure of Soft Composites with Magnetically Aligned Nickel Particles

Alignment of nickel and nickel-core particles is achieved by placing magnets on the top and bottom of a TIM mold prior to curing the polymer matrix. This results in a magnetic field across the TIM pad, producing forces that align the filler particles into columns. The induced dipole moment in the particles creates an inter-particle attraction that causes them to aggregate together as shown in the schematic in **Figure 1**a and as described by Borbath et al.[41] The application of this field induces evident alignment of nickel particles (diameter = 21 µm) in a silicone matrix at $\phi \leq 0.3$, but particle alignment becomes difficult to detect at $\phi \geq 0.4$ (see Figure S1, Supporting Information). Similar evidence of alignment is present with silver-coated nickel particles, as shown in Figure 1b. The presence of silver and LM (see Figure 5a) coatings do not disrupt the magnetic alignment process.

By magnetically aligning the particles, percolation is enforced, particle–particle contact is significantly increased, and R_{pp} becomes the limiting thermal boundary resistance. Thus, for composites with magnetically induced percolation, decreasing R_{pp} can have a measurable effect on the composite's thermal performance, even at low ϕ where R_c will be smaller and mechanical properties of the composite are uncompromised. To carefully investigate the effect of silver and liquid metal coatings on particle–particle thermal boundary resistance, we first investigate thermal transport in particle beds with no polymer matrix (Sections 2.2 and 2.3).

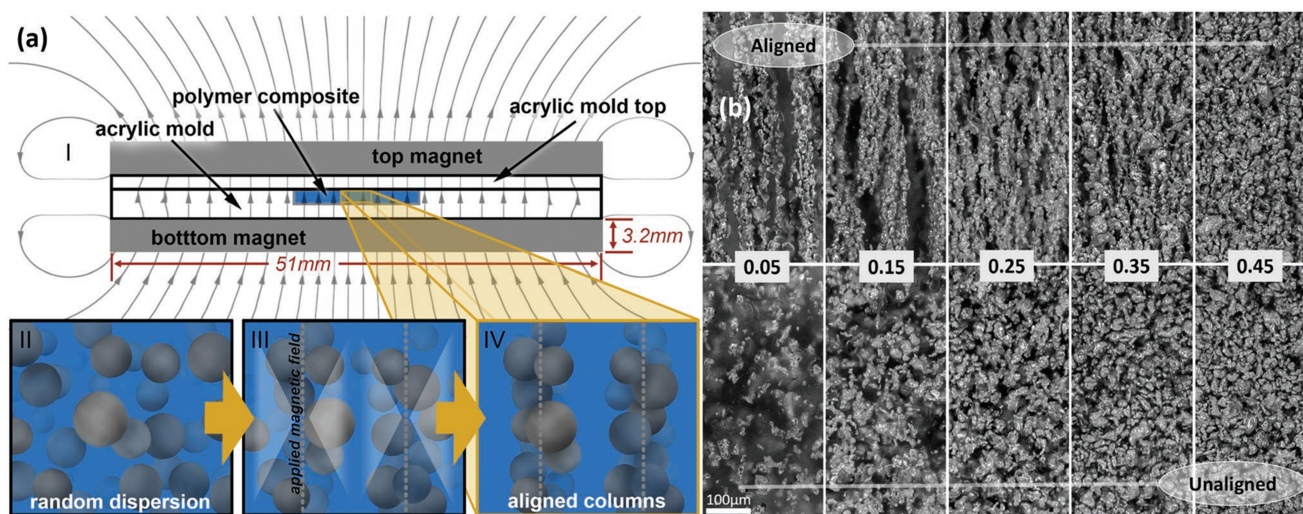

Figure 1. a) Illustration showing how, (I) when a magnetic field is applied, the particles go from (II) a random dispersion in the polymer matrix to (III) being aligned and (IV) forming columnar structures; and b) side view optical microscope images of the aligned (top) and unaligned (bottom) composites with (from left to right) 0.05, 0.15, 0.25, 0.35, and 0.45 volumetric fractions (ϕ) of nickel particles with 350 nm silver shells. Analogous optical microscope images of aligned and unaligned composites with bare Ni particles and liquid metal-coated Ni particles are available in Figures S1 and S2 in the Supporting Information.

 © 2019 WILEY-VCH Verlag GmbH & Co. KGaA, Weinheim

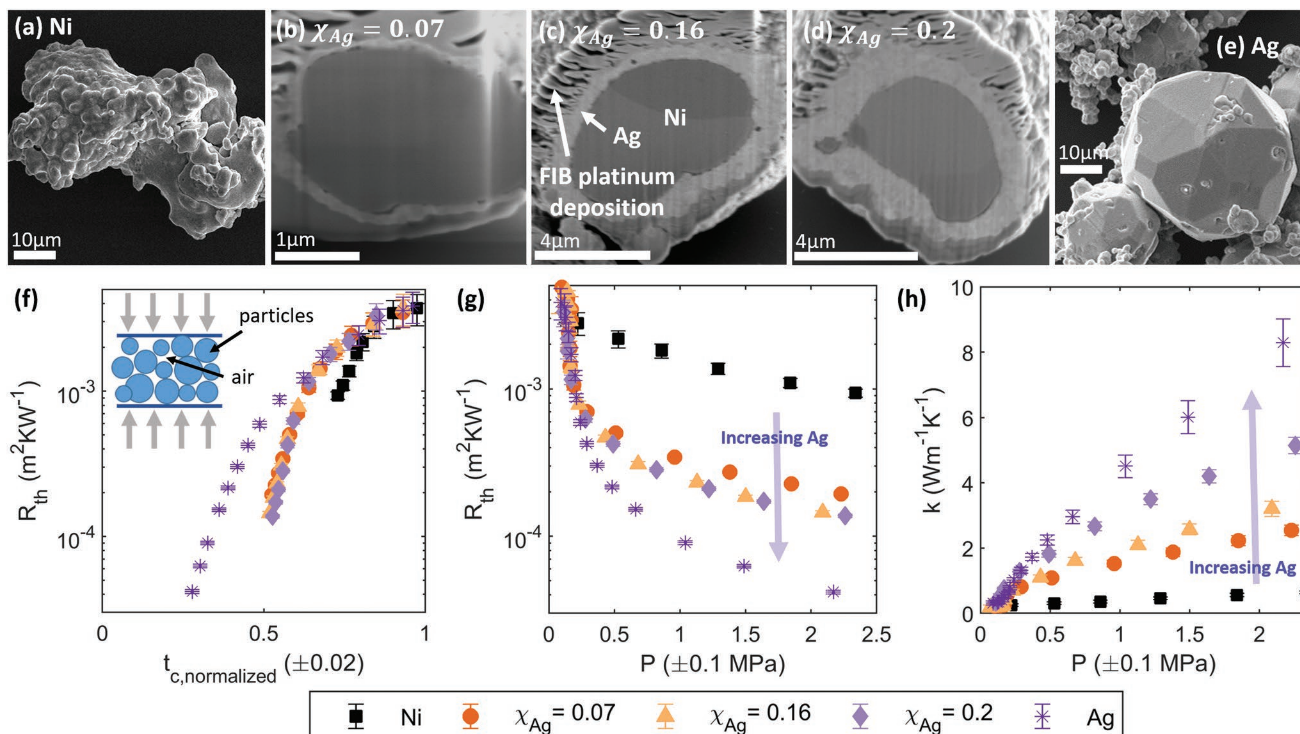

Figure 2. Scanning electron microscope (SEM) images of a) the nickel particles, b–d) Ag-coated particles that are cross-sectioned using an FIB with χ_{Ag} of 0.07, 0.16, and 0.2, respectively, and e) silver particles; f) the thermal resistance (R_{th}) plotted versus the normalized thickness (t_c) of the pressed powder beds with inset illustrating the process; g) thermal resistance plotted versus the pressure (P) applied to the powders; h) effective thermal conductivity plotted versus the pressure applied to the powders.

2.2. Contact Engineering with Silver Coatings on Nickel Particles

In this section, the soft and nearly oxide-free silver–silver interface characteristics are used to improve thermal transport in particle beds. Nickel particles as well as silver-coated nickel particles (8, 18, and 23 wt% Ag) were acquired from Potters Beads LLC. The base nickel particles on which the silver coatings are deposited are randomly shaped with an aspect ratio near 1 (**Figure 2**a). The 8, 18, and 23 wt% Ag particles correspond to calculated volume fractions of Ag to Ni, χ_{Ag}, of 0.07, 0.16, and 0.20, each having an average shell thickness of 350, 750, and 850 nm, respectively (Figure 2b–d). We also compare the thermal performance of pure silver (Figure 2e) and pure nickel (Figure 2a) as reference points using particles of similar size to that of the silver-coated nickel particles. Since the shells are relatively thin, the particle size distributions are similar for the uncoated and silver-coated nickel particles with a mean particle size of around 20 µm and a standard deviation of 10 µm (see the Supporting Information for further details).

The silver-coated nickel particles show a significant decrease in thermal resistance compared to the bare nickel particles when compressing loose particle powder beds (1 mm thick) in our stepped-bar apparatus (SBA).[42,43] The thermal resistance and sample thickness of the particle beds are measured as a function of the applied compressive force. The thickness of the compressed samples is normalized in Figure 2f by their estimated thickness at the estimated first point of contact with the SBA reference bars (this is where compression of the sample—and not just removal of the air above it—begins). Comparing the three thicknesses of silver coatings on nickel particles to the bare nickel shows a dramatic decrease in thermal resistance, even at pressures as low as 300 kPa (Figure 2g). Specifically, all three silver coatings provide less than a quarter of the thermal resistance of the bare nickel particles at a moderate pressure of 500 kPa. Nevertheless, as the pressure increases up to 1 MPa and beyond, the thicker silver coatings do show even lower resistances, with pure silver particles exhibiting the lowest resistance of all. It is worth noting that, near the maximum pressure tested, the bare nickel bed can only be compressed by about 25%. At this point, it has a thermal resistance lower than the coated particle beds with the same normalized thickness (see Figure 2f). However, the plot in Figure 2g reveals that the pressure required to compress the coated particles beds to this normalized thickness is an order of magnitude lower than the bare nickel particle beds (around 250 kPa) and is well below the 1 MPa maximum for most TIM applications.[44]

To confirm that the decrease in the overall thermal resistance stems from the deformation of the silver coatings, we image the various samples before and after compression. Imaging of the nickel particles after compressing them under more than 2 MPa shows no sign of surface deformations and they remain a loose powder. Conversely, the silver-coated nickel particles press into a cake under only 500 kPa that is easily handled and cross-sectioned without breaking apart (**Figure 3**a,b). Figure 3c clearly shows that the silver shell deforms under minor pressure, leading to better thermal contact and reduced resistance between particles, as illustrated in Figure 3d,e. This deformation also explains why

© 2019 WILEY-VCH Verlag GmbH & Co. KGaA, Weinheim

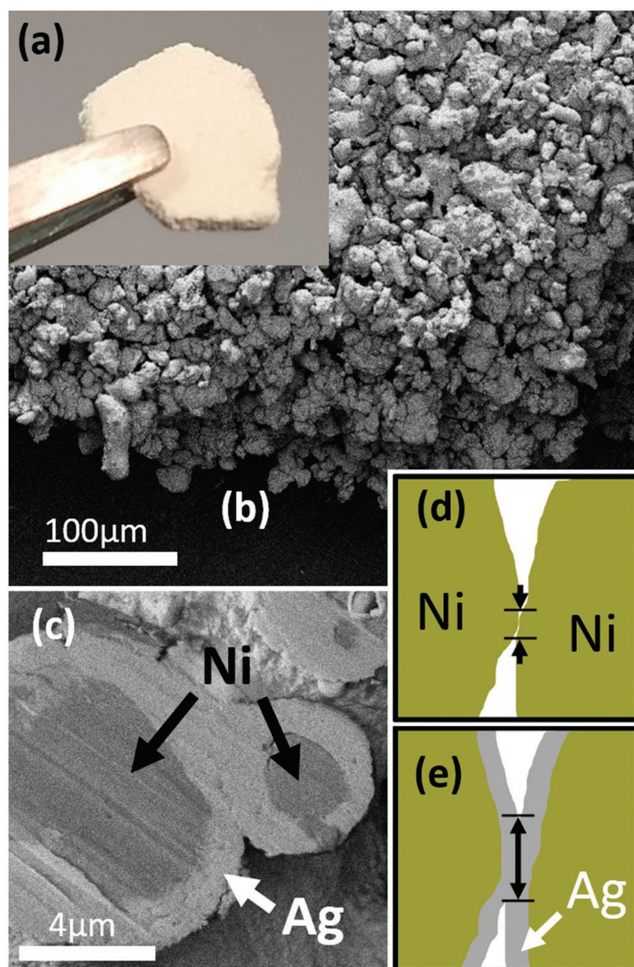

Figure 3. a) photo of the pressed silver-coated nickel powder; b) SEM image of the pressed silver-coated nickel powder; c) SEM of the cross-section of the silver-coated nickel powder showing how the silver coating allows the particles to fuse together; d) illustration showing the small interface area between two nickel particles compared to e) the larger interface of the deformed/fused silver–silver interface.

coated particle beds can be compressed significantly more than uncoated particle beds under the same applied pressure.

Compression of pure silver particles increases the thermal conductivity of the particle beds by eightfold—as compared to the bare nickel particles. However, pure silver is not affected by an applied magnetic field, preventing sufficient thermal performance in the polymer composite at reduced filler content through magnetically induced percolation. Furthermore, the pure silver particles used in this study are 30 times more expensive than the silver-coated nickel (see Figure S3, Supporting Information). This makes the silver-coated nickel particles a much more cost-effective way to reduce R_{pp} that can take advantage of magnetic alignment in the polymer composite.

2.3. Contact Engineering with Liquid Metal Coating of Nickel Particles

In this section, eutectic GaInSn is used as a coating on the nickel particles. The liquid nature of this material facilitates the "gluing" of the nickel particles together and the subsequent decrease of the interfacial thermal boundary resistance between them. This leads to meaningful increases in the thermal conductivity of particle beds. The LM-coated nickel mixtures are pressed between the copper reference bars of the SBA and the thermal properties measured with increasing pressure. **Figure 4**e,f shows energy-dispersive X-ray spectroscopy (EDS) maps and corresponding Scanning electron microscopy (SEM) images of the mixed LM-coated nickel particles for the volume fractions of LM, χ_{LM}, of 0.1, 0.2, 0.3, 0.4, and 0.5, before and after the compression experiments (additional EDS images, as well as optical images, are provided in Figures S4 and S5, Supporting Information). The images reveal that as the content of LM increases, so does the number of LM "bridges" that connect the nickel particles together. Ultimately, at $\chi_{LM} = 0.5$, the LM almost completely fills in the gaps between nickel particles as the sample is compressed. These LM-bridges thermally connect the nickel particles and significantly enhance the thermal conductivity of the pressed particle powders, as evidenced in Figure 4a,b. The increase in χ_{LM} from 0.1 to 0.5 steadily lowers the thermal resistance and at 500 kPa, the resistance of $\chi_{LM} = 0.5$ is an order of magnitude lower than bare Ni. Beyond 500 kPa, all samples decrease in R_{th} at roughly the same rate. The increase in thermal conductivity shows a similar trend with increasing χ_{LM}, but with a much larger jump between $\chi_{LM} = 0.4$ and 0.5. At 2 MPa, k doubles from 5 to 10 W m^{-1} K^{-1} at $\chi_{LM} = 0.4$ and 0.5, respectively.

With thick enough LM coatings, high powder bed thermal conductivities can be achieved. However, thin Ag coatings are still more effective. For example, at 2 MPa, χ_{Ag} of 0.07 and 0.2 reach 2.5 and 5 W m^{-1} K^{-1}, respectively, yet it requires χ_{LM} of 0.2 and 0.4 to reach similar k values. This effect most likely stems from the presence of gallium oxide, which naturally forms when LM is exposed to air.[45] This elastic, few nanometers thin oxide layer is prone to nanoscale and microscale wrinkling.[46,47] Thus, we postulate that the oxide layer on the LM provides inferior contact between particles relative to the silver coatings. To test this hypothesis, we coat the silver-coated nickel particles with a secondary LM film. The thermal resistance of this powder shows similar thermal properties to the LM-coated nickel – suggesting the superior silver-silver interface is lost under the LM and its oxide shell. In addition to being present at the interfaces, some gallium oxide flakes are also likely to be incorporated into the bulk of the LM during processing, providing another mechanism for the reduction in thermal conductivity.

Both the silver and LM coatings reduce R_{pp} and enhance the thermal conductivity of the nickel particle beds in an air environment. However, for application in TIMs pads, the particle coatings need to be effective in a polymer matrix. In the next section, we explore whether these engineered contacts also produce substantial increases in thermal performance within soft, cross-linked polymer matrices.

2.4. Thermal Conductivity Enhancement of Polymer Composites with Magnetically Aligned Silver- or LM-Coated Nickel Particles

Here, we evaluate the composite thermal conductivity enhancements that can be obtained through the synergistic

© 2019 WILEY-VCH Verlag GmbH & Co. KGaA, Weinheim

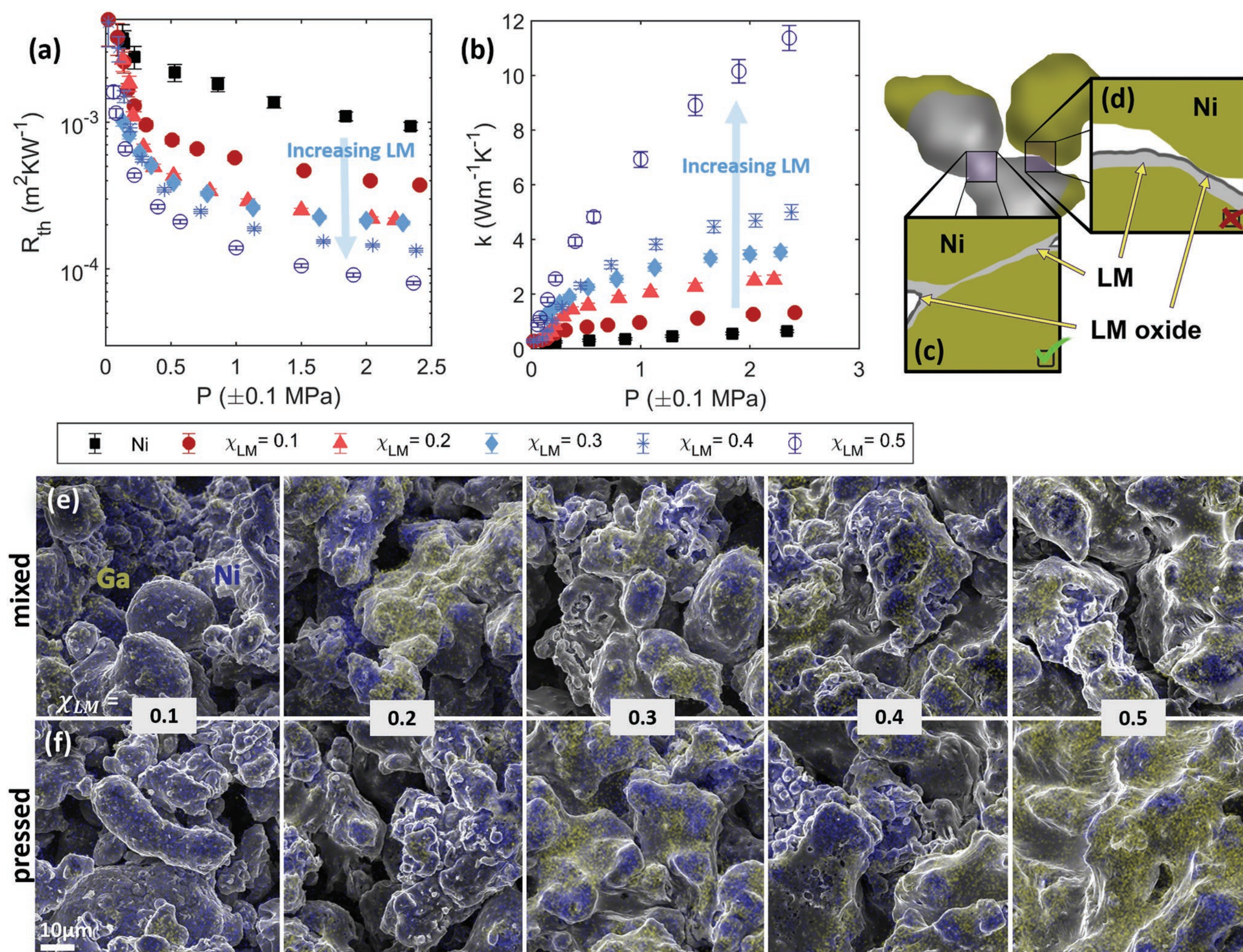

Figure 4. Properties of LM-coated nickel particles including a) R_{th} of the LM-coated nickel plotted against the pressure applied and b) k of the LM-coated nickel plotted against the applied pressure. An illustration of the LM coating on the nickel particles when c) the interface between Ni particles is completely encased in LM providing a good thermal connection and, conversely, d) when the LM oxide prevents a good thermal connection. And EDS images at (from left to right) χ_{LM} = 0.1, 0.2, 0.3, 0.4, and 0.5 e) prior to and f) after pressing them and measuring thermal properties.

effects of magnetically induced percolation and reduction of particle-particle boundary resistance by silver or LM particle coatings. Specifically, particles are incorporated in a soft silicone matrix, cast in the form of a TIM-pad, and cured in an applied magnetic field. Composite cross-sections of magnetically aligned LM-coated nickel particles at ϕ = 0.3 with χ_{LM} ranging from 0.1 to 0.5 are presented in **Figure 5**a. These images demonstrate that the LM coatings remain intact during magnetic alignment and the curing process. As expected, the magnetic alignment enforces percolation and induces contact between many particles, again making the effect of particle coatings (i.e., R_{pp} reduction) more pronounced.

The enhancement of the powder thermal conductivity achieved through silver and LM coating of nickel particles demonstrated in the preceding sections is also evident in the powder dispersed in the polymer matrix. Figure 5c presents the thermal conductivity of the elastomer composites at various ϕ. Both the silver and LM coatings provide a substantial increase in the thermal conductivity of the samples with magnetically aligned particles. Particle coatings do not impact the thermal conductivity of samples with unaligned particles for $\phi \le 0.4$. To avoid any artifacts stemming from variation between particle geometries that are likely to be more pronounced at higher filler packing ($\phi \ge 0.4$), we investigate the effect of the thickness of particle coatings in the polymer composite at $\phi = 0.3$ (i.e., the theoretical threshold for the onset of percolation). We also note that at $\phi \ge 0.4$ we occasionally observed evidence of minor LM leakage from pads under compression, which could be undesirable in TIM applications.

Comparing the thickness of the silver coatings in Figure 5b reveals no significant increase in k_c with increasing silver shell thickness. This is in contrast to the results from the powder bed measurements (compare to Figure 2h) where the thicker silver shells provided further enhancement to thermal performance. In these polymer composites, ϕ is only 0.3 whereas in the powder beds it is closer to 0.6—the maximum packing factor for random spheres.[48] Therefore, the number of particles in good contact with one another other would be larger in the particle beds. Another important consideration is the difference in applied pressure during thermal transport measurements

 © 2019 WILEY-VCH Verlag GmbH & Co. KGaA, Weinheim

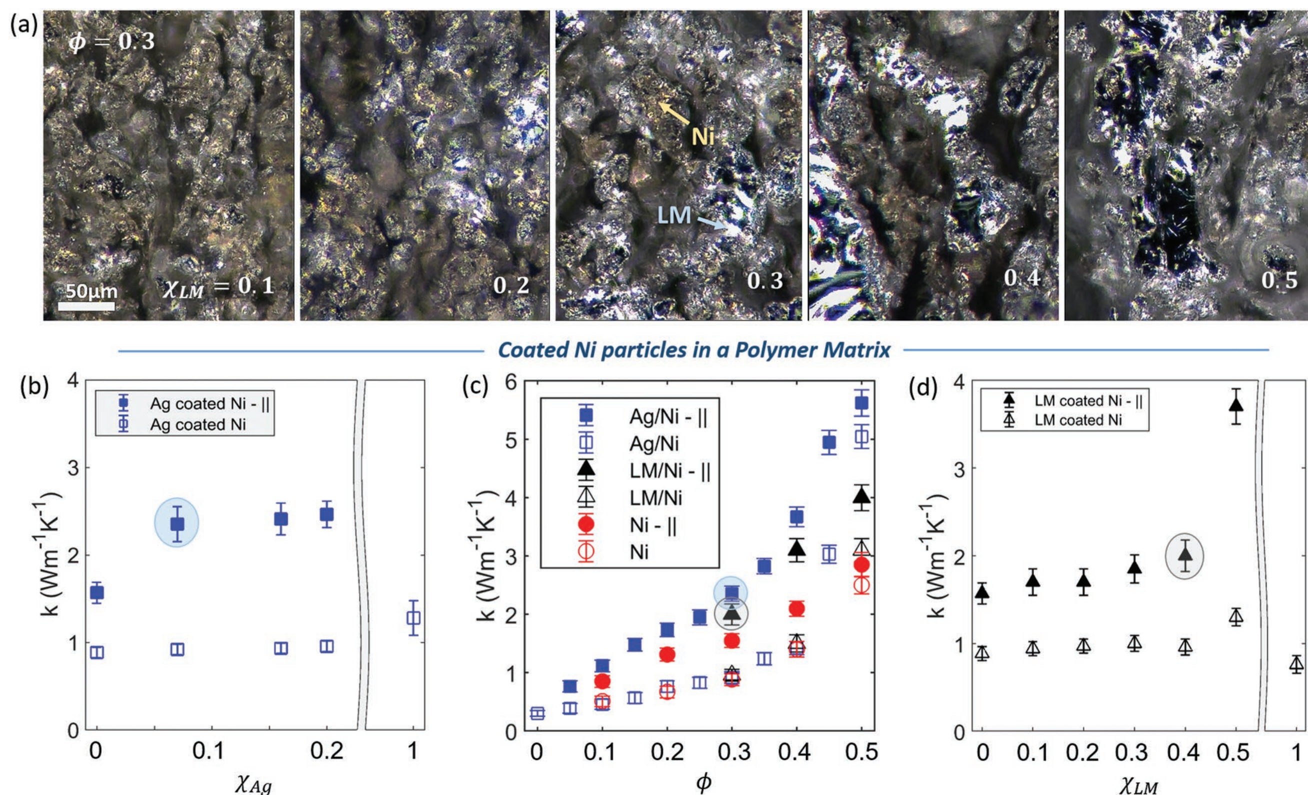

Figure 5. a) Cross-sections of aligned LM-coated nickel particles in the polymer composite at $\phi = 0.3$ with χ_{LM} of 0.1, 0.2, 0.3, 0.4, and 0.5. The nickel particles can be identified by their brown-gold coloring and the LM by its high reflectance and silver color. b) The enhancement due to magnetic alignment (||) as χ_{Ag} increases from 0 (pure nickel particles) to 1 (pure silver particles) at $\phi = 0.3$ and a compressive strain of 5%. c) The comparison of k versus ϕ of aligned and unaligned nickel particle composites as well as silver-coated nickel composites ($\chi_{Ag} = 0.07$) and LM-coated nickel composites ($\chi_{LM} = 0.4$) at a compressive strain of 5%. And d) k versus χ_{LM} with both aligned and unaligned fill at $\phi = 0.3$ and a compressive strain of 5%. The shaded circles highlight the same data points across the multiple plots.

for the polymer composites versus the powder beds. The polymer composites in Figure 5b were only tested up to a pressure of 150 kPa whereas the powder beds were tested up to 2 MPa. Consequently, the Ag-coatings in the powder beds likely experienced much more deformation and fusion than in the polymer composites. Thus, thicker shells provide less benefit in these polymer composites. Testing on the polymer composites was limited to 150 kPa in order to maintain a compressive strain of 5% across all the samples to minimize contact resistance yet prevent negative thermal effects from aligned column buckling.[27]

The effects of the various LM coatings are also evaluated at $\phi = 0.3$ (Figure 5d). Increasing the LM content increases k_c for aligned particles, but not as drastically as in the compressed LM-coated Ni powders (compare to Figure 4b). There are only minor increases in k_c from increasing the thickness of the LM coating (a 5% increase in k_c for every 10% increase in χ_{LM}) until $\chi_{LM} > 0.4$, where it jumps by 50% to near 4 W m^{-1} K^{-1} at $\chi_{LM} = 0.5$. We note that samples with $\chi_{LM} = 0.5$ had a visible decrease in mechanical stability when handling the composites and so we focused the majority of our studies on $\chi_{LM} = 0.4$ (Figure 5c).

We note that in order to obtain these meaningful enhancements in composite thermal conductivity using liquid metal coatings, it is important to combine the liquid metal– nickel particle mixture into the polymer in a particular manner. More specifically, aggressive mixing of the liquid metal–nickel mixture into the polymer results in independent nickel particles and liquid metal inclusions dispersed in the polymer matrix. It is more advantageous to preserve liquid metal–nickel aggregates (i.e., multiple nickel particles in a liquid metal droplet as opposed to single nickel particles in a liquid metal droplet). The LM must connect several nickel particles inside its oxide skin. Otherwise, the polymer matrix will wet the self-passivating Ga oxide[49] that covers the coated particles and no decrease in thermal resistance will be evident between nickel particles. The importance of these material processing characteristics is described in our prior work, in which we used LM-coated copper particles in a three-phase polymer composite and leveraged the unique, rapid alloying of copper and gallium to enhance percolation through the polymer matrix.[29] The use of magnetic alignment allows for achieving percolation at much lower filler volume ratios and significantly increases repeatability of the results. In addition, it is important to note that the aligned composites are electrically conducting under compression at high ϕ.

The largest enhancement from the magnetic alignment of the particles is at $\phi = 0.4$. Magnetic alignment of the bare nickel particle composites increases k_c by a factor of 1.6 (from 1.3 to 2.1 W m^{-1} K^{-1}), while the alignment of the LM- and Ag-coated particle composites increases k_c by a factor of 2.2 and 2.6 (from

© 2019 WILEY-VCH Verlag GmbH & Co. KGaA, Weinheim

1.4 to 3.1 and 3.7 W m^{-1} K^{-1}), respectively. This means that the LM and Ag coatings themselves increase k_c by 50% and 75%, respectively, over the aligned bare nickel particle composites at $\phi = 0.4$. These enhancements are of similar or greater magnitude than those previously achieved using other methods that increase conductance between filler particles in a polymer matrix such as bridging Ni particles with carbon nanotubes.[50,51]

3. Conclusions

Magnetic alignment of nickel particles in a polymer composite enforces percolation of the high k particles through the low k polymer matrix, increasing the thermal conductivity of the composite by around 150%. It also increases the particle-particle interactions, making the thermal boundary resistance at the particle–particle interfaces a dominant thermal resistance. Thus, modifying the particle interfaces to lower R_{pp} has a large impact when particles are magnetically aligned in the composite.

Leveraging the soft, nearly oxide-free silver surfaces as a coating on the nickel particles in a dry powder bed provides a fivefold decrease in thermal resistance with only 500 kPa of applied pressure. Similarly, the fluid nature of GaInSn is leveraged as a coating and bonding agent between nickel particles to cut the thermal resistance of the pressed particle beds in half with $\chi_{LM} = 0.1$ and a full order of magnitude with $\chi_{LM} = 0.5$. Both coatings reduce R_{pp} and increase the thermal performance of the nickel particles, but the Ag coatings provide more benefit than LM coatings at an equivalent coating thickness.

Combining these engineered interfaces with magnetic alignment in a polymer composite results in significant enhancements in k_c. Nickel particles with silver shells of only 350 nm show a 175% increase in k_c over the bare Ni in the aligned polymer composites, achieving 3.7 W m^{-1} K^{-1} at $\phi = 0.4$. Similarly, $\chi_{LM} = 0.4$ particles show a 150% increase over the aligned Ni composites, achieving 3.1 W m^{-1} K^{-1}. This work provides significant insight into surface engineering and materials processing methodology that lead to improvements in soft, thermally conductive composites. Future work will investigate how to minimize the negative thermal effects of LM oxide–LM oxide interfaces to enable greater enhancements with less LM to bridge the thermal gap between high k fill particles.

4. Experimental Section

Materials: The polymer matrix used in this work for all the composites is Smooth-On EcoFlex 00-20, a soft, platinum cured silicone elastomer with a thermal conductivity of 0.3 ± 0.03 W m^{-1} K^{-1} (95% uncertainty). The nickel particles (Ni325, 325 mesh nickel powder), as well as the silver-coated nickel particles (SN40P08, SN40P18, SN325P25-ALT1), were all purchased from Potters Beads LLC. Size distributions of the nickel and silver-coated nickel particles, measured with ImageJ from SEM images, are provided in Figure S6 in the Supporting Information. The silver particles (325 mesh, supplier ID 327107-10G) were purchased from Sigma Aldrich. The GaInSn eutectic mixture, Galinstan, was purchased from Rotometals.

Material densities used in this work were 6.44 g mL^{-1} for Galinstan, 10.50 g mL^{-1} for silver, and 8.91 g mL^{-1} for nickel. The densities of the silver-coated nickel were calculated by multiplying the densities of each constituent by the weight percent of that constituent, then adding the two partial densities together. For example, the density of the 8 wt% Ag particles is calculated as

$$\text{Ag}: 10.5\ \text{g mL}^{-1} * 0.08 = 0.840\ \text{g mL}^{-1} \qquad 0.84\ \text{g mL}^{-1}$$

$$\text{Ni}: 8.91\ \text{g mL}^{-1} * 0.92 = 8.20\ \text{g m}^{-1} \qquad \frac{+8.20\ \text{g mL}^{-1}}{9.04\ \text{g mL}^{-1}}$$

Densities for the 18 and 23 wt% Ag particles are calculated as 9.20 and 9.28 g mL^{-1}, respectively.

Composite Fabrication: The particles were weighed out and mixed into the polymer matrix by hand with a mortar and pestle. For the composites with LM on the solid particles, the LM and solid fill were mixed in the mortar and pestle prior to adding the polymer and stirring the mixture lightly with a stir rod until somewhat homogenous, but without breaking up the LM-solid particle agglomerations. Since the oxidation of the LM has been shown to aid in wetting other metals, we mix the nickel powder with various amounts of LM in an air environment.[52,53] The uncured composite was vacuum degassed to remove air bubbles prior to pouring into rectangular acrylic molds with dimensions of 1.5 × 12.7 × 12.7 mm. An acrylic top was placed on the mold and magnets (BY0Y02, 2″ × 2″ × 1/8″, NdFeB, Grade N42) purchased from K&J Magnetics, Inc. were placed on top and bottom of the acrylic mold for the magnetically aligned samples, which positioned the magnets 2.25 mm above and below the center of the sample. Borbath et al.[41] observed that a maximum column thickness was formed with a magnetic field strength of 110 kA m^{-1}, similar to the magnetic field strength applied in our fabrication procedure. For the unaligned sample, a weight was placed on top of the mold during cure. The composites were cured at room temperature for 3 h.

Microscopy: Optical microscopy was conducted with Zeiss Axio Zoom.V16 with an objective lens of 2.3 × /0.57 FWD and 10.6 mm focal length Zeiss PlanNeoFluar Z. SEM of the particles was conducted using an Amray 1910 with field emission gun and was conducted at 20 kV and a working distance of between 8 and 12 mm. The cross-sectioning and imaging of the silver-coated nickel particles were done using a focused ion beam (FIB) instrument (FEI Nova Nanolab 200 FIB/SEM) using typical procedure.[54]

Thermal Measurements: Thermal resistances (R_{th}) were measured in line with the aligned particles using an SBA.[42,43] A linear encoder installed on the SBA measured the distance between the copper reference bars, thus providing a good estimate of the compressed sample thickness (t_c). A load cell integrated with the SBA provided concurrent load measurements. Thermal conductivity was calculated as

$$k = \frac{t_c}{R_{th}} \tag{1}$$

where t_c is in meters and R_{th} is in m^2 KW^{-1}. The average sample temperature during thermal measurements was 55 °C. A thin layer of Galinstan was applied on top and bottom of the samples to minimize contact resistance at the sample–reference bar interface. The copper reference bars are not affected by gallium within the short timeframe of the measurements.[18]

Supporting Information

Supporting Information is available from the Wiley Online Library or from the author.

Acknowledgements

M.I.R. acknowledges support through Arizona State University's (ASU) Fulton Schools of Engineering Dean's Fellowship. K.R. and R.Y.W. acknowledge funds from Semiconductor Research Corporation contract

© 2019 WILEY-VCH Verlag GmbH & Co. KGaA, Weinheim

#2017-PK-2787 and from Fulton Schools of Engineering at ASU. The authors also acknowledge the use of facilities within the LeRoy Eyring Center for Solid State Science at Arizona State University.

Conflict of Interest

The authors declare no conflict of interest.

Keywords

boundary resistance, liquid metal, polymer composites, silver, thermal interface materials

Received: November 19, 2018
Revised: January 9, 2019
Published online:

[1] R. S. Prasher, P. E. Phelan, *J. Appl. Phys.* **2006**, *100*, 063538.
[2] R. S. Prasher, C.-P. Chiu, in *Materials for Advance Packaging*, (Eds: D. Lu, C. P. Wong), Springer, Switzerland **2017**, pp. 511–535.
[3] S. P. Gurrum, S. K. Suman, Y. K. Joshi, A. G. Fedorov, *IEEE Trans. Device Mater. Reliab.* **2004**, *4*, 709.
[4] A. L. Moore, L. Shi, *Mater. Today* **2014**, *17*, 163.
[5] Z. Han, A. Fina, *Prog. Polym. Sci.* **2011**, *36*, 914.
[6] A. Bar-Cohen, K. Matin, S. Narumanchi, *J. Electron. Packag.* **2015**, *137*, 040803.
[7] F. Sarvar, D. Whalley, P. Conway, *2006 1st Electron. Syst. Technol. Conf.* **2006**, *2*, 1292.
[8] N. Burger, A. Laachachi, M. Ferriol, M. Lutz, V. Toniazzo, D. Ruch, *Prog. Polym. Sci.* **2016**, *61*, 1.
[9] R. Consiglio, D. R. Baker, G. Paul, H. E. Stanley, *Phys. A (Amterdam, Neth.)* **2003**, *319*, 49.
[10] J. F. Douglas, F. Thorpe, **1995**, *52*, 819.
[11] S. Galam, A. Mauger, *Phys. Rev. E* **1996**, *53*, 2177.
[12] R. Tutika, S. H. Zhou, R. E. Napolitano, M. D. Bartlett, *Adv. Funct. Mater. 28*, **2018**, 1804336.
[13] S. H. Jeong, S. Chen, J. Huo, E. K. Gamstedt, J. Liu, S.-L. Zhang, Z.-B. Zhang, K. Hjort, Z. Wu, *Sci. Rep.* **2016**, *5*, 18257.
[14] M. D. Bartlett, C. Majidi, *Proc. Natl. Acad. Sci. USA* **2017**, 8.
[15] L. Zhao, H. Liu, X. Chen, S. Chu, H. Liu, Z. Lin, Q. Li, G. Chu, H. Zhang, *J. Mater. Chem. C* **2018**, *6*, 10611.
[16] E. Breval, M. Klimkiewicz, Y. T. Shi, D. Arakaki, J. P. Dougherty, *J. Mater. Sci.* **2003**, *38*, 1347.
[17] S. Ramkumar, K. Srihari, *J. Electron. Packag.* **2007**, *129*, 149.
[18] T. Lu, J. Wissman, C. Majidi, *ACS Appl. Mater. Interfaces* **2015**, *7*, 26923.
[19] S. Jin, R. C. Sherwood, J. J. Mottine, T. H. Tiefel, R. L. Opila, J. A. Fulton, *J. Appl. Phys.* **1988**, *64*, 6008.
[20] S. Jin, T. H. Tiefel, R. Wolfe, *IEEE Trans. Magn.* **1992**, *28*, 2211.
[21] T. Lu, E. Markvicka, Y. Jin, C. Majidi, *ACS Appl. Mater. Interfaces* **2017**, *9*, 22055.
[22] J. E. Martin, G. Gulley, *J. Appl. Phys.* **2009**, *106*, 084301.
[23] J. Su, X. Liu, M. Charmchi, H. Sun, *Int. J. Heat Mass Transfer* **2016**, *97*, 645.
[24] K. J. Solis, J. E. Martin, *J. Appl. Phys.* **2012**, *111*, 073507.
[25] C. Yuan, B. Duan, L. Li, B. Xie, M. Huang, X. Luo, *ACS Appl. Mater. Interfaces* **2015**, *7*, 13000.
[26] J. E. Martin, A. Snezhko, *Rep. Progr. Phys.* **2013**, *76*, 126601.
[27] M. Ralphs, C. Scheitlin, R. Y. Wang, K. Rykaczewski, *J. Heat Transfer* **2018**.
[28] D. G. Cahill, W. K. Ford, K. E. Goodson, G. D. Mahan, A. Majumdar, H. J. Maris, R. Merlin, S. R. Phillpot, *J. Appl. Phys.* **2003**, *93*, 793.
[29] M. I. Ralphs, N. Kemme, P. B. Vartak, E. Joseph, S. Tipnis, S. Turnage, K. N. Solanki, R. Y. Wang, K. Rykaczewski, *ACS Appl. Mater. Interfaces* **2018**, *10*, 2083.
[30] Y. P. Mamunya, V. V. Davydenko, P. Pissis, E. V. Lebedev, *Eur. Polym. J.* **2002**, *38*, 1887.
[31] N. Balachander, I. Seshadri, R. J. Mehta, L. S. Schadler, T. Borca-Tasciuc, P. Keblinski, G. Ramanath, *Appl. Phys. Lett.*093117, **2013**, *102*.
[32] K. Pashayi, H. R. Fard, F. Lai, S. Iruvanti, J. Plawsky, T. Borca-Tasciuc, *J. Appl. Phys.* **2012**, *111*, 104310.
[33] H. Yu, L. Li, Y. Zhang, *Scr. Mater.* **2012**, *66*, 931.
[34] I. Seshadri, G. L. Esquenazi, T. Borca-Tasciuc, P. Keblinski, G. Ramanath, *Adv. Mater. Interfaces* **2015**, *2*, 1500186.
[35] I. Seshadri, G. L. Esquenazi, T. Cardinal, T. Borca-Tasciuc, G. Ramanath, *Nanotechnology* **2016**, *27*, 175601.
[36] B. Hwang, H. A. S. Shin, T. Kim, Y. C. Joo, S. M. Han, *Small* **2014**, *10*, 3397.
[37] F. H. Buttner, E. R. Funk, H. Udin, *J. Phys. Chem.* **1952**, *56*, 657.
[38] W. M. Moore, P. J. Codella, *J. Phys. Chem.* **1988**, *92*, 4421.
[39] A. De Rooij, *EsA J.* **1989**, *13*, 363.
[40] J. W. D. Callister, *Material Science and Engineering An Introduction*, John Wiley & Sons, Inc., New York, US **2007**.
[41] T. Borbath, S. Günther, D. Y. Borin, T. Gundermann, S. Odenbach, *Smart Mater. Struct.* **2012**, *21*, 105018.
[42] D. R. Thompson, S. R. Rao, B. a. Cola, *J. Electron. Packag.* **2013**, *135*, 041002.
[43] M. I. Ralphs, B. L. Smith, N. A. Roberts, *Meas. Sci. Technol.* **2016**, *27*, 115014.
[44] R. Prasher, in *Proc. IEEE*, IEEE **2006**, Vol. *94*, pp. 1571–86.
[45] M. D. Dickey, *ACS Appl. Mater. Interfaces* **2014**, *6*, 18369.
[46] K. Doudrick, S. Liu, E. M. Mutunga, K. L. Klein, V. Damle, K. K. Varanasi, K. Rykaczewski, *Langmuir* **2014**, *30*, 6867.
[47] S. Liu, X. Sun, N. Kemme, V. G. Damle, C. Schott, M. Herrmann, K. Rykaczewski, *Microfluid. Nanofluid.* **2016**, *20*, 1.
[48] A. V. Anikeenko, N. N. Medvedev, T. Aste, *Phys. Rev. E* **2008**, *77*, 1.
[49] Y. Zheng, Q. Zhang, J. Liu, *AIP Adv.* **2013**, *3*, 1.
[50] X. Hu, L. Jiang, K. E. Goodson, *Ninth Intersoc. Conf. Therm. Thermomechanical Phenom. Electron. Syst. (IEEE Cat. No.04CH37543)*, IEEE **2004**, 63.
[51] W. Park, K. Choi, K. Lafdi, C. Yu, *J. Heat Transfer* **2012**, *134*, 041302.
[52] U. Daalkhaijav, O. D. Yirmibesoglu, S. Walker, Y. Mengüç, *Adv. Mater. Technol.* **2018**, *3*, 1700351.
[53] G. Li, Y. Ji, M. Wu, H. Ma, in *ASME 2016 Heat Transf. Summer Conf. Collocated with ASME 2016 Fluids Eng. Div. Summer Meet. ASME 2016 14th Int. Conf. Nanochannels, Microchannels, Minichannels*, American Society Of Mechanical Engineers **2016**, pp. V001T04A004–V001T04A004.
[54] N. Antoniou, K. Rykaczewski, M. D. Uchic, *MRS Bull.* 347, **2014**, *39*.

© 2019 WILEY-VCH Verlag GmbH & Co. KGaA, Weinheim

BIOGRAPHICAL SKETCH

Matthew Ralphs is the son of Michael H. Ralphs and Diana [Alldregde] Ralphs. He grew up in Paradise, Utah. He graduated as Valedictorian from Mountain Crest High School in Hyrum, Utah in 2006 and went on to undergraduate studies at Utah State University with the aid of the Presidential Scholarship. He graduated Utah State University with a Bachelor of Science degree in Mechanical Engineering with departmental honors and Minors in Spanish and Mathematics in May 2012. The week after graduating from USU, he married Amanda Karen Johnson and they moved to Newton, Kansas, where his new job awaited as a Test and Reliability Engineer at AGCO Corp. After 2+ years at AGCO he returned to USU in pursuit of a Master's Degree and accepted a position as a Graduate Research Assistance under Dr. Nicholas Roberts. He graduated from USU with a Master of Science degree in Mechanical Engineering in May 2016 with a Thesis titled, "Investigating the Effect of Carbon Nanotube Functionalization in a PolyDimethylSiloxane Composite through use of a Stepped-Bar Apparatus." Having been offered the prestigious Dean's Fellowship to continue his graduate career at Arizona State University, he moved his, now, family-of-four to Gilbert Arizona to start a PhD in Fall 2016. He was co-advised by Dr. Konrad Rykaczewski and Dr. Robert Wang and will graduate with his PhD in Mechanical Engineering in May 2019. He has accepted a position as a Mechanical Engineer at the Space Dynamics Laboratory in Logan, Utah.